Mechanical reliability of aluminum nitride thin films

Jere Kinnunen

School of Electrical Engineering

Thesis submitted for examination for the degree of Master of Science in Technology.

Espoo 22.5.2017

Thesis supervisor:

Prof. Mervi Paulasto-Kröckel

Thesis advisor:

M.Sc. (Tech.) Elmeri Österlund

Aalto University
School of Electrical Engineering

AALTO UNIVERSITY
SCHOOL OF ELECTRICAL ENGINEERING

ABSTRACT OF THE
MASTER'S THESIS

Author: Jere Kinnunen

Title: Mechanical reliability of aluminum nitride thin films

Date: 22.5.2017 Language: English Number of pages: 8+102

Department of Electrical Engineering and Automation

Professorship: Electronics Integration and Reliability

Supervisor: Prof. Mervi Paulasto-Kröckel

Advisor: M.Sc. (Tech.) Elmeri Österlund

The purpose of this Master's Thesis is to study the mechanical reliability of aluminum nitride thin films. This is done by measuring the relevant mechanical properties of the thin films through use of the bulge test.
The Young's moduli, residual stresses, ultimate tensile strengths and fracture toughness of AlN thin films are measured. A fatigue cycling experiment is conducted in order to study the effects of cyclic loading on these films.
The measurements are conducted on films of two thicknesses produced by sputtering (54 and 220 nm) and on a 126 nm film deposited with MOVPE.
The implications of the results are analyzed in detail with an error analysis, and the way these material properties can be used in design for reliability is presented.

Keywords: aluminum nitride, thin film, bulge test, mechanical reliability, Young's modulus, residual stress, ultimate tensile strength, fracture toughness, fatigue

AALTO-YLIOPISTO
SÄHKÖTEKNIIKAN KORKEAKOULU

DIPLOMITYÖN
TIIVISTELMÄ

Tekijä: Jere Kinnunen

Työn nimi: Alumiininitridi-ohutkalvojen mekaaninen luotettavuus

Päivämäärä: 22.5.2017 Kieli: Englanti Sivumäärä: 8+102

Elektroniikan laitos

Professuuri: Elektroniikan integroinnin ja luotettavuuden laitos

Työn valvoja: Prof. Mervi Paulasto-Kröckel

Työn ohjaaja: DI Elmeri Österlund

Tämän diplomityön tarkoitus on tutkia alumiininitridi-ohutkalvojen mekaanista luotettavuutta. Tutkimus on toteutettu mittaamalla bulge test-testimetodin avulla näiden ohutkalvojen relevantit mekaaniset ominaisuudet.
Alumiininitridi-ohutkalvojen kimmokertoimet, jäännösjännitteet, murtolujuudet ja murtositkeydet on mitattu. Kalvojen väsymisominaisuuksia tutkittiin syklitystestillä.
Mittaukset on tehty kahdella eri pinnoitustekniikalla (sputterointi ja MOVPE) tuotetuille kalvoille. Testatut sputteroidut kalvot ovat 54 nm ja 220 nm paksuja, ja MOVPE-kalvot 126 nm paksuja.
Tuloksien luotettavuus, sekä tuloksista tehtävissä olevat johtopäätökset ovat esitelty yksityiskohtaisesti. Tapoja, joilla tuloksia voi käyttää luotettavien alumiininitridiohutkalvoja käyttävien sovellusten suunnittelemisessa, on annettu.

Avainsanat: alumiininitridi, ohutkalvo, bulge-testi, mekaaninen luotettavuus, kimmokerroin, jäännösjännite, murtolujuus, murtositkeys, väsyminen

Preface

I would like to thank Professor Mervi Paulasto-Kröckel for the opportunity of doing this research work as a part of the Electronics Intergration and Reliability group. I'd like to thank M.Sc. Elmeri Österlund as well for his continuous support and supervision throughout the thesis work. Thanks go as well to all the other members of the EIR group for answering all the questions I came up with.

The thesis work would not have been possible without Doctor Altti Torkkeli as well, so thanks go to him, and Mr. Keiichi Umeda and Mr. Yasuhiro Aida from Murata Japan for the provided research material.

The experience and insight on the bulge experiment of M.Sc. Ville Rontu were as well important for the success of the experimental part of this thesis, for which I am thankful.

The testing equipment at the Electronics Research Lab of Helsinki University were as well vital for the experiments, and thus I am grateful to Professor Edward Häggström and Ph.D. Ivan Kassamakov for the possibility of using the equipment. The expertise with the SWLI device was vital for fast and accurate measurements, and thus the contribution of M.Sc. Anton Nolvi made obtaining and analyzing these results viable.

Thanks go as well to the guys at HS-Foils for their assistance and expertise in operating the bulge testing device.

Last but not least, all work and no play makes a thesis a dull game, and thus I'm thankful to my family, Skipoli, for keeping me busy, when I wasn't busy with the thesis work.

Otaniemi, 22.5.2017

Jere I. Kinnunen

Contents

Abstract ii

Abstract (in Finnish) iii

Preface iv

Contents v

Symbols and abbreviations viii

1 Introduction 1

2 Background 3
2.1 AlN MEMS . . . 3
2.2 Physics of fracture . . . 4
2.3 Young's modulus . . . 6
2.4 Fracture toughness . . . 7
2.5 R-curve behaviour . . . 10
2.6 Ultimate tensile strength . . . 11
2.7 Anelasticity . . . 12
2.8 Crack tip opening displacement . . . 12
2.9 J-integral . . . 13
2.10 Residual stress . . . 13
2.11 Fatigue . . . 14
2.12 Thin films versus bulk material . . . 15
2.12.1 Geometry effects . . . 15
2.12.2 Material properties . . . 16

3 Research material 19
3.1 Materials and their relevant properties . . . 19
3.1.1 Aluminum nitride . . . 19
3.1.2 Silicon . . . 22
3.2 Defect types and their formation . . . 23

4 Fabrication methods 26
4.1 Deposition methods . . . 26
4.1.1 Atomic Layer Deposition . . . 26
4.1.2 Metalorganic vapour phase epitaxy . . . 27
4.1.3 Sputter deposition . . . 28
4.2 Sample fabrication methods . . . 29
4.2.1 Deep reactive ion etching . . . 29
4.2.2 Focused ion beam milling . . . 30
4.2.3 Lithography . . . 30

5 Testing methods **32**
5.1 Four point bending . . . 32
5.2 Scratch testing . . . 33
5.3 Nano or microindentation . . . 34
5.4 Micropillar indentation . . . 35
5.5 Microcantilever testing . . . 37
5.6 Microtensile film tests . . . 38
5.7 Bulge test . . . 40

6 Characterization methods **42**
6.1 X-ray diffraction . . . 42
6.2 Ellipsometry . . . 43
6.3 Scanning electron microscopy . . . 43

7 Design of experiments **45**
7.1 Experimental question . . . 45
7.2 Experimental procedure . . . 45
7.2.1 Bulge test for UTS, Young's modulus and residual stress . . . 46
7.2.2 Fatigue testing . . . 49
7.2.3 Bulge test for fracture toughness . . . 50
7.2.4 Bulge tester at Micronova . . . 52
7.2.5 Bulge tester with scanning white light interferometry at Helsinki University . . . 53
7.3 Characterization . . . 55
7.3.1 X-ray diffraction . . . 55
7.3.2 Ellipsometry . . . 55
7.4 Statistical analysis . . . 56

8 Samples and sample preparation **59**
8.1 Sample material . . . 60
8.1.1 Sputter deposition . . . 60
8.1.2 MOVPE . . . 61
8.2 ALD aluminum oxide hard mask . . . 61
8.3 Photolithography . . . 62
8.4 DRIE process . . . 62
8.5 Sample detachment and cleaning . . . 63
8.6 PDMS sample holder attachment . . . 64
8.7 FIB milling of fracture toughness sample pre-cracks . . . 65

9 Results **66**
9.1 Film characterization . . . 66
9.1.1 Film thicknesses via ellipsometry . . . 66
9.1.2 Diameters using optical microscopy . . . 66
9.1.3 Micrographs from scanning electron microscopy . . . 67
9.1.4 X-ray diffraction results . . . 69
9.2 Young's modulus . . . 72

9.3 Residual stresses . . . 73
9.4 UTS results . . . 74
9.5 Fatigue . . . 76
9.6 Fracture toughness . . . 78

10 Discussion **80**
10.1 Implications of the XRD results . . . 80
10.2 Analysis of the Young's moduli and residual stresses . . . 81
10.3 Analysis of the UTS results . . . 82
10.4 Area or volume defects . . . 83
10.5 Effect of fatigue . . . 85
10.6 Error analysis . . . 86
10.6.1 Sample fabrication related error . . . 86
10.6.2 Sensitivity of the measurements to Poisson's ratio variance . . 87
10.6.3 Effect of diameter error . . . 87
10.6.4 Validity of the fracture toughness measurements . . . 88
10.7 Evaluation of the mechanical reliability of AlN thin films . . . 90
10.7.1 Critical defect size in the sample material . . . 90
10.7.2 Design for reliability . . . 91

11 Conclusions **93**
11.1 Future research . . . 93

References **94**

Symbols and abbreviations

Symbols

E	Young's modulus
K_{Ic}	Fracture toughness (critical stress intensity)
ν	Poisson's ratio
σ	stress (sometimes used for standard deviation)
ϵ	strain

Abbreviations

UTS	Ultimate tensile stress, also referred to as fracture strength
ICP RIE	Inductively coupled plasma reactive ion etching, a dry etching technique
DRIE	Deep reactive ion etching, a process type for RIE
AlN	Aluminum nitride
ZnO	Zinc oxide
PZT	Lead-zirconate-titanate, a piezo material
MEMS	Micro electro mechanical system
XRD	X-Ray diffraction
ALD	Atomic layer deposition, a technique for producing AlN films
MOVPE/MOCVD	Metalorganice vapour phase epitaxy, a technique for producing AlN films
SCG	Subcritical crack growth, a phenomenon affecting material strength
LEFM	Linear elastic fracture mechanics, fracture mechanics when no plastic deformation occurs
EPFM	Elasto-plastic fracture mechanics, like LEFM, but plastic deformation is accounted for
AFM	Atomic Force Microscopy, a measurement technique employing a nanoindenter to scan a surface
FWHM	Full width at half maximum of a curve
CTE	Coefficient of thermal expansion, measure of materials expansion when temperature is altered
PDMS	Polydimethylsiloxane, a material used as a sample holder in the experiments
FIB	Focused ion beam, a micromachining and imaging technique
CMOS	Complementary metal oxide semiconductor, usually used as a synonym to the processing methods used in the production of CMOS's

1 Introduction

Aluminum nitride is a ceramic semiconductor material with a wide range of applications, from high temperature windows to optoelectronics and piezoelectric actuators. [1] Thin films of aluminum nitride (thicknesses ranging from tens of nanometers to around 10 micrometers) have seen great research interest especially in piezoelectric applications. However, very little research has been conducted on the mechanical properties of these thin films. This makes design for reliability of applications, where aluminum nitride thin films are used, difficult.

The applications where aluminum nitride is used are various, and thus the dangers that a possible material failure would cause vary as well from a mere nuisance to potentially life dangering consequences. Owing to the microfabrication processes of these applications, fracture of the thin film is likely to be impossible or impractical to repair. Thus, the reliability of the thin films is of paramount interest, and a set of mechanical properties is required for the design for reliability of these applications. These properties of aluminum nitride thin films are studied through a set of experiments in this thesis.

When designing for reliability, the main idea is to approximate the stresses and strains experienced by the material in the application, and then comparing these with the known fracture strength of the material. However, this fracture strength for aluminum nitride thin films has not been studied, and thus it is measured in this thesis.

In order to accurately quantify the stresses and strains, that the thin film undergoes in the application, the Young's modulus and residual stress of the films should be known. Through use of Young's modulus of the thin film, a known strain can be linked to the stress state that the film experiences. Residual stresses add up to the effect of strain, and thus alter the actual stress in the film when a certain strain is applied. Both of these properties of aluminum nitride thin films are studied in this thesis.

As the stresses experienced by thin films in, for example, piezoelectric actuation, may be cyclic in nature, the effect of fatigue should be known for these films in order to verify that the films can withstand the stress cycles that the film undergoes during the lifetime of the application. An experiment with cyclic loading is done in this thesis.

Finally, the fracture toughness of AlN thin films is studied. Through knowledge of the fracture toughness of a material, its resilience against defects of different sizes can be assessed, and thus it can be evaluated how greatly the films are influenced by any induced mechanical damage.

The aforementioned properties of aluminum nitride are thus measured through a bulge test experiment in this thesis, with the results and their implications being reported in sections 9 and 10 respectively. The experiments are conducted on two sputter-deposited AlN thin films of different thicknesses and a metalorganic vapour phase epitaxy (MOVPE)-deposited film. First, however, it is important to understand the basic concepts related to the evaluation of mechanical reliability of a material, and these will be introduced in section 2. A brief introduction to the different micro

electro mechanical systems (MEMS), where use of AlN thin films has been studied, is given in section 2.1. The general properties of aluminum nitride are presented in section 3 and the fabrication methods used for sample preparation in this thesis are introduced in section 4. A review on the different mechanical testing methods that can be used in the study of mechanical properties is given in section 5, with some characterization methods, that can be used to study the quality and structure of these thin films, being introduced in section 6. The experimental details of the experiments done in this thesis are reported in sections 7 and 8.

2 Background

In this section, first a short introduction into how aluminum nitride thin films are used in contemporary micro electro mechanical systems (MEMS) is given. Then, the quantitative mechanical properties related to evaluation of mechanical reliability are presented, explained and their usefulness in this study is evaluated. The relevant theoretical background that is required in order to understand the results of this thesis is also given. The purpose of this section is to give insight into how mechanical reliability is evaluated in contemporary literature and thus give some basic understanding on how the results of this thesis can be compared with those reported elsewhere. Further details on how this theoretical background can be applied in the case of aluminum nitride thin films is presented in section 3. As fracture mechanics is a wide field of study and the range of applicable materials is likewise vast, the emphasis is on fracture mechanics applicable to ceramics that behave similarly as aluminum nitride.

2.1 AlN MEMS

The motivation of this thesis is to evaluate the mechanical reliability of aluminum nitride thin films, which is especially relevant for piezoelectric actuation applications where these thin films undergo significant stresses and strains. Piezoelectric actuation can be used in a variety of microelectromechanical system (MEMS) applications, some of which are presented in this section. [2]

Traditionally, lead zirconate titanate (PZT) has been the most commonly used material for piezoelectric layers. However, it suffers from deposition difficulties and poor compatibility with CMOS processes, which has hindered its use for MEMS applications. AlN does not suffer from these issues, and with its piezoelectric and acoustic properties, its use in MEMS applications has seen great research interest in the recent years. [2]

The use of AlN thin films has been studied in a wide range of MEMS applications, where capacitive silicon technology has been traditionally used. The piezoelectric properties can be used in two principal ways; either to actuate a device by applying a voltage over the piezoelectric film to cause displacement, or by sensing the induced voltage from the piezoelectric film, when the film is under strain caused by an external force. Devices that have been demonstrated using piezoelectric actuation with AlN thin films include for example resonators, filters and switches. Piezoelectric sensing with AlN thin films has been demonstrated in microphones, strain sensors, accelerometers and chemical sensors, whereas use of the films piezoelectric response has also been demonstrated in energy harvesting applications [3]. A combination of piezoelectric actuation and sensing has also been demonstrated for use in ultrasonic transducers. In addition to these, the reasonable chemical inertness and great thermal stability have spurred research for MEMS devices utilizing AlN structures for highly demanding environments, such as automotive engines and thermal power plants. [2, 4]

While there has been a large amount of research on different types of AlN

piezo applications, the main commercial success has been in thin film bulk acoustic resonators with Avago industries producing over a billion units a year [5]. Microphones that utilize AlN thin films have also been commercialized by Vesper Technologies [6].

2.2 Physics of fracture

Fracture mechanics is of principal interest in this study and in order to understand and discuss the related phenomena, it is important to clarify some basic concepts and terminology and an attempt into that is made in this section.

Fracture is defined as a non-reversible separation of material under loading. This separation occurs when the applied stress surpasses the strength of the bonds in the material. On the molecular scale, this happens when a single bond between atoms is placed under sufficient stress, the required stresses typically being in the range of tens of gigapascals. On macroscopic scale, existing discontinuities in the material will cause stress concentrations in the material and thus a lower average stress field may induce fracture in the material bulk, with discontinuities being defined as any disruptions to the perfect lattice structure. Fracture occurs when the stress concentration (stress intensity) exceeds the fracture toughness of the material. Stress concentration and fracture toughness are further discussed in section 2.4. In contrast, fracture strength then refers to the actual stress in the volume of material when fracture occurs. Fracture strength is discussed in more depth in section 2.6. [7]

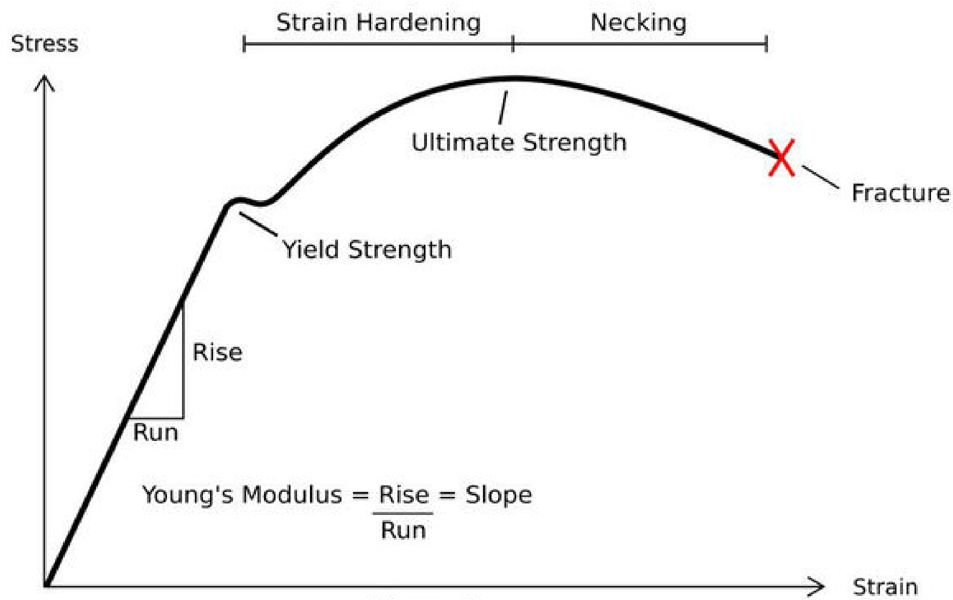

Figure 1: A stress versus strain curve with explanations for Young's modulus, yield strength and fracture strength. In the case of ceramics, fracture occurs very close to the point of yield strength, with little non-linear (plastic) deformation prior to fracture [8].

Fracture strength should not be confused with yield strength (see figure 1), which refers to the stress at which material begins to deform plastically. However, the material under research in this thesis, aluminum nitride, is known to be a brittle material, and thus little plastic deformation can occur prior to brittle fracture. Thus its yield strength is approximately the same as its fracture strength. [9]

Fractures can occur under three different loading conditions; mode I (opening mode), mode II (sliding mode) and mode III (tearing mode). Mode I fracture occurs under tensile stress, whereas modes II and III occur under shear stresses of differing orientations. The modes are visualized in figure 2.

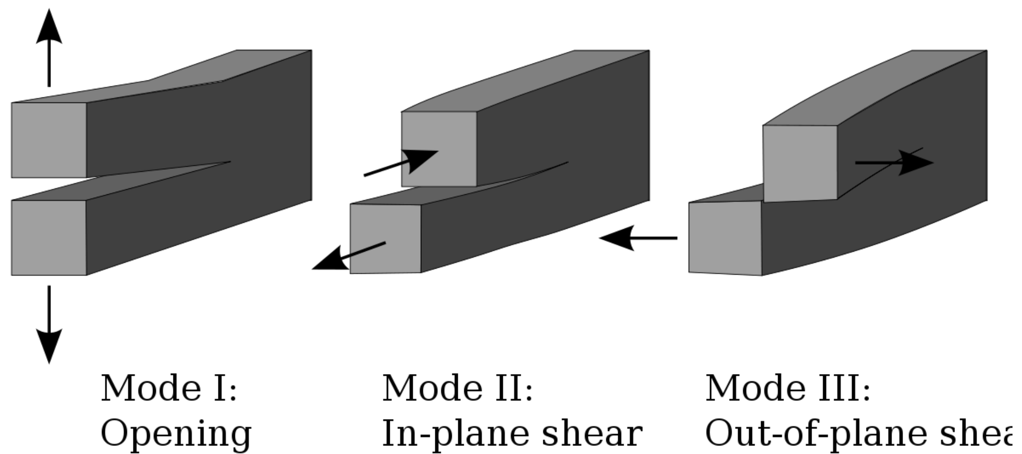

Figure 2: Fracture modes. [10]

In this study, the primary interest lies in studying mode I fracture and effort is made to minimize shear stresses in the testing setup so that reliable results for ultimate tensile stress and fracture toughness of mode I fracture can be obtained.

Fracture mechanics itself is divided into the so called linear-elastic fracture mechanics (LEFM) and elastic-plastic fracture mechanics (EPFM). In LEFM, it is assumed that plastic deformation is insignificant and the area close to crack tip that plastically deforms (explained in more detail in section 2.4) is minor compared to the size of the crack itself, which is a reasonable assumption in brittle materials that show close to nonexistent plasticity. In contrast, EPFM is a modification of LEFM that takes into account plastic deformation of the crack tip prior to fracture. As a brittle ceramic material is studied in this thesis, EPFM is discussed in less detail and it is assumed that LEFM conditions persist and the fracture toughness discussed and measured in this thesis is the linear elastic fracture toughness of aluminum nitride. However, as fracture properties of aluminum nitride thin films are not well studied, it is a possibility that plastic deformation can be in play in its fracture mechanics, and some insight into fracture mechanics under EPFM is given in sections 2.8 and 2.9.

2.3 Young's modulus

Young's modulus, also known as the elastic modulus, defines how material elastically deforms under applied stress. Elastic deformation means deformation, which is reversed when the stress is removed. Young's modulus defines the ratio of stress to strain of a material and thus its unit is pascals, however common materials have their Young's moduli in the gigapascal range. Young's modulus is formally defined as:

$$E = \frac{\sigma(\epsilon)}{\epsilon}, \tag{1}$$

where E is the Young's modulus, $\sigma(\epsilon)$ is the stress in the direction of strain and ϵ is the strain (the elongation) of the material.

Young's modulus defines the elongation of a volume in the direction of applied stress and when this kind of a tensile stress is applied on a volume, it causes compression of the volume in directions perpendicular to the direction of applied stress. The ratio between the strain in the direction of stress to the compressive strain in a direction perpendicular to the applied stress is called Poisson's ratio and it is denoted as ν. In this thesis, an important parameter is a so called biaxial modulus, which describes the elastic deformation of a thin film under biaxial (equal stress in two perpendicular directions, in the case of thin films the stresses are in the length and width directions) plane stress (plane stress is discussed in section 2.4) and equation (1) is the following in these conditions:

$$\sigma_{xy} = \frac{E}{1 - v}\epsilon_{xy}, \tag{2}$$

where $E/(1 - v)$ is the biaxial modulus.

Crystal lattices are often anisotropic in nature and thus Young's moduli of crystalline materials usually depend on the direction at which stress is applied on the crystal. Thus, one value is not enough to define a crystals elastic response to stress, and a set of elastic constants is required. When considering bulk polycrystalline material with mixed crystalline orientations, Young's modulus represents response of the whole volume to stress and the elastic constants in different crystalline orientations are of little importance. However, with materials with grain sizes close to the critical dimensions of the material, the differences between elastic constants in different lattice directions will play a bigger role. [11]

When evaluating mechanical reliability of a material, Young's modulus plays a key role as it is used to link stress with strain, when either of those two is known. Thus, Young's modulus is vital in calculation of stresses that these films experience during use so that the fracture strength of the material is not exceeded. For this reason the Young's modulus of aluminum nitride thin films is measured, with results presented in section 9.2.

2.4 Fracture toughness

Fracture toughness (K_{Ic}) is defined as the stress intensity at a crack tip singularity that will cause this crack to propagate. Essentially, the value of fracture toughness represents the ability of a given material to resist propagation of cracks or defects found in the material [12]. Fracture toughness is an intrinsic property of a material deriving from the interatomic bonds of the material, and it can also be used to derive a so called critical defect length (a size of an ideal crack that would cause failure) at a given stress level. Thus, when fracture toughness is known, it can be used to extrapolate the effect of defects on a given materials mechanical reliability. Principally, it is the most important mechanical material parameter of brittle materials as it defines the fracture properties of a material. In contrast, fracture strength, (further discussed in 2.6), varies depending on the intrinsic properties of a material, such as grain size and defect density.

Fracture toughness is measured in (mega)pascals per square root meters ((M)Pa·$m^{1/2}$). As it effectively measures the ability of a material to resist brittle fracture, the higher the value, the more ductile the material tends to be, with plastic materials exhibiting highest fracture toughnesses. Fracture toughnesses of brittle materials such as glass or single crystal materials are commonly very low, down to 0.5 MPa·$m^{1/2}$. Ceramics also exhibit relatively low fracture toughnesses, most commonly in the range of 2-5 MPa·$m^{1/2}$, whereas metals can have values ranging from 15 to up to 150 MPa·$m^{1/2}$. [13]

The critical stress intensity around the crack tip in mode I loading conditions can be generally derived from the applied stress on the crack through the following equation:

$$K_{Ic} = \sigma_c \sqrt{\pi a} Y \left(\frac{a}{W} \right), \quad (3)$$

where K_{Ic} denotes mode I (tensile) critical stress intensity factor at crack tip singularity, σ_c denotes critical stress on the whole crack and a is the half-length of the crack (follows from the geometry of stress concentration at crack tips). The $Y(\frac{a}{W})$ is a geometrical constant that can be used to take into account the effect of differing specimen geometries on the stress field induced on the crack. This constant is close to unity for plane stress geometries [14]. Materials generally have a differing fracture toughness depending on the loading mode (following from anisotropic crystal structures) and thus mode I, mode II and mode III fracture toughnesses have distinct values. However, in this thesis, only mode I loading is discussed and measured, and thus only K_{Ic} is considered.

Equation (3) can also be used, once UTS and fracture toughness of a material are measured, to calculate a critical crack length, which describes the size of an ideal crack, positioned perpendicular to the direction of applied stress, that the material can withstand at this stress level. This can be used to extrapolate the sensitivity of the material to defects and thus to defects caused by fabrication processes or mechanical wear in use.

In this study, the testing setup is done so that only purely tensile stress fields are induced and thus the stress intensity factors K_{II} and K_{III} are taken as zero.

Hence, these factors will be left out of consideration, as is also predominantly done in contemporary studies. It should also be noted that the stress intensity factor is only valid in LEFM conditions where no plastic deformation occurs at crack tip prior to fracture, and thus the effective crack length does not change until the critical stress intensity is reached. [15] This should be a valid assumption for the material under investigation in this study (due to the brittleness of AlN) and the cases where plastic deformation would occur are discussed shortly in the section 2.9.

In essence, there are two distinct conditions under which fracture toughness can be evaluated, called plane stress and plane strain conditions (often also misleadingly named plain stress and plain strain conditions). In continuum mechanics, plane stress is mathematically defined as the situation where one of the principal stresses (stresses in x, y and z directions) is 0 (no constrainment of material is present in one direction). Material is then under plane strain when strain in one of the principal directions is 0 (material is fully constrained in at least one direction). In both cases, stress states are reduced to a simpler 2D-form and thus the calculations are simplified. The conditions are visualized in figure 3. The conditions are further discussed from an engineering point of view in the following text, with the case of fracture toughness under these conditions being under primary consideration. The material interaction behind these conditions is as well further discussed in section 2.12.1.

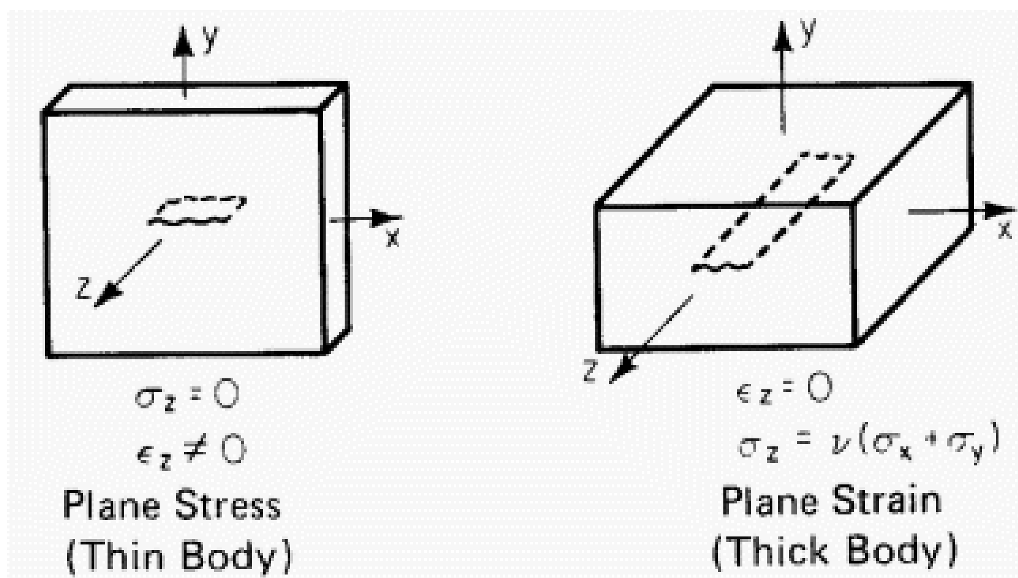

Figure 3: Plane stress and plane strain conditions visualized. [16].

Plane strain condition states that the thickness (or some other critical dimension in some cases) of the sample under testing is large enough so that the plastic deformation zone around the crack tip, from now on named the plastic zone, is negligible compared to the actual thickness of the sample. Plastic zone is defined as the area around crack tip where the induced stress field causes plastic deformation of the material, which, although small, is still non-zero even for brittle elastic materials.

The sample thickness B required for plane strain condition to be met is described in the ASTM E399 standard criteria given by the following equation:[17]

$$B_I = 2.5\frac{K_{Ic}^2}{\sigma_{ys}^2}, \tag{4}$$

where σ_{ys} denotes yield stress of the material, which, for brittle materials, is very close to its fracture stress σ_c. With knowledge of the range of UTSes and fracture toughnesses of brittle ceramic thin films, this condition is very likely not met in the case of this thesis and so the measurements are thus done in plane stress conditions. [12]

Plane stress condition states that the plastic zone thoroughly penetrates the whole thickness of the sample under testing and thus no constraint of contraction is present. The conditions are described by the following equation:[14]

$$B_0 = \frac{K_{1c}^2}{3\pi\sigma_{ys}^2}. \tag{5}$$

The plane stress condition can be met when the thickness B_0 of the sample is below the approximate value given by equation (5).

Fracture toughness at plane strain is always lower than the fracture toughness at plane stress conditions. This follows from the fact that under plane stress the plastic zone is not restricted by material as it penetrates the whole thickness of the sample. In plane strain, the material around the plastic zone supports the plastic zone, and so prevents the deformation of the plastic zone. With highly brittle and predominantly elastically deforming materials this difference is minor (in the order of few percents) as is discussed in [14]. Nevertheless, the stress state should still be evaluated when discussing fracture toughnesses so that results from plane stress and plane strain conditions are not mixed.

The fracture toughness under plane stress conditions is linked to fracture toughness under plane strain (K_{Ic}) through the critical energy release rate G_c. Critical energy release rate is the amount of energy dissipated in the process of crack propagation and is measured in J/m^2. In some cases, it is easier to obtain from measurements, namely when using the so called *energy approach*. The critical energy release rate can be used to obtain K_{Ic} for both plane stress and plane strain conditions through the following equations (6) and (7), respectively. [15]

$$G_c = \frac{K_{1c}^2}{E}, \tag{6}$$

$$G_c = \frac{K_{Ic}^2(1-\nu^2)}{E}. \tag{7}$$

It can be seen that the difference with common Poisson's ratios in the range of 0.15-0.3 would yield a difference of 2.3-9 % between the plane stress and plane strain energy release rates.

Critical stress intensity factor under plane stress should be denoted as K_{1c} as it differs from the case under plane strain (which then should be denoted as K_{Ic}) [7]. However these are often mixed in literature and notation K_{Ic} is also used for plane stress conditions. It should be noted that as the application under interest

here should be under plane stress conditions, the measured value will be K_{1c} of AlN. However, the notation K_{Ic} will nevertheless be used in this thesis in order to keep the content in line with contemporary literature.

As discussed in this section, fracture toughness is the principal material parameter that governs the fracture properties of a given material type. It can be used to assess the effect that defects have on a materials fracture strength, and thus it is a valuable parameter, which will be measured in this thesis for aluminum nitride thin films.

2.5 R-curve behaviour

Fracture toughness is generally defined so that it follows equation (3) and thus it is an intrinsic property of a material, independent of crack lengths. However, in some cases, fracture toughness varies depending on the length of the crack. This kind of a response is called R-curve behaviour. As a result, the fracture toughness of such a material can not be characterized using a single value. [18]

R-curve behaviour is mainly explained by two distinct toughening mechanisms; transformation toughening and crack bridging. Transformation toughening refers to the effect, where free surface produced by cracks onsets the transformation of a materials metastable phase to a stable phase, thus inducing changes in the material morphology during crack formation. In crack bridging, the material includes ligament-like structures, that, when cracking occurs, are "left behind" in the cracks wake to bridge the crack edges together, inducing a closing force on the crack. The ligaments can be, for example, whiskers, fibers or elongated grains trapped in the material. [9]

Both transformation toughening and crack bridging induce a closure force on formed cracks, which then results in a change in fracture toughness depending on the crack length where closure force is present. The zone in the crack wake that is affected by transformation or bridging will usually increase to a certain extent, after which it stays constant (for example whiskers fracture at the same phase as they are formed) and thus the R-curve settles at some constant value at some crack length. [9]

The general implications of R-curve are that the material can resist even larger cracks without fracturing (ie. its UTS remains high even with larger defects), which then naturally results in higher reliability. However, it has been noticed that R-curve behaviour results in increased fatigue susceptibility, most likely due to cyclic fatigue opening and closing the cracks and thus destroying the bridging material. This can potentially induce crack extending forces, when the bridging material is trapped between the closing crack, which can exert an opening force on the crack tip. [9]

R-curve behaviour in aluminum nitride has not been studied, so its possibility cannot be directly dismissed. However, while knowing the toughening mechanisms and aluminum nitrides general material properties, it is highly unlikely that such an effect can be found. Thus, studying R-curve is out of the scope of this thesis.

2.6 Ultimate tensile strength

Fracture strength is defined as the stress level at which fracture propagation occurs in a material. When discussing tensile stresses (stresses acting in the direction that elongates the material, as opposed to compressive stresses), the name ultimate tensile strength (UTS) is used to notify that the value denotes strength under tensile stresses. Thus, UTS is the measure of actual tensile stress in the material volume at point of fracture, which is mostly catastrophic in nature in brittle materials. Essentially, UTS defines the stress limits that a certain material volume can withstand, and thus it is a measure of how fracture toughness acts in a sample with a certain defect distribution. [7]

As noted in section 2.2, brittle materials generally cannot relieve stress concentrations on defects and cracks through plastic deformation, and thus catastrophic fracture occurs when fracture toughness is exceeded somewhere in the material. Thus, the UTS is related to the fracture toughness of the material through equation following equation:

$$\sigma_c = \frac{K_{Ic}}{\sqrt{\pi a}}, \tag{8}$$

which can be used to calculate the UTS of a material with a known critical crack size when fracture toughness is known. When both fracture toughness and UTS are measured, the critical crack size that causes fracture in the tested material can be assessed.

Due to the aforementioned nature of brittle fracture, UTS is largely dependant on the intrinsic defect distribution in the material volume or area (defect distributions may either scale through area or volume, which is further discussed in section 3.2, however for simplicity only volumes are considered in this text). When differing volumes of material with the same defect distributions are studied, the statistical probabilities associated with the distributions come to effect; a smaller volume has a smaller chance of containing a larger critical defect and vice versa. Subsequently, when testing a set of equally sized samples, the measured UTSes will vary to some extent due to these probabilities, and thus only a probability of failure at a certain stress level can be given. An average value can be calculated from the set of measured UTSes, but it does not assess the distribution of UTSes in the sample set and for this reason, Weibull distributions are used when presenting and analyzing results from UTS experiments. These statistical methods are presented in section 7.4 and the effect of microstructure of a material on its UTS is further evaluated in section 2.12.2.

UTS thus depends on the fracture toughness, the defect distribution and the volume or area of the material in question. Thus it is not an intrinsic property of the material substance itself, but rather is only the same for materials of the same substance with the same defect distributions. However, when defect distributions can be evaluated, the UTSes can be extrapolated for different volumes or areas of the material (see section 7.4), and thus it is a useful parameter for estimation of mechanical reliability in applications and it will be measured in this thesis.

2.7 Anelasticity

Anelasticity is the time-dependant elastic deformation of a material. There are various types of effects that can cause time-dependancy of elastic deformation and the effects depend greatly on the material type involved. Anelastic effects generally fall into two categories, those caused by the so called thermoelastic effect and those caused by internal friction. In the case of this thesis, more interest lies in the types of anelasticity caused by internal friction as testing temperatures will be constant. [11]

The internal friction related effects depend on the limited speed at which dislocations can move in a material, due to friction. There are two types of identified internal friction related phenomena that are proven to cause anelasticity. These are bowing of dislocations and grain boundary sliding. [19] More evidence is also presented in [20], that defects may produce anelastic response in a material.

However, very little research has been conducted on how large these effects may be in ceramic materials, especially in specimens with very small dimensions. Thus, as the scale of these effects cannot be assessed, effort is rather made to minimize their possible effects. Small strain rates are thus used in the testing so these effects cause no variation in the results.

2.8 Crack tip opening displacement

Crack tip opening displacement (CTOD) is a parameter sometimes used to describe fracture toughness of a material, and sometimes it is used as a mean for derivation of the actual fracture toughness K_{Ic}. CTOD is essentially the measure of how wide a crack tip is under certain stress condition, taking into account crack blunting and crack tip plastic zone, which allows for its use in EPFM conditions. Crack opening displacement (COD), which is a measure for crack width at the center of a crack, is also occasionally incorrectly mixed with CTOD. [7]

CTOD can be directly linked to K_{Ic} in linear elastic fracture mechanics (LEFM) conditions through the following equation:

$$CTOD = \frac{4K_{Ic}^2}{\pi E \sigma_{ys}}, \tag{9}$$

where K_{Ic} is the fracture toughness, E is the Young's modulus and σ_{ys} is the yield stress. This equation is a generalization in a rather ideal situation, with a well modeled crack geometry, which may not hold with non-ideal cracks. The equation can also be modified to include plastic deformation [7].

CTOD measurements in ceramics can generally prove difficult as catastrophic brittle fracture occurs with very little crack extension, and hence only microscopic crack opening can be seen prior to fracture. Very powerful *in situ* imaging would be required and thus measurement of CTOD is not viable or necessary in this thesis as K_{Ic} can be directly measured.

2.9 *J*-integral

When LEFM conditions are not satisfied and plastic deformation takes place at a crack tip, the LEFM fracture toughness does not apply. The elastic strain energy release rate G_c in equation (6) has to be corrected with a plastic parameter, denoted as J_{pl}, which is given by the following equation: [18]

$$J_{pl} = \frac{H\sigma^{n+1}a}{F}, \tag{10}$$

where H is a geometrical constant dependant of the loading geometry, n is a so called hardening exponent, a is the crack half width and F is the effective Young's modulus in the plastic region, although the elastic Young's modulus is sometimes used as well.

The J-integral is then defined as:

$$J = G_c + J_{pl}, \tag{11}$$

which can also be written as (under mode I loading):

$$J = \frac{K_{Ic}^2}{E} + \frac{H\sigma^{n+1}a}{F}. \tag{12}$$

The J-integral is thus the elastic-plastic strain energy release rate, which can be used as a measure of fracture toughness in elastoplastic materials, and in these cases it is called the critical elastic-plastic strain energy release rate or J_c. In cases under LEFM conditions, J_c is the critical elastic strain energy release rate and thus directly connected to K_{Ic}.

In this thesis, the material under investigation is reasonably well studied and confirmed to behave in a brittle elastic manner [21]. Thus, the J-integral is not required in order to describe the fracture toughness of aluminum nitride thin films unless plastic effects are observed in the measurements.

2.10 Residual stress

Residual stress is defined as a stress state that is left in a material after the original cause of that stress is removed. For example, in thin film fabrication, lattice mismatch, thermal gradients and mismatch of coefficients of thermal expansion (CTE) between the film and the substrate can leave the film in a stressed state after the actual fabrication process is finished. The stress states can be either tensile or compressive, with different implications on the materials mechanical reliability. [9]

Residual stresses affect the way a film responds to mechanical loading as can be seen for example in the equations presented in section 7.2.1. With thin films commonly being on top of substrate materials, bending of the substrate applies a strain on the film. The strain thus applies a stress on the film and if tensile residual stresses are present in the film, the residual stress causes the total stress state to be higher than that of the situation with no residual stresses. With compressive residual stresses, the stress in the same case would thus be smaller. Thus, in order

to accurately quantify the stress state in the film, the residual stress state of a film should be known when using these films in applications.

Due to the nature of formation of residual stresses, it should be noted that the stress state may not be uniform throughout a thin film specimen. In the case of CTE- and lattice mismatch related residual stresses, the stress is highest in the substrate-film interface and is possibly relieved through formation of dislocations when going closer to the film surface, depending on the thickness and the material of the film, which is discussed further in section 3.2. [22]

The residual stresses left in thin films are dependant of the deposition process used and thus they will be further discussed in the section 4.

2.11 Fatigue

Fatigue is defined as changes in the microstructure of a material under constant or cyclic applied stress. When considering fatigue in ceramics, it is important to distinguish between the different phenomena that cause similar changes in material strength, ie. cause fatigue in the material. The main phenomena in ceramics are creep, sub-critical crack growth (SCG) and actual dynamic fatigue. [9]

Creep is the time dependant deformation of material under static stress conditions, which is usually enhanced by near melting point temperatures. The mechanisms of creep are various and complex, although it generally includes all mechanisms, where atoms of a material seek to deform in order to relax their stressed state, be it through diffusion or viscous flow for example. Creep in ceramics is generally extremely slow at room temperature and thus in the scope of this thesis it can be considered negligible [23]. [9]

Sub-critical crack growth means extension of a crack via chemical reactions at crack tip. Stress concentration at the crack tip enhances the chemical reactivity of the material under stress, thus making cracks prone to extend in a reactive atmosphere. SCG naturally depends on both the stress concentration and the concentration of a reactive species available at the crack tip. In the case of SCG, the reactivity of the material to water or oxygen should be assessed to determine whether it is susceptible to this kind of fatigue in common atmospheric conditions. [9]

Dynamic fatigue means fatigue under dynamic loads, most commonly meaning loads of cyclic nature. The common mechanism of cyclic fatigue damage is the propagation of microcracks, which naturally degrade the material strength (as can be seen from equation (3)). However with ceramics, low fracture toughness and plasticity usually allow for no extension of microcracks, but rather when critical stress concentration is reached, the cracks extend catastrophically. However, the mechanisms of cyclic fatigue may vary (well explained in [24]) and for example materials exhibiting R-curve behaviour (see section 2.5) seem to be more susceptible to cyclic load damage, although the mechanism of damage is different than in common cyclic fatigue. Thus, microcrack propagation may cause fatigue changes in AlN thin films. [9, 24]

Dynamic fatigue is usually separated into low cycle and high cycle fatigue. By definition, high cycle fatigue usually means fatigue damage at loads that cause no

plastic damage and cycle amounts of $>10^4$. On the other hand, low cycle fatigue is fatigue under sufficiently high loads for plastic deformation to occur, and cycle amounts being under 10^4. In ceramics, even though plastic deformation is considered to be negligible prior to brittle fracture, fatigue damage has been reported at 10^6 cycles at 60-80 % initial fracture strength [25].

Even though general material knowledge would hint that no cyclic fatigue changes should occur in aluminum nitride due to its ceramic nature, there are conflicting reports from how other ceramics respond to cyclic loads, and thus it is of high interest to experimentally verify what is the case with AlN thin films. Naturally, as the deposition methods and fabrication processes used for production of AlN thin films vary, the structural properties of these films vary as well (for example crystallographic composition and defect composition). The variance in structural properties can result in variable response to cyclic loads.

2.12 Thin films versus bulk material

Thin film materials stand apart from their bulk counterparts in various ways. The apparent properties of thin films follow from both geometrical reasons and differences in material structure, which are partially explained by different deposition methods used for production of thin films versus such of bulk materials.

As the total effect of thickness on materials mechanical properties is of interest, the geometrical influence is first evaluated in section 2.12.1, after which material property effects are discussed in section 2.12.2.

2.12.1 Geometry effects

The first effect of material thickness is its geometry. When considering thin films, usually the the thickness of the films becomes more and more negligible compared to the width and length of the material. This leads to changes in how stresses act in the material, and causes the transition from plane strain state to plane stress state (discussed shortly in section 2.4. Stress is distributed through interactions between material molecules and so the aforementioned transition is easiest explained via molecular interactions.

When looking at a crystal structure, when a tensile force in x direction is applied on one particle in the crystal lattice, the particle pulls the surrounding particles in the crystal with it also in directions y and z. For this reason, a force applied in one direction results in forces acting in all directions in the crystal, with Poisson's ratio defining the ratio of these stresses. The crystal deforms depending on its elastic-plastic properties; if the bonds in question allow it, the distance between each particle is slightly increased and a so called elastic deformation takes place. If the bonds break, a plastic deformation takes place. Plastic deformation takes place when the applied stress on the bond between particles surpasses a critical limit, the so called yield stress σ_{ys}. However, when there are surrounding particles, the particles being stressed are supported by the surrounding particles, which reduce the strains experienced by them and thus constrain the plastic and elastic deformation. [7]

Now we can move back to the greater picture. In a bulk material, the stress is spread in all directions of the material when a tensile stress is applied. The material surrounding the stressed area constrains the deformation of this area and thus the area where stress is applied experiences stresses in y and z directions as well. This results in a greater total stress under this so called plane strain condition, where there is enough surrounding material to fully constrain this strain and thus it can be taken as zero. [7]

Now in practice with brittle materials such as AlN, the zone of stress distribution or the so called plastic zone is in the range of micrometers [12]. When stress is applied on a film that is thinner than the plastic zone that the stress would produce, the stress cannot be distributed further in the z-direction and so particles close to the origin of force are free to deform. This deformation results in a smaller total stress experienced by the thin film under this so called plane stress condition, which then leads to it apparently being able to withstand greater tensile forces without fracture. As previously explained, the actual strength of the material does not change, but the way stress and strain act and distribute in the material do, and thus this kind of a thin layer can withstand greater stresses in real world applications as well as long as the layer is not constrained by its substrate or any layers on top of it. However, the impact of this condition for brittle materials has been found to be fairly negligible in practice, in the order of few percents [14].

2.12.2 Material properties

Another aspect to be taken into account is the material structure. As fractures nucleate predominantly from discontinuities in brittle materials, the structure of the material under question is of great influence. Material properties that affect the fracture mechanics of a crystalline brittle material are first of all its crystallinity and orientation of the said crystals, and in the other hand also the grain size of the crystals, as due to the anisotropic nature of the mechanical response of crystallites, these define the stress-strain relationships in the material. In addition to these properties that can usually vary with no regard to materials dimensions, materials in the real world always include defects of different types, such as dislocations, cracks and voids of varying sizes and material imperfections and impurities. As defects cause stress concentration and thus dominate the fracture nucleation in a brittle elastic material, the defects have a large influence when going down to smaller film thicknesses. Often it is assumed that defects are equally distributed throughout the volume of a material, but the case may as well be in thin films that the distribution of defects large enough to dominate fracture behaviour may rather scale through the area of the film under testing (due to the nature of defect formation). However, for simplicity, in the following text it is assumed that critically sized defects are equally distributed throughout the volume of the film, while the same concepts can be used for films with defect distributions scaling with area. [9]

It can be said that defects are always produced in a material depending on the fabrication process used, and cannot be completely avoided. Generally, a material consists of a certain density of a varying set of defects depending on the fabrication

method and parameters used, and thus the defect distribution produced in a certain fabrication process is often independent of the film thickness (this is a generalization and the actual quality of films produced via different deposition methods is further assessed in section 4). What does change though, is the volume of the material produced. If we take the amount of critically sized defects (defects of the largest size found in the material that dominate fracture nucleation) per unit of volume as a constant, when we decrease the thickness of the material by 50 %, the volume will change in the same ratio. Now, the probability of finding a critically sized defect is also halved, if defects are equally distributed throughout the volume. As defects are the predominant source of fracture nucleation in brittle solids, and they directly influence the UTS of the material, and from the previously stated follows that the UTS should increase when decreasing the film thickness. [9, 26]

An equation is derived through Weibull statistics to relate the volume change of a material to the change in UTS: [9]

$$\frac{\sigma_{comp}}{\sigma_{test}} = \left(\frac{V_{test}}{V_{comp}}\right)^{1/m}, \tag{13}$$

where σ_{comp} is the UTS (Weibull shape parameter) to be calculated, σ_{test} is the UTS (Weibull scale parameter) of the tested sample set, V_{test} and V_{comp} the volumes of those material specimens and m is the Weibull modulus of the tested material that can be found through UTS testing (further explained in section 7.4).

Due to the way defects are formed in a material (which will be discussed further in section 3.2), defect distribution may as well scale through area rather than volume. In this case, the areas of the specimens can be used in equation (13). Through use of this equation with measurements from multiple film thicknesses, it can be evaluated, whether the UTS of the thin films scales through area or volume, and thus whether critically sized defects are distributed in the area or volume of the film.

The change in UTS through area or volume difference is purely due to statistics, and when talking of testing of thin films, the probability of having defects in the volume under testing will be smaller. However, defect distribution may also have a greater statistical variance when the film thickness decreases, depending on the density of the defect distribution. This can result in a greater variance in measured UTSes, although at the same time the average UTS should increase according to equation (13). This has great effect especially when going down to the nano scale and for example, as is noted in section 3.1.1, the UTS of bulk AlN for example is approximately 265 MPa [27], whereas its theoretical limit from *ab initio* calculations is 50 GPa [28]. Now, when decreasing the thickness of the tested film, the UTS can possibly grow from 265 MPa all the way up to 50 GPa, if an ideal defect-free single crystal film structure is reached. The volume effect is one of the most important aspects of this study; the UTS at the thicknesses of 100-1500 nm, which are of interest in our particular applications, will be studied. [29]

Another material effect when going down to small thin film thicknesses is that the grain size of the material at hand most likely reaches somewhere close to the actual thickness of the film. The commonly known Hall-Petch effect and inverse Hall-Petch effects are related to the grain size of the material. These are not exactly related

to the thickness of the material at question, but rather to its fabrication process parameters. What is interesting though, is when the material thickness and its grain size coincide. As is stated in the section 3.1.1, for use as piezoelectric actuators, a wurtzite structure with its crystalline columnar orientation being in the direction of the film thickness is preferred. Now, when the crystalline columns penetrate through the whole thickness of the film, a single grain boundary then connects both the surface and the bottom of the film. This allows for more dominant grain boundary sliding to occur, which then can possibly decrease the ultimate tensile stress the film can withstand, as fractures can occur and propagate on grain boundaries more easily than in crystal material.

An effect more related to the deposition technique and substrate used is the formation of a transition zone close to the substrate-film interface, where the lattice mismatch between the substrate and thin film material causes greater dislocation activity. The transition zone is generally dependant of the fabrication process used, and its thickness is constant when same process parameters and substrates are used. Thus, when decreasing the thickness of the deposited film, the proportion of the transition zone to the thickness of the sample will increase and thus the transition zone may have a larger effect on the fracture properties and elastic response of the thin film. This will be further discussed in section 3.2. [22]

It has also been noticed that Young's modulus may vary when testing thin film samples. This has been accounted to differences in fabrication methods and mainly to the fact that the size of the defects reaches a larger portion of the critical dimensions of the film and thus the defects have more effect on the elastic deformation of the thin film. [26]

As a conclusion, both geometry effects and material structure related effects increase when materials thickness is reduced. However, it is likely that materials structural properties dominate the response, while geometrical effects should be thought of when assessing stresses and strains experienced by the thin films. The structure of thin films deposited through various methods will be further discussed in sections 3.2 and 4.

3 Research material

The focus of this thesis is to evaluate the mechanical reliability of aluminum nitride thin films. Naturally, the fundamental mechanical properties of a substance are what dictate how the material responds to mechanical loads, and thus in this section the fundamental properties of the materials studied in this thesis are assessed. A literature study is conducted in order to find measured values for the mechanical properties of aluminum nitride, so that the findings in this study can be compared with those found in literature.

Although the material under investigation in this thesis is aluminum nitride, the properties of deposited thin film layers are greatly affected by the substrate material used and thus the relevant properties of the substrate material used in this thesis, silicon, are discussed as well in section 6.

As discussed in section 2, defects and their distribution have a great effect on the mechanical properties of a material, especially in the case of brittle elastic materials such as aluminum nitride. Thus, the way defects form and how the defect distribution exactly affects the measured material properties in this thesis is discussed in section 3.2.

3.1 Materials and their relevant properties

3.1.1 Aluminum nitride

Aluminum nitride is a wide band gap semiconducting ceramic material. It has a very high thermal conductivity and in addition to this it exhibits piezoelectric properties. [30] Due to these promising properties, its use in a wide variety of applications has been studied, such as sub-ultraviolet surface acoustic wave filters [31], piezoelectric MEMS resonator structures [32], piezoelectric ultrasound transducers [33] and acoustic, force and acceleration sensing applications [34].

Under ambient conditions AlN takes a wurtzite crystal structure. The phase transition to its rock salt-cubic phase only undergoes at over 16 GPa pressure, which ensures that in most practical applications it is under its wurtzite phase. [35] The wurtzite crystal structure, and the hexagonal pillar geometry produced by this crystal structure is visualized in figure 4. The lattice constants, which represent the inter-lattice-point distances in different directions of the crystal, are 0.498 nm in the c-axis direction (direction of the centerline of the hexagon in figure 4) and 0.311 nm in a-direction (direction perpendicular to c-axis). [36]

The piezoelectricity of AlN is strongest in its c-axis orientation (the axis of the center of the hexagonal crystallite) and thus poly- or single crystalline films with the c-axis of the columnar grains oriented perpendicular to the film surface are preferred in piezoelectric applications. [33] The deposition processes that can be used to produce these kinds of aluminum nitride thin films are discussed in section 4.

The fundamental mechanical properties of AlN have been investigated through *ab initio* simulations. *Ab initio* calculations are a bottom up method where the fundamental interactions between atoms and molecules are simulated in order to model their interactions. Such a model was used to model AlN under tension and

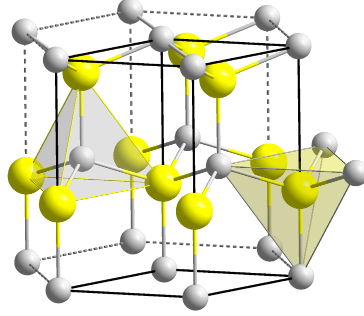

Figure 4: Wurtzite crystal structure of AlN, with Al atoms in grey and N atoms in yellow. [37]

its Young's modulus and yield strength were obtained as 208 GPa and 50 GPa, respectively. [28] The calculations were made in the direction of the hexagonal crystalline pillar (the c-axis of AlN lattice). These are however far from the ideal world where material defects and imperfections play a significant role in the actual performance of the material, and thus should be only taken as a theoretical upper limit.

The hexagonal crystal structure of AlN results in the crystal having anisotropic mechanical properties between its c-axis direction and 002-plane (the plane in the direction of the a-axis) axes; it deforms differently depending on the orientation of the applied stress. In this thesis, the films are proven (in section 9.1.4) to consist of crystal grains oriented primarily with their c-axis towards the film surface and thus the properties measured in this thesis are primarily influenced by the elastic constant and Poisson's ratio in the 002-plane of the crystal. The anisotropic nature can be seen from the elastic constants reported for aluminum nitride, presented in figure 5.

Bulk aluminum nitride has reasonably well established mechanical parameters with a 345 GPa Young's modulus and 265 MPa flexural strength (special case of fracture strength under bending tests) being reported. [27]

	C_{11}	C_{12}	C_{13}	C_{33}	C_{44}	B
Measurements by Tsubouchi *et al.* (Ref. 16)	345	125	120	395	118	201
Measurements by McNeil *et al.* (Ref. 17)	411±10	149±10	99±4	389±10	125±5	210
Calculations by Ruiz *et al.* (Ref. 10)	464	149	116	409	128	228
Calculations by Kim *et al.* (Refs. 11 and 12)	(398)	(140)	127	382	(96)	218
Present calculations	396	137	108	373	116	207

Figure 5: Elastic constants for wurtzite aluminum nitride, both calculated and measured results in GPa. [38]

Due to the anisotropy of AlN crystal structure, its Poisson's ratio varies depending on the crystalline orientation. The measured values for Poisson's ratio of AlN vary from 0.177 to 0.255. [39] A value of 0.207 is reported for single crystal AlN [40],

which should be a suitable value for the films used in this thesis, and thus it will be used as Poisson's ratio unless otherwise mentioned. The effect of Poisson's ratio variance will be discussed in section 10.6.2, although it can be said that it generally has a reasonably minor effect in calculation of material parameters.

As thin film materials are distinguished from their bulk counterparts through geometrical effects and material structure related effects as discussed in section 2.12, the literature values most applicable in the case of this thesis are ones obtained from thin film samples. There is a reasonable amount of study on the Young's moduli of these thin films, and a compilation of results found in literature is presented in table 1.

Table 1: Young's moduli reported for AlN thin films in literature with test types, deposition methods, substrates and thicknesses listed for reference.

Ref.	Test type	Deposition type	Substrate	Thickness	E (GPa)
[41]	Resonant beam	ALD	Si[100]	$\sim$ 20 nm	68
[42]	Nanoindentation	Sputtered	Si[100]	180 nm	104-115
[43]	Nanoindentation	Sputtered	Si[100]	530 nm	175.2
[44]	Nanoindentation	Sputtered	c-plane sapphire	400 nm	243.5
[45]	Nanoindentation	Sputtered	Si[111]	$\sim$ 400 nm	223.92
[46]	Nanoindentation	Sputtered	Al/Si[100]	2200 nm	225
[47]	Nanoindentation	Sputtered	Si[100]	420 nm	296
[48]	Nanoindentation	Sputtered	Si-doped GaN template	400 nm	332
[49]	Nanoindentation	Pulsed laser	Si[111]	300 nm	320
[50]	Bulge	Sputtered	Si[100]	100-1200 nm	209-252

Residual stresses in aluminum nitride thin films vary greatly depending on the deposition process and only results for very similar deposition conditions are relevant. Tensile stresses of around 1-1.5 GPa have been reported for MOVPE AlN films of 400 nm thickness on Si[111]-substrates in [51] and for sputtered AlN films on Si[100]-substrates with thickness in the range of 100-1200 nm, tensile residual stresses of 206-350 MPa have been reported [50].

There is no study as of now on the UTS of aluminum nitride thin films. Thus no literature values can be presented and it is of great interest to conduct measurements of our own.

The fatigue effects in aluminum nitride are likewise poorly studied. However, one study could be found where fatigue related failure was observed in resonator structures with AlN thin films [21]. The study thus points out that fatigue effects exist in aluminum nitride thin films, although little knowledge of the actual fatigue mechanisms in effect can be found. Thus it is interesting to conduct a fatigue study to see if the effects seen in [21] can be confirmed.

Fracture toughness of aluminum nitride bulk material has been studied in [52]. A K_{Ic} of 2.6 MPa/m$^{1/2}$ is reported with sample material being thin plates of few millimeters thickness. No studies on fracture toughness of aluminum nitride thin films deposited through contemporary thin film fabrication methods have been made

and thus it is equally interesting to conduct measurements, as the deposition methods and crystalline quality of thin films may induce a considerably different fracture toughness in these thin films.

Aluminum nitride is an interesting material for a variety of applications. Due to its anisotropic nature, the material properties of produced thin films vary greatly depending on the grain orientation in the structure and thus consideration is required when comparing results from films fabricated in different manners. The Young's modulus, residual stress, UTS and fracture toughness of aluminum nitride thin films are measured in this thesis and the results are presented in section 9.

3.1.2 Silicon

Silicon used in semiconductor technology often comes as wafers cut from a monocrystalline silicon ingot. The silicon wafer can be grown in different directions depending on which crystallographic orientation is preferred. The crystalline structure of silicon is face-centered diamond-cubic, which is visualized in figure 6.

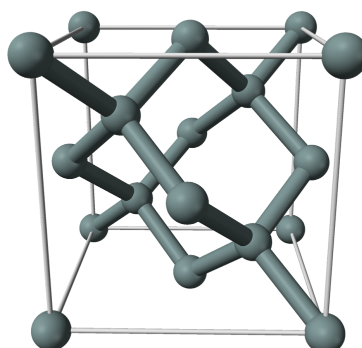

Figure 6: Face-centered diamond-cubic crystal structure of silicon. [53]

Most commonly wafers are grown in the [100] Miller index direction, but for use in aluminum nitride thin film growth, a surface structure with less lattice mismatch with AlN is usually required in order for the [002]-oriented growth to occur.

The silicon (111) plane surface has an atomic layout closer to the hexagonal layout of (001)-AlN. The lattice mismatch between the AlN 001-plane and Si-111-plane is only 19 %, whereas it would be 49 % between 100-Si and 001-AlN. [54] In these experiments, only (111)-silicon substrates are used in order to maintain good film quality and correlation of our experiments.

The substrates affect the growth of AlN films and thus cause changes in the defect distributions and residual stresses of these films through both lattice and CTE-mismatch related effects. Thus it is important to note the kind of substrate used when comparing results from different studies. It should as well be noted that in some measurement techniques (discussed in section 5), film is tested while still on the substrate, and thus the mechanical properties of the substrate should be well known.

3.2 Defect types and their formation

As previously discussed, the fracture of brittle materials is predominantly caused by stress concentration on defects in the material. In practice, materials always contain some defects that can originate from various sources in the fabrication process. There is a variety of different kinds of defects and the most relevant defect types and their origin are presented in this section, with their possible effects on the measurement results assessed.

Defects in crystalline materials can be classified into two categories: imperfections in the crystal lattice and three dimensional bulk defects. Crystal lattice imperfections include all distortions in the perfect crystal lattice and are categorized into three types: point, line and planar defects. Point defects are lattice distortions originating from a single lattice point, line defects are then originating from a linear dislocation in the material and plane defects are then planar discontinuities in the material, such as twin boundaries. Bulk three dimensional defects are then all defect types that distort the lattice to the extent that the interatomic bonds are almost completely severed, such as grain boundaries. In addition to these, extrinsic defects (for example scratches and etching damage) caused by processing and handling may as well significantly contribute to the mechanical response of these films, although the films with these defects are likely to alter the films response to such an extent that they show clearly outlying mechanical properties, such as clearly lower UTS than films with no such defects. [9, 55]

When discussing the mechanical properties of a material, the size and density of defects are of great influence. All of a material volumes mechanical properties, such as Young's modulus and UTS, follow from the interaction of single atoms in the material under stress. Small defects alter the aforementioned interaction for only a few atoms, whereas larger defects affect these interactions for billions of atoms. Thus a smaller defect has less effect by itself, although a large density of smaller defect types can yield a considerable effect. However, a population of larger defects is highly likely to have a much larger effect and thus dominate the response of the material to stress, especially in the case of UTS. For this reason, the defect types that are of interest in this thesis are the planar imperfections in crystal lattices and the three dimensional bulk defects as it is likely that linear and point defects yield little to no noticeable effect on the mechanical properties of the polycrystalline AlN thin films in this thesis. [9]

In this thesis, Young's modulus, residual stress, UTS and fracture toughness of AlN are measured. In addition to these, fatigue effects are assessed through cyclic loading. Defects should have no effect on measured fracture toughness as a defect of larger size is fabricated than what the material should contain. For Young's modulus, residual stress and UTS, a varying effect should be observable. The defect types and the way they affect the measurement of the quantities or the quantities themselves are discussed separately in the following text.

For Young's modulus, it has been shown that increasing amount of volume defects causes the measured effective Young's modulus to be smaller than in a case without defects. Equations are also presented that can be used to compare two measured

Young's moduli of differing film types to evaluate the difference in porosity or defect content of those film types. [56] These calculations only take into account the mechanical response caused by three dimensional bulk defects, which follows from the geometrical shape of these defects. The greatest lattice distortion related effect in the AlN thin films in this thesis is likely to arise from the grain boundaries in the polycrystalline films. It has been reported that grain boundaries themselves have a lower Young's modulus than the material in a crystalline lattice due to the amorphous nature of the lattice at grain boundaries, and thus an increasing proportion of grain boundary area in the material will result in a lower measured effective Young's modulus. A considerable decrease at 10-40 nm grain size has been noted, which is close to the grain size that the films in this thesis are likely to have. [57]

Residual stresses are formed in thin films during their deposition processes and vary greatly depending on the physics of the deposition process used. The relation between defects and residual stresses in the film is in that residual stresses are relaxed through formation of planar and line dislocations and three dimensional bulk defects during or after the deposition process. This is primarily the case when the residual stresses are tensile. Compressive residual stresses are commonly formed due to point defects (a process gas or an intended doping material fills some points in the crystal lattice). However, compressive stresses are not present in the films tested in this thesis (and they could not be tested with the bulge test in any case as is noted in section 5.7) and thus the residual stresses discussed in this thesis are purely tensile. As stated, the formation mechanisms and effects of residual stresses are various and are assessed in more detail in [58]. Their main effect considering measurements and results of residual stresses in this thesis lies in that residual stresses cause some formation of line, planar and three dimensional bulk defects in the material, with defect formation being more pronounced closer to the substrate-film interface [22] (due to substrate constrainment) and more intact crystalline lattice being present closer to the film surface with lower residual stresses (due to residual stress relaxation through dislocation formation).

In the case of UTS, the defect content of the material is naturally a decisive factor. As stated previously, brittle materials fracture when stress concentration at one point of the material exceeds the fracture toughness of the material. Defects cause stress concentration on the tips of the defects and thus dictate the stress at which a brittle material fractures. As stress concentration is the decisive factor, the size of individual defects is the most important aspect in how defects alter the UTS, accompanied by the distribution density of those defects. The main defect types that affect the UTS of a material are thus planar dislocations and three dimensional bulk defects. The largest defect type determines the measured UTS, as can be seen from equation (2.4).

In literature, it is noted that defect types in polycrystalline AlN films originate dominantly from the interface between the substrate and the thin film. The lattice mismatch of the interface creates lattice distortions, which then thread through the volume of the material as a thicker layer is grown, in a so called screw threading manner. [39, 58] The layer thickness where most defects are formed is in the range of 25 nm (as can be seen in figure 7), which is a significant part of the thickness

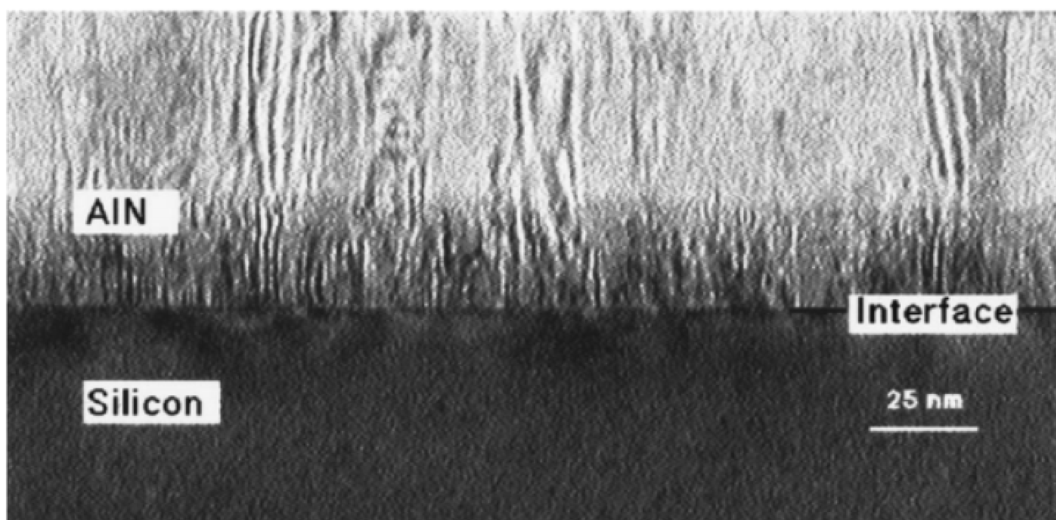

Figure 7: A TEM image of AlN deposited with plasma assisted gas source molecular epitaxy on 111-silicon with a highly defect populated layer of 25 nm thickness well visible at the interface. [22]

of the films studied in this thesis, and thus this transition layer is likely to have a considerable effect on the mechanical properties of these films. [22, 59]

4 Fabrication methods

Thin film deposition techniques can impose significant variation in the structures and residual stresses of the deposited thin films. The residual stresses and structural properties, such as grain size, defect density and crystal orientation, directly affect the mechanical properties of the material. Thus, it is important to evaluate and take into account the effect of the deposition technique on the measured material properties. This will be done in the section 4.1, where great emphasis is given on what kind of films the methods produce, while still giving a brief recap of the process itself and the process parameters involved.

In addition to the film deposition techniques, the other sample fabrication processes used in this thesis are presented, with the possible effects on film quality being assessed in section 4.2.

4.1 Deposition methods

The methods used in the deposition of aluminum nitride thin films in this thesis are explained in the following sections.

4.1.1 Atomic Layer Deposition

Atomic layer deposition (ALD) is a chemical vapour deposition technique that is based on the cycling of self-limiting gas-solid reactions. Two different gases (called precursors or in some cases reactants) are used in the process. First, one of the precursors is introduced in the deposition chamber (where a substrate is also placed). The precursor reacts with the substrate surface, which results in a thin layer of this precursor being deposited on the substrate surface. Then, the first precursor is purged from the chamber, after which the second precursor is introduced. The second precursor reacts with the first precursor that is deposited on the substrate surface, producing a thin film (also called a monolayer) of material that consists of the reaction product of these two precursors. Then the second precursor is purged from the chamber and the first precursor is again introduced in the chamber. This cycle is repeated until a film of preferred thickness is reached. [60] The reaction is visualized in figure 8.

ALD is based on cyclic irreversible and self-limiting reactions. This means that both precursors should be able to saturate the surface of the substrate, and that the deposited precursor no longer reacts with the surface once the surface is saturated. This leads to the fact that under purely ALD conditions (the reaction is perfectly saturating and irreversible) the only relevant parameters for production of films of different thicknesses are the amount of cycles and the thickness of a single monolayer produced during one ALD cycle. For this reason, growth rate of ALD is generally considered reasonably stable for parameter changes, for example the temperature dependence of material deposited per cycle is very weak in the common temperature ranges used for deposition (180 - 300 °C) (when for example common CVD processes have exponential temperature dependence). [60]

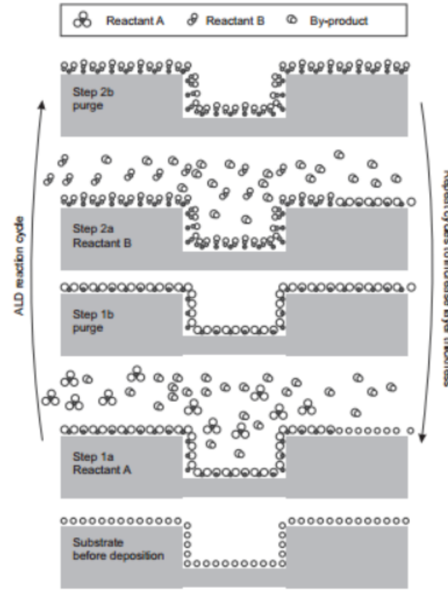

Figure 8: One ALD cycle illustrated. [60]

However, a number of non-idealities lead to the fact that some parameters still affect the actual structure of the produced thin film. A complete list of these possible imperfections in the process is given in [60] chapter A. The most relevant ones are the temperature dependency of both the film growth per cycle and the actual structure of the film that is produced, and the effect the substrate has on the deposited film.

In the case of AlN, an important question is the crystallinity of the material. General understanding is that ALD often produces AlN with varying crystalline structures. Often the produced films are amorphous or at least partially amorphous and crystal lattice orientations are mixed [61, 62], due to which they are not applicable for use in piezoelectric applications. However, there are other possible applications where this kind of film can be used [63].

ALD will be used to produce Al_2O_3-hard masks, the details of which will be presented in section 8.

4.1.2 Metalorganic vapour phase epitaxy

Metalorganic vapour phase epitaxy (MOVPE or also MOCVD) is a chemical vapour deposition technique where chemical reaction between a metalorganic compound and a reactant, usually a hydride, enables growth of a layer of a crystalline compound on a crystalline substrate. The reaction is based on pyrolysis (decomposition of the metalorganic at elevated temperature), which leaves the decomposed metal to bond with the substrate surface, which then results in a metal layer being deposited on the substrate. The metal atoms then react with the hydride compound, producing the desired crystalline material with the byproducts being vented out of the reaction chamber. [64, 65]

The main parameters in a MOVPE deposition process are the process temperature,

the reactant gas compositions and the crystalline structure of the substrate. Of some importance, although harder to characterize, are other process technology related parameters, such as venting of the reaction byproducts to prevent contamination.

The required process temperature depends on the pyrolysis temperature of the metalorganic compound, and naturally the temperature should be high enough for adequate pyrolysis to occur. The high temperature also increases the mobility of atoms in the gas, which helps them to find the most energy-efficient positions during deposition and thus allows for crystalline structures to form. Another effect of a high process temperature is that a possible CTE mismatch between the produced thin film and the substrate will generate residual stresses during cooling of the wafer. [64, 65]

The partial pressure and composition of the reactant gases can be altered as well, although it mainly effects the deposition rate and should be optimized so that there is enough reacting particles available for the deposition process to occur uniformly on the substrate surface. [64, 65]

Other parameters, such as substrate structure and reactant gas composition, alter the deposition rate of the process, and thus the manner in which the thickness of the deposited film is defined is through process time. As the deposition rate might vary due to small changes in process conditions, it is usually measured by testing the process with certain parameters for a certain duration, and then measuring the following film thickness. In more modern devices, *in situ* reflectance measurement provides the necessary thickness data. Deposition rate can then be used for approximating film thicknesses for another process run with the same parameters. [64, 65]

MOVPE is an epitaxial deposition method, which means that the deposited structure attempts to match the crystalline structure of the substrate surface. Large lattice mismatch does not allow for actual epitaxial growth, and thus the reaction could yield variable results in cases with large lattice mismatches. A reasonable lattice mismatch (such as between (111)-silicon and (002)-AlN) will enable the deposition process, but the mismatch may cause some stresses to form in the film and these stresses are relaxed by dislocations and mixed crystalline structure close to silicon surface [22]. In addition to this, the CTE mismatch between AlN and silicon may possibly cause significant residual stresses due to the high temperatures involved, and thus deposition of thicker MOVPE films could become increasingly difficult, when residual stresses surpass the UTS of the material.

MOVPE-produced films will be studied in this thesis and the process parameters are reported in section 8.

4.1.3 Sputter deposition

Sputter deposition is a deposition technique, which is based on the bombardment of a *target* with energetic particles. The bombardment detaches particles from the target, which then tend to deposit on any surface that they hit. The wafer that is to be coated is placed underneath this target and so it will be coated with particles detached from the target. The gas used to produce the bombarding ions is dependant on the target substance, and with aluminum, most often argon plasma is used. [66, 67]

In the case of this thesis where aluminum nitride coatings are produced, the process is called reactive sputtering, where the detached aluminum particles react with the nitrogen atoms found in the gas atmosphere in the reaction chamber. The formed aluminum nitride molecules then deposit on the wafer surface as described previously. [67]

Key parameters in a sputtering setup are the temperature of the wafer (as the wafer is warmed up by the ion bombardment, it is usually cooled), the kinetic energy of the sputtering ions, the composition of the used target, the base pressure of the deposition chamber and the partial pressures of the used gas environment. [67]

Crystalline films are of particular interest in this thesis and sputtering is capable of producing well ordered crystalline structures. Epitaxial growth of aluminum nitride has been reported when growing AlN on a Si(111) wafer. Sputtering is then done with an aluminum target under a mixed argon-nitrogen gas environment with base pressure being in the ultrahigh vacuum region. Temperatures in the range of 600 C° are used. The order of the crystalline structure is reported to be with AlN c-axis towards film surface. [66, 67]

Sputtered films will be studied in this thesis, and the fabrication and properties of these films will be discussed in 8 and 10.

4.2 Sample fabrication methods

4.2.1 Deep reactive ion etching

Reactive ion etching (RIE) is a dry etching process that employs a chemically reactive ion plasma to etch a material. The plasma is most often produced through radio frequency excitation of a gas and the reactive positive plasma ions are then directed on the material to be etched using an electric field. The reactive plasma ions are chosen according to the material that is to be etched. The etching is a combination of the chemical reaction of the plasma and the material under etching and the physical sputtering caused by the ion bombardment. The combination of physical and chemical etching enables anisotropic etching, which is required when high aspect ratio etches are desired. [68]

Deep reactive ion etching (DRIE) is a form of RIE where either cryogenic temperatures or passivation cycles are used to enable etching of high aspect ratio trenches. Cryogenic RIE relies on hindering of chemical etching when the material under etching is cooled to cryogenic (below -110 °C) temperatures. The etching is done under a gas atmosphere, where both passivating and reactive gases are present, for example with SF_6/O_2-chemistry. This results in passivation of trench sidewalls, while the sputtering effect removes the passivating layer from the bottom of the trench and enables anisotropic chemical etching. The clear benefit of cryogenic RIE is that it produces trenches with smooth sidewalls, which are useful when very narrow trenches are preferred. However, the cryogenic temperatures make use of hard masks difficult as they can be delaminated from the silicon surface under these extreme temperatures. [69]

DRIE using passivation cycles is called the Bosch process DRIE. In Bosch DRIE,

a reactive gas and a gas that produces a passivating layer are alternated. The passivating cycle produces a film of material that is resilient to etching and thus the whole surface of the material under etching is protected. In the reactive cycle, the ion sputtering effect causes faster removal of the passivation layer from the bottom of the trench, which causes higher etch rates in the vertical direction. However, the passivation layer is also etched away and some etching to the horizontal direction also occurs in the reactive cycle. This causes scalloping of the sidewalls of the trench. Nevertheless, the scalloped sidewalls do not pose much of a problem in applications, where trench widths are not in the nanometer scale. [69]

The Bosch process parameters include the gas pressures for both the passivating and reactive gases (and naturally the actual gases that are used), the platen power that determines the power of ion bombardment on the wafer, the RF power for producing the plasma, the cycle lengths and the wafer temperature. When etching silicon, the most common Bosch etch chemistry consists of SF_6 reactive gas and C_4F_8-O_2 passivation gas.

DRIE will be used in this thesis in order to release the thin film membranes for the bulge test experiment. The sample pieces are simultaneously detached from each other with lines that are etched away, removing the need for wafer dicing that could damage the fragile membranes. The process parameters used are described in 8.

4.2.2 Focused ion beam milling

A focused ion beam (FIB) is an instrument that can be used for both accurate imaging and micromachining of samples. It closely resembles a scanning electron microscope, with the main difference being that FIB uses ions instead of electrons as its beam. A FIB consists of an ion source (most usually gallium ions are used) and a set of lenses that are used to manipulate the beam. The ions are most commonly produced from liquid gallium that is under an intense electric field, which causes ionization and field emission of gallium ions, which then form the ion beam. The gallium ions are accelerated using an electric field and directed through the previously mentioned set of lenses and apertures. The lenses and the sample chamber of the FIB-device operate under a vacuum. [70]

FIB imaging employs scanning of a low energy ion beam across the target, which generates a secondary electron emission from the sample surface, which can then be detected. The ion beam always causes some ion implantation in the sample and material sputtering from the sample, depending on the beam current that is being used. For imaging purposes, the effect is limited due to the beam being directed on the surface of the material only for a shorter period of time, while for milling purposes, the beam is held in place for a longer time period in order to remove material with the sputtering effect. In this thesis, FIB is used to mill pre-cracks in some of the samples in order to measure the fracture toughness of the thin films. [70]

4.2.3 Lithography

Lithography will be used to pattern a hard mask layer on the backside of the silicon wafer. This hard mask prevents the etching of selected areas of the backside of the

mask, and thus enables the formation of chip dicing lines and free standing film cavities in the through wafer etch process.

In photolithography, photoresist is used to define patterns on to a surface of interest. The photoresist is spun on the surface-to-be-patterned, after which a strong UV light is applied on the photoresist through a mask. When developed in a special liquid, the exposed areas of the photoresist are stripped away, thus defining a pattern on the photoresist layer.

The patterned layer can then be used as a mask for wet etching processes. The wet etching is done using an acid that does not etch the photoresist, while etching the surface that is exposed from beneath the photoresist layer. Thus, the pattern on the photoresist can be transferred on to the surface of the substrate.

A variety of chemicals may be used in the lithography process, and thus it should be verified that no damage to the AlN thin film can occur during these steps.

5 Testing methods

The mechanical reliability of thin film materials can be assessed by placing a sample film under a known load, and then measuring the induced strain. When these two are known, the Young's modulus, residual stress and UTS of the film can be readily obtained. When a crack of a known size is induced, the fracture toughness of the material can as well be calculated when the stress-strain relation is known. Fatigue effects can then be assessed when the stress can be applied in a cyclic manner, preferably with low enough cycle times for testing to be feasible.

Although it may seem simple, the mechanical testing of thin film materials is difficult due to numerous reasons. Due to their size, thin films are so fragile that normal sample handling methods become unfeasible. The measurement of the stresses and strains will become increasingly difficult as the smaller the sample, the more accuracy is required in the measurement. In addition to these, with thin film samples, the film has to be somehow released from the substrate or then the film has to be tested with the substrate, which may produce additional difficulties. With these difficulties in mind, numerous differing testing setups and geometries are used in the assesment of the mechanical properties of materials. However, it is vital for calculation of accurate material properties that the stress and strain fields in the material are well modeled or measured.

The most used testing methods for characterization of the mechanical properties of thin films are presented in the following section. The field is reasonably vast, with different researchers often developing testing methods of their own. Thus only the most prominent testing methods are considered, with focus on those methods that could possibly be employed in this thesis. The basic concepts of these methods will be assessed with their weaknesses and strengths, with focus on the testing of aluminum nitride thin films.

5.1 Four point bending

A four point bending setup is a commonly used fracture testing setup for macro scale test specimens. It employs a simple beam of material, which is then bent using, for example, a hydraulic bending apparatus. The beam is supported from two points and the bending device applies force on two points of the beam, with the points being equally far from the supports of the beam, hence the name four point bending.

Such a testing setup is very easily built and different kinds of devices can be used to bend the beam. For this reason it is a commonly used method when testing macroscopic scale specimens. It is also well standardized by ASTM (for example ASTM standard D6272) in order to produce standardized and quantitative results in bulk specimens. By using Stoney's equation (14), it is also possible to test thin film structures using this method as the stress state of the thin film can be estimated when radius of curvature of the substrate is measured: [71]

$$\sigma_f = \frac{E_s h_s^2 \kappa}{6 h_f (1 - \nu_s)}, \tag{14}$$

where σ_f is the stress in the film, E_s is the Young's modulus of the substrate, h_s is the thickness of the substrate and κ is the radius of curvature of the substrate and naturally the film as well. h_f is the thickness of the film and ν_s is the Poisson's ratio of the substrate.

When attempting to measure thin film properties on a macroscopic test setup, the main concern is that, in order to obtain measurable quantities, the radius of sample curvature and the applied force need to be rather large compared to what the thin film can actually withstand. Thus, it requires high accuracy from the testing setup in order to be able to accurately determine the point of fracture for the thin film, and that the testing setups internal errors due to for example sample holder and actuator compliance and accuracy of where force is actually applied, need to be very small. This requires not only an accurate hydraulic test setup, but also an accurate mean for thin film fracture identification. Detection of acoustic waves produced by cracking and *in situ* SEM imaging have been used for this purpose [72]. The common hydraulic testing devices are usually too large for *in situ* SEM imaging, and thus the testing setup itself has to be scaled down in order to produce accurate results. This is where sample handling might become an issue, and hence more practical approaches are preferred, such as microcantilever specimens, which are discussed in more detail in section 5.5.

Four point bending can be easily used to measure Young's modulus, fracture strength and fracture toughness of bulk samples, whereas for thin films the case is a bit different. Young's modulus of a thin film cannot be measured as the effect of the thin film on the displacement-force curve compared to the substrate is negligible. Measurement of UTS should also be viable, however, for example in [72], only strain on the thin film at point of fracture is measured due to difficulties in determining the precise Young's modulus of the thin film. Measurement of fracture toughness is usually limited to delaminating cracks between the thin film and the substrate [73], and a special sandwiched sample structure is then used. This, however, can only be used to measure fracture toughness of an interface between the thin film and a substrate, which is only useful for this certain bilayer interface, and thus is not an intrinsic property of the thin film itself. [74]

Four point bending is thus not viable for thin film testing as it is, and more viable testing methods are discussed in the following sections.

5.2 Scratch testing

Scratch testing is done by driving a hard and narrow tip, for example a diamond indenter tip, across the coated surface while increasing the applied load towards the surface. The force at which cracking starts to occur and the force at which catastrophic failure (delamination) of the thin film occurs are measured. These values can be used in qualitative studies for comparison between different thin films, although the values do not represent any quantitative material parameter (UTS, fracture toughness) as they are. However, some effort has been made in order to convert these results into measures of fracture toughness. One of these methods is considered oversimplified, and the other too complex due to 3D finite element

modelling being required in order to model the tensile stresses in the thin film caused by the scratching. [12]

As force is applied towards the surface of the sample, substrate compliance and fracture properties also have to be considered when analyzing results [43]; the cracking and delamination can be caused by the substrate deforming rather than only the film.

Due to the complex stress fields caused by the indenter tip, it is close to impossible to obtain any quantitative material properties from scratch tests and thus it is mainly used as a quick qualitative comparison tool, and different nanoindentation based testing methods are used for quantitative studies, which are presented in the following sections.

5.3 Nano or microindentation

Nano- and microindentation are techniques that involve applying pressure on a thin film under testing with a very sharp and hard tip, called the indenter. The force at which the indenter is pushed into the thin film and the depth to which the indenter tip penetrates the film are recorded and used for calculation of material properties. There are multiple different tip materials and geometries that can be used, and when comparing results, one should take into account which tip has been used in the tests. The difference between nano- and microindentation lies mainly in the size of the indenter tip that is used, and consequently the accuracy of the testing device, and these names are often mixed. Thus the name nanoindentation is used henceforth.

Nanoindentation is a widely used technique for measurement of the Young's modulus and the so called indentation hardness (H) of the thin film. Hardness is a purely indentation related constant, which describes the materials ability to resist plastic deformation under indentation loads. However, it cannot be reliably related to actual yield stress or fracture toughness of the material, and thus it remains a comparative tool between indentation studies. Young's modulus can be readily extracted from the load-displacement curve produced by the device through either a simple method described in [75] or through a more elaborate, so called Oliver-Pharr, method [76]. Indentation hardness can be calculated using the equation:

$$H = \frac{P_{max}}{A}, \tag{15}$$

where H is the indentation hardness, P_{max} is the maximum applied pressure on the film and A is the contact area of the indenter tip, which can be calculated when depth of indentation and indenter tip geometry are known. As contact area is used in this equation, any discrepancies in its calculation will reduce the accuracy of the result. Pile-up of the material on the sides of the indent changes the contact area of the indentation tip and thus can cause variations in the results when materials with different plasticities are tested [75].

As nanoindentation of thin films requires pressure applied towards the substrate, the used substrate can naturally affect the measurement results. Any deformation in the substrate material will reduce the reliability of the measurement results, and

for this reason it is stated that indentations deeper than 10-20 % of the thin film thickness should not be used. It is also stated that residual stress states and substrate effects are generally difficult to account for in nanoindentation measurements. [75]

Effort has been made as well to find a way to reliably measure fracture toughness through nanoindentation. The main idea generally is to use for example a Vickers nanoindenter tip to produce cracking in the film and then measure the length of the produced cracks with a microscope. A large set of equations has been developed in order to link the crack lengths to the actual fracture toughness of the material. However, due to the complex 3D stress states during fracture with considerable material deformation around the cracks, the validity of this technique is under question and for this reason more rigorous techniques using nanoindentation for measurement of fracture toughness have been developed and are introduced in section 5.4. [77]

In conclusion, nanoindentation is an easy and quick method for determining the Young's modulus and hardness of a thin film when certain sample and measurement criteria are met. However, as the fracture properties of aluminum nitride thin films are of interest in this thesis, nanoindentation alone is not a valid method for all our testing needs and thus, in order to obtain information on the mechanical reliability of the thin films, special test geometries should be used in addition to pure nanoindentation, which are presented in the following sections.

5.4 Micropillar indentation

As stated in the previous section and shown in the figure 9, different kinds of test structures can be used in order to measure fracture properties of thin films with nanoindentation induced loads. These can be divided in two categories, micropillar and microcantilever indentation tests. Micropillar-type tests are presented in this section, whereas microcantilevers are discussed in section 5.5.

Micropillar indentation employs the indentation of a pillar-like structure ((d) in figure 9), which has been micromachined on the surface of the sample. The load at which this pillar fractures can be used to derive the fracture toughness of the material. The micromachining of the pillar is often done with a focused ion beam device (see section 4.2.2) and thus it is reasonably easy to produce this kind of test structures. It is reported that this kind of a test structure (when aspect ratio/film thickness criteria are met) relieves residual stresses in the film volume, and substrate effects should be minimal when sufficiently brittle materials are tested. [78]

Micropillar indentation seems to be a promising approach for measurement of fracture toughness instead of nanoindenting a non-prepared thin film. Reasonably accurate and reproducible results have been reported through use of micropillar indentation in [78]. The following equation is used to link the load at fracture to the fracture toughness of the sample material: [78]

$$K_c = \gamma \frac{P_c}{R^{3/2}}, \tag{16}$$

where P_c is the critical load at fracture, R is the radius of the pillar and γ is a

coefficient that depends on the ratio of hardness to Young's modulus of the material. Some values for γ are produced through cohesive zone finite element modelling in for materials quite similar to AlN [78]. K_c seems to be used instead of K_{Ic} as the stress state is possibly more complex than in a mode I loading condition, and thus the resulting value is a mixture of mode I, II and III fracture toughnesses.

Micropillar indentation has been considered a viable and simple technique for fracture toughness measurements [79]. It is relatively easy to produce a large amount of samples for testing and *in situ* imaging is only required for accurate placement of the indenter tip. However, it does have some limitations considering film thickness. The aspect ratio of the pillar (diameter/height) should be close to unity, and due to the damage induced by FIB milling, a 500 nm diameter is considered the minimum so that the area where fracture initiates is far enough from FIB milled edges of the pillar. [78] In this study, due to thickness limitations of MOVPE deposited AlN films, films with thicknesses of over 500 nm could possibly be too damaged due to excessive residual stresses to be tested. Even with a 1000 nm pillar diameter, it would be very difficult to place the nanoindenter tip accurately with the devices available here. Micropillar indentation was, however, considered a viable alternative when planning this study. However, due to the difficulties associated to its use, bulge testing was chosen for this study.

Micropillar indentation could be used to measure fracture toughness of a thin film, but for UTS measurements, a different test geometry should be used. The possible geometries are discussed in the following sections.

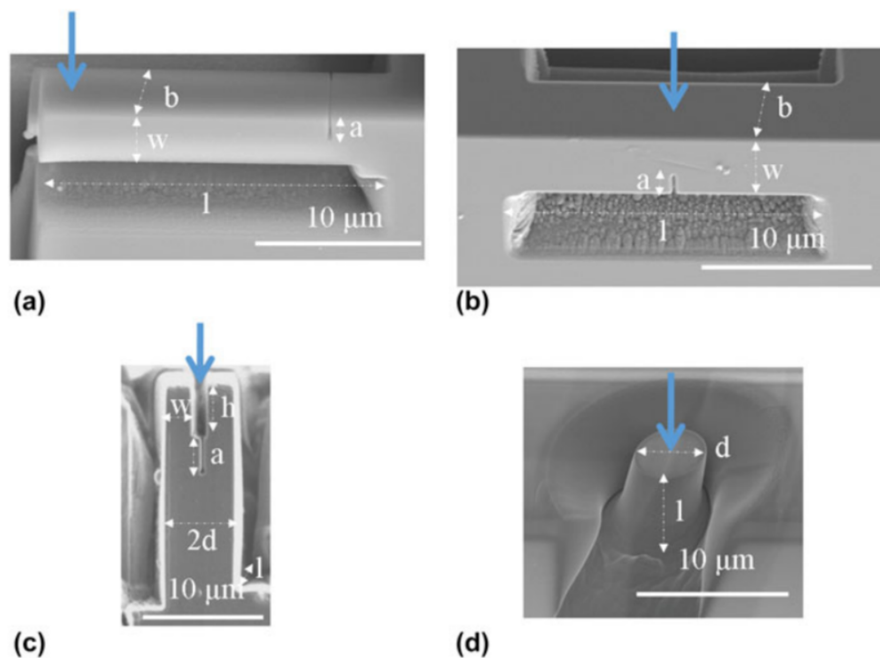

Figure 9: Different kinds of nanoindentation test structures. (a) is a common microcantilever, (b) is a clamped beam, (c) a double cantilever bending structure and (d) is the micropillar splitting sample. [79]

5.5 Microcantilever testing

In microcantilever testing, a micromachined test structure is loaded until its fracture. Loading is most commonly done using a nanoindenter or an atomic force microscope (AFM). The most common used structures are cantilevers attached to the substrate from one of their ends (single cantilever test), and beams that are attached to the substrate from both ends (clamped beam test). Depending on whether fracture toughness or UTS is the property under investigation, the cantilevers or beams can be made with or without a pre-crack of known length. For UTS measurements, a rounded notch is usually introduced in order to produce a controlled and modellable stress concentration zone. For fracture toughness measurements, the pre-cracks can be made using differing techniques as well, with most prevalent ones being micromachining a sharp notch with FIB milling or using an indenter to produce a crack on the beam. [79, 80]

As stated previously, it is possible to use a microcantilever setup to measure both fracture toughness and UTS using only slightly differing test structures. Some studies use Young's modulus that is calculated from the displacement-force curve of the measurement [81], while some use Young's moduli obtained via other measurement methods [79] and thus it is not clear whether it is a reliable mean of producing accurate values for Young's modulus.

In a single cantilever setup, it is assumed that residual stresses are reasonably well relaxed and thus do not affect the measurement, but for clamped beam experiment, the residual stress cannot be measured during testing and it has to be estimated using different measurement techniques. The clear benefits of this type of test is that it is rather easy to micromachine such test structures using a FIB device, and there is also a rather large amount of research that successfully employs microcantilever testing for these purposes.

For use in this thesis, there are a few weaknesses that discourage the use of microcantilever testing. First of all, the measurement structure is commonly in the range of tens of μm, and it is limited mainly by the accuracy of *in situ* imaging and nanoindenter movement resolution, which makes it difficult to test sample films with thicknesses under a micrometer. Testing has been done on samples with thicknesses down to half a μm [81], but this may be at the lower limits of what is feasible (and *in situ* imaging capabilities available for use in this study are very limited). The smaller the test structure, the more the accuracy of placement of the nanoindenter tip has effect on the test results due to varying stress states induced by misaligned indenter tip. Secondly, due to this size constraint, the test structure used in this thesis should most likely have a silicon beam with the thin film layer on top of it. This would make it very difficult to separate substrate effects from the actual mechanical properties of the thin film. These factors make accurate measurements of the thin films under study in this thesis difficult, and thus microcantilever tests were not chosen as the test method.

5.6 Microtensile film tests

The most common UTS measurement types in the macroscopic scale simply involve pulling a piece of material apart, while measuring the applied stress and induced strain. However, this becomes increasingly difficult when moving down to microscopic dimensions. Handling of microscopic sample structures requires *in situ* imaging and high resolution testing apparatuses. In the case of brittle structures, gripping of the sample in the loading apparatus may also prove impossible as it may damage the sample [82]. Thus it is more common to rely on different test structures to make handling of samples feasible. Microtensile tests are a vast family of differing testing setups that have been developed in order to reproduce a macroscopic tensile test in the microscopic scale. Thus the microtensile test types are discussed here in general, with some test types being presented as examples, such as those shown in figures 10 and 11.

All these tests involve applying a measurable uniaxial stress on the sample film. As stated previously, the greatest difficulties are first of all in fabrication and sample handling of these fragile and small samples. Clamping of samples in testing devices and setups is as well very difficult. A common way to resolve this issue is to use larger gripping handles, between which the film is suspended. Gripping can be done for example electrostatically or using an adhesive. Usually these test structures involve support structures, that can be severed prior to measurement in order to enable manual handling of the samples. Such techniques are demonstrated in [83], [84] and [85]. In [85], gripping pieces with holes are used, and in this case loading can be done using a hook structure. Samples are then loaded using either purpose built or modified loading devices with high resolution displacement control (examples of which can be found in [86] and [87]), with load cells for accurate load measurement. [88]

Another difficulty lies in accurate displacement sensing. Multiple techniques can be used, including AFM [84], interferometry [83] or high resolution *in situ* imaging with an optical microscope [86]. SEM and transmission electron microscopy (TEM) may also be used if the testing device can be made small enough [89].

The aforementioned techniques still involve manual handling of test samples and large testing devices that may produce error (for example accuracy of sample alignment [89]), when sub-μm films are tested. An approach that has been used is to use a compliant substrate material underneath the tested film. In this case, the substrate material and the thin film undergo the same strain under loading, and the data can be interpreted when the stress-strain behaviour of the substrate is known. This approach makes it easy to handle the film and makes testing possible with conventional equipment. [90, 11] However, the interface effects are not well known, and the results obtained may only be applicable for this certain bilayer structure [87].

One approach for minimizing the risk of these kinds of error is demonstrated in [89], where a testing device is designed that includes force sensing beams that can be used to calculate both the displacement and stress in the freestanding sample film. The whole test device is simultaneously manufactured and it is fitted inside a

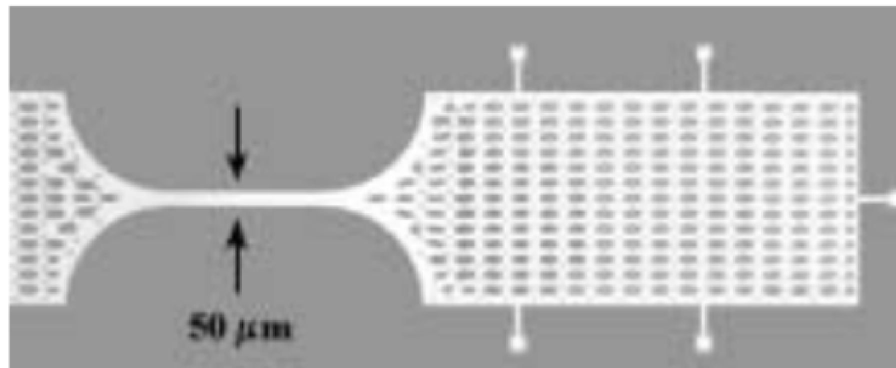

Figure 10: A microtensile testing structure, top down view. Load is applied using the grip handle on the right side of the picture. [84]

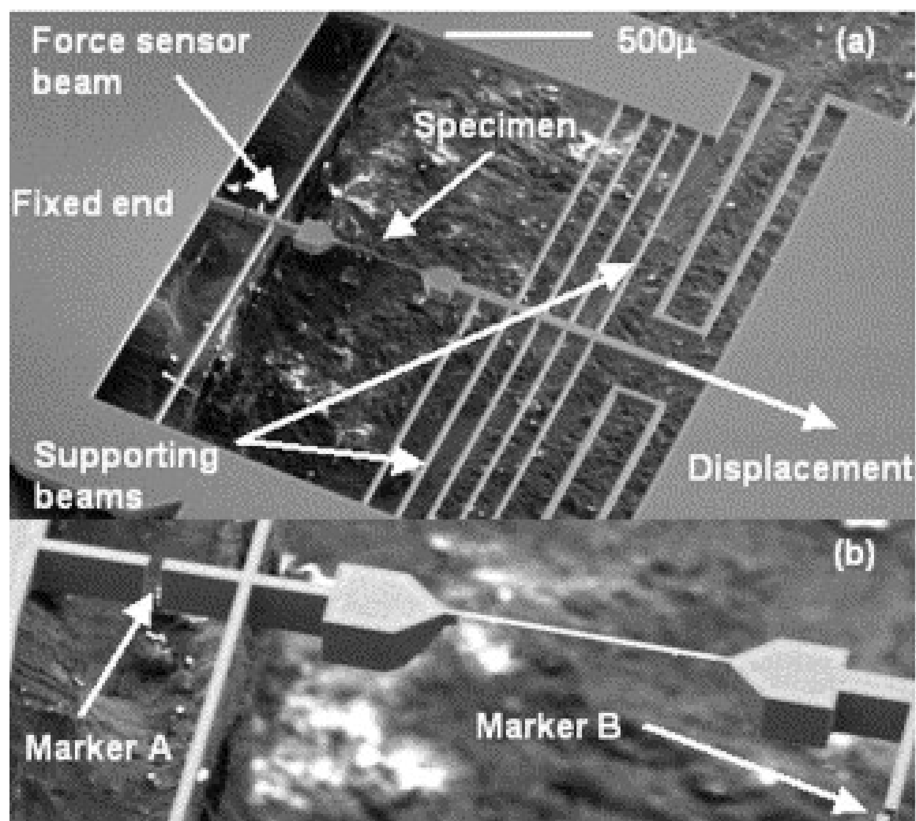

Figure 11: A miniature microtensile testing device. [91]

SEM or TEM device, which is then used to image the device for displacement data. An external loading device is used to load the sample structure. Sample films with thicknesses down to 30 nm have been tested [91]. Another device demonstrated in [92] has a thermal actuation mechanism built in.

The testing types listed here are only a fraction of all the possible configurations demonstrated in literature. However, for most test types, specially engineered testing devices and setups are required. Depending on the test type, there is also some

extent of accurate micromachining and microfabrication steps required. All the free standing test types are also inapplicable for films with compressive residual stresses due to film buckling after release. Depending on the test type, the tests may as well be very time exhaustive, which restricts the feasible sample set sizes. The strengths of these tests lie in the possibility of very accurate measurements and the purely uniaxial stress states that can be produced in the thin films (and thus the straightforward interpretation of results [11]). All of the microtensile test types produce a direct stress-strain relation, which can be easily used to obtain Young's moduli, yield strengths and UTSes of the thin films, with fracture toughness measurement being possibly viable using FIB milled pre-cracks. Nevertheless, such a testing geometry would not have been feasible for measurements in this thesis, and thus the bulge test was chosen, which is presented in the following section.

5.7 Bulge test

Bulge testing utilizes pressurization of a thin film in order to produce tension in this film. Most commonly it is realized through removal of substrate material from underneath a thin film, and then pressurizing this cavity in order to deflect the thin film. The thin film, that is left free standing, is called the bulge. [93]

This bulge can be pressurized either from the substrate cavity side (as is done in figure 12), or from the thin film side, depending primarily on the testing setup, with slightly differing outcomes depending on the chosen pressurization direction as is discussed in [94]. The cavity can be pressurized with various gases and fluids (for example water [95]), although testing is most often done with nitrogen or air [14], [96].

Bulge testing can be done on bulges of any shape as long as a pressurizable cavity is present. However, in order to be able to easily model the tensile stresses induced in the thin film, the chosen shape should either be rectangular or circular. The relation between the actual pressure and the tensile stress in the film is modeled through equations (18) and (17), which require either of these simple geometric cases for the stress distribution to be accurately modeled. [93] Round shape is more commonly used in UTS testing as a well defined model for the stress distribution in the film exists [96], whereas a rectangular shape is commonly used for fracture toughness measurements [95, 14].

Fracture toughness can be measured with a bulge testing setup, when a large aspect ratio (>4 [93]) rectangular film, that has a FIB-micromachined crack in its center, is used. The deflection versus pressure curve, or when the Young's modulus of the sample is well known, the pressure at fracture can be used to obtain stress on crack tip at fracture, which can then be used to calculate fracture toughness. This technique is also used in this study and it is more thoroughly explained in section see section 7.2.3.

Bulge tests can also be modified to accomodate loading with a nanoindenter, as is done in [96], where a shaft is left in the middle of the thin films. The shaft can then be loaded with a nanoindenter in order to produce deflection and fracture of the membrane.

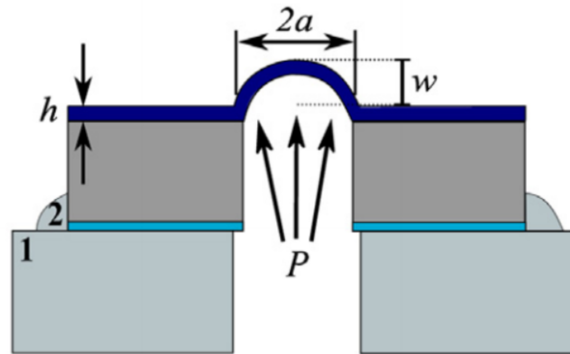

Figure 12: An illustration of the bulge test. [96]

The main advantages of bulge testing are its relative ease of sample production and the relatively simple testing setup. It is also easy to obtain a multitude of material parameters with the same testing setup (Young's modulus, residual stress, UTS and fracture toughness) and the samples and testing setup can be easily modified depending on the thin film material and thickness.

Its weaknesses lie in that a free standing film is tested and thus the substrate effects that may be in play in practical applications are not taken into account. However, multilayer structures can also be tested. It is also possible that the films are damaged during sample processing, which is difficult to identify with any characterization step. The testing setup is also very specific and thus the device needs to be built for this purpose only. If the membrane geometry has imperfections following a poor through-etch, stress concentrations that are not taken into account in the models may be induced, and the validity of the stresses calculated by the models are put under question as well.

Nevertheless, it is chosen as the testing method employed in this study and the Young's modulus, residual stresses, UTS and fracture toughness of AlN thin films are assessed using the bulge test. In addition, fatigue cycling is done as well using bulge pressurization cycles. The exact way the method is used is presented in section 7.2.1.

6 Characterization methods

In order to relate the measured mechanical properties to the films structural properties, a set of characterization measurements are required. The theoretical background of the characterization methods, that are used in this thesis, is presented in this section. The way these characterization methods are used in this study is then presented in section 7.3.

6.1 X-ray diffraction

X-ray diffraction (XRD) is a crystallographic characterization method that employs the diffraction of an X-ray beam from the crystal planes of a material under investigation. The diffraction patterns produced, when the sample is rotated, can be linked to different crystal planes, and thus the crystalline structure of the material can be studied. [97]

X-ray diffraction includes a wide range of techniques that employ the interaction between X-rays and crystal planes for the purpose of material structure research. These techniques include, for example, X-ray powder diffraction and Small angle x-ray scattering (SAXS). [97]

In this thesis, the primary interest is to obtain information on the crystalline quality of the AlN thin films and then evaluate if there is any correlation between the mechanical properties and the crystal structure. As the deposition methods used in this thesis can have differences in the crystalline quality of the produced films, it is important to characterize these crystalline properties so that possible variations in the mechanical properties of the films could be explained. [97]

The exact properties that are measured with an XRD scan vary depending on the direction of the scan rotation. The sample films can be turned in any preferred direction and angle. Nevertheless, the most common scans are of either type ω or ω-2θ. ω refers to the angle at which the X-rays hit the sample surface, and 2θ is the angle between the incoming beam and the detector. The exact physics of diffraction are best understood by thinking of the related geometry (visualized in figure 13) and the Bragg's law, which would be difficult to explain shortly here, and thus the differences between the scan types are rather briefly explained without going deeply into the actual physics behind the diffraction peaks, which are well explained in [39].

In an ω-scan the detector is held at a constant angle (usually the angle of some certain XRD peak of the material) and the angle of the incident beam is scanned. In a ω-2θ, both the incident beam and the detector are scanned at the same pace through a certain angle range (usually around an XRD peak as well). The differences between the studied properties between these two scan types are explained in the following text using the peaks of AlN as examples.

The intensity peak width of the 002-peak in ω-2θ XRD scan gives some insight into how the crystals are distributed and oriented in the films vertical axis (perpendicular to the film surface). When a single crystal is measured, the diffraction occurs at a singular angle value due to the 002-planes being at exactly the same distances from one another. When multiple crystals are present on the vertical axis of the thin

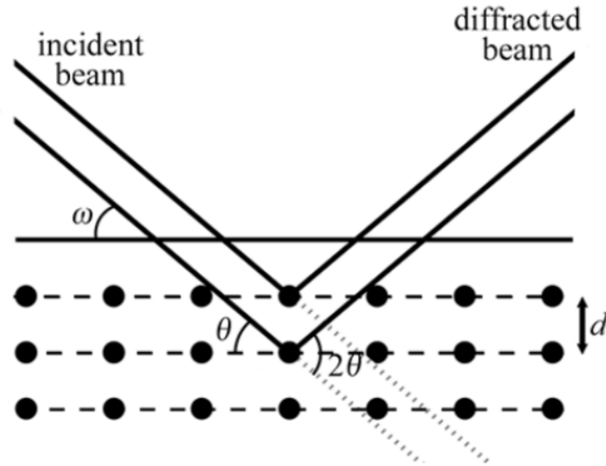

Figure 13: An illustration of X-ray diffraction. [36]

film, grain boundaries have a wider interplanar distance, and thus the diffraction can occur at a slightly differing angle. This can be seen in the XRD plot as widening of the intensity peak. The broadening of the peak is thus related to the crystallite size in this c-axis direction. In addition to this, residual stresses in the c-axis direction also distort the inter-002-plane distances even in single crystals, and this also yields a widening effect in the XRD curve, when a stress gradient is present. [98, 39]

Widening of a peak in an ω scan then shows if there is any variation in the c-axis orientation of the crystalline grains in the film. The variation is thus best explained by thinking of the geometry of the scan. Dislocations, column misalignment and wafer bending are the most prevalent causes of peak widening in these scans. [39]

These two XRD scan types can thus be used to study the crystallite size and orientation in the material. As the crystallite orientations differ primarily due to different defect related effects, the widening of the XRD peaks contains information of the crystalline qualities of the studied films. XRD scans will thus be used to study the crystalline quality of the sample films in this thesis.

6.2 Ellipsometry

Ellipsometry is a measurement technique that utilizes the polarization change between an incident and reflected beam when reflected from a thin film-substrate surface. The change of polarization can be compared to a mathematical model, and thus it can be linked to the material properties of the thin film, primarily its thickness and the complex refractive index. [99]

Ellipsometry will be used to measure the thicknesses of the sample films in this thesis for use in the mathematical models related to the bulge test experiments.

6.3 Scanning electron microscopy

Due to the high sensitivity of equations (18) and (17) to bulge diameter, the accurate diameters of the bulges should be obtained. Either scanning electron microscopy or

optical microscopy can be used to measure the bulge diameters.

SEM is based on the use of an electron beam that causes excitation of atoms in the material, which then emit secondary electrons. These secondary electrons can be detected and an image can be compiled when the electron beam is scanned through the material area. Imaging resolutions of up to 1 nm can be obtained with a SEM. Due to the great resolution, SEM can be used to image very small features. SEM devices usually require a vacuum in order to operate and thus the use of a SEM device may be time consuming. Thus in this thesis, SEM will be used to characterize the quality of the through wafer etching result and simultaneously the diameters that are measured with optical microscopy will be verified. [100]

7 Design of experiments

In this section, the research methods used are presented in detail. The experimental question is presented in section 7.1, while the section 7.2 discusses the bulge test experiments in detail. The characterization measurements that are done are presented in section 7.3. The section 7.4 explains the statistical nature of the UTS measurements and the methods that will be used in order to analyze the results.

7.1 Experimental question

The experimental question of this thesis is: What is the mechanical reliability of aluminum nitride thin films? In order to answer this question, the relevant mechanical properties of aluminum nitride thin films are measured, and once the properties are known, the mechanical reliability of the thin films can be evaluated.

Experiments are made in order to define what are the Young's moduli, residual stresses and ultimate tensile strengths of aluminum nitride thin films deposited via MOVPE (W7M100BX, the sample codes are introduced in section 8.1, and they are used in this section already for clarity) and sputtering (W1S50, W2S50, W4S200 and W5S200R). It will also be studied how these properties change in films of different thicknesses, as these experiments are done on sputtered films of two thicknesses (W1S50/W2S50 and W4S200), in order to enable use of the measurement results in evaluation of mechanical reliability of aluminum nitride thin films of differing thicknesses. Fracture toughness of these films will as well be measured with samples fabricated through sputter deposition (W5S200R). In addition to these, an experiment is made with the sputtered films (W4S200fat) in order to study whether fatigue has any effect on the mechanical properties of these thin films.

The method of choice for these measurements is the pressurized bulge test (see section 5.7), which can be used to measure all of the aforementioned properties. The details of the experimental procedure will be explained in the next section.

7.2 Experimental procedure

The experimental part of this thesis is divided into three distinct test types. The method of choice for all of the tests is the bulge test and the actual testing schemes are further described in the three following sections.

First testing scheme comprises of UTS, Young's modulus and residual stress measurements of the different sample types (all sample types except W5S200R). This scheme is presented in see section 7.2.1.

The second scheme comprises of fatigue cycling of a set of samples (W4S200fat), after which the UTS, Young's modulus and residual stress measurements described in section 7.2.1 are done for these samples. The scheme is presented in section 7.2.2.

The third scheme consists of the fracture toughness measurements of the rectangular bulge samples (W5S200R) prepared for this specific testing scheme. This scheme is presented in section 7.2.3.

7.2.1 Bulge test for UTS, Young's modulus and residual stress

The basic concepts of bulge testing are described in the section 5.7. This section further presents the theory of bulge tests, after which the scaling and planning of the UTS experiments will be presented. The experimental procedure realized in this thesis will then be reported.

Bulge test has been used in a study conducted in a research group in Aalto University [96]. In this study, fracture strength of Al_2O_3 thin films deposited via ALD was determined. Much of the testing procedures employed in the study are used as a basis for the testing procedure used in this study and the same testing equipment is as well used, although some changes are required to account for the material change and for the fracture toughness and fatigue experiments.

Bulge testing is based on loading a membrane of material with applied pressure. The pressure causes a deflection of the film and the displacement of the center of the film follows the relation described by the following equation:

$$P(w) = c_1 \frac{h\sigma_0}{a^2} w + c_2 \frac{hE}{a^4(1-v)} w^3, \tag{17}$$

where $P(w)$ is applied pressure, σ_0 is the residual stress in the film, E is the Young's modulus of the film, a is the half-width of the membrane (or radius), w is the displacement of the bulge center, ν is the Poisson's ratio of the film and h is the displacement of the bulge center when pressurized [93]. c_1 and c_2 are coefficients for differing geometries and they are explained in more detail in [93], and the constants used in this thesis are discussed in more detail in the following text.

Thus when the thickness, diameter and Poisson's ratio of the film are known and the pressure and the displacement of the center of the membrane is measured at multiple pressure values, the data can be fitted using equation (17) in order to calculate the Young's modulus and residual stress in the film.

The equation holds under a few assumptions. First, the film should be very thin compared to the deflections that are induced. In such a case, the effect of bending on the strain can be neglected. The effect of film stiffness on the stress state at film edges is also assumed negligible when large deflections are measured. It is as well pointed out, that the stress field in the film is not equal-biaxial, but rather transfers from equal-biaxial in the center of the film to plane strain at the edges of the film. In addition, it is stated, that due to the weak relation to residual stress of the parameter c_2, the model may become inaccurate at residual stresses above 0.5 GPa. [93]

Coming back to the values of the c-parameters, numerous different values are used in literature with some values listed in [96] for circular membranes. In a more recent, yet unpublished, work, the fit between experimental data and displacement-pressure curves predicted by this model with differing c_1 and c_2 parameters is evaluated and the values c_1=4 and c_2=2.67/(1.026+0.233·ν) represent the experimental situation the best. These values are obtained through FEM modeling in [101] and these values are used for circular membranes in this thesis.

In addition to the equation (17) that could as well be used to calculate the stress at the center of the bulge, an equation has been derived that directly relates the applied

pressure to the stress state at the center of a circular bulge. Thus, measurement of deflection becomes unnecessary and equipment with no displacement measurement capability can be used, which makes testing much faster. The equation is derived in its simple form in [102], where the effect of residual stresses is neglected. In a more recent, although yet unpublished work [103], an equation, which takes into account the effect of residual stresses, is derived in a similar manner as is done in [93] for rectangular membranes, and it is the following:

$$\sigma_{UTS}^3 - \sigma_0 \sigma_{UTS}^2 - \frac{1}{24} \frac{E P_u^2 a^2}{(1-\nu) h^2} = 0, \tag{18}$$

where σ_{UTS} is the ultimate tensile stress, σ_0 is the residual tensile stress in the film, E is the Young's modulus of the film, P_u is the pressure at fracture, a the half-width of the membrane (or radius), ν is the Poisson's ratio and h is the thickness of the membrane.

In the study [103], the effect of residual stresses on the calculated UTS results is assessed and its effect is seen to increase at higher residual tensile stresses. Thus, the equation (18) is used in this thesis and the general solution to a cubic equation is used to solve the equation for UTS, with residual stress and Young's modulus values acquired from the separate measurements used.

The equation (18) is an approximation that models the stress field in the center of a circular film and assumes biaxial loading (which should be a valid assumption in the center of the film) and a hemispherical cap shape of the bulge center when pressurized (which is valid at low deflections, and becomes increasingly inaccurate at higher deflections, where higher order geometrical terms have an effect). [102] It should as well be noted that the stress state is not uniform in the whole film volume as can be seen from figure 14. The equation thus only represents the stress state at the central region of the bulge, which is the maximum stress the bulged film experiences during pressurization and thus can be used in UTS measurements. It should, however, be noted when comparing results from bulge tests to other experiments or to an application of choice. The concept of effective volume will be discussed in section 7.4, and the effect of the stress gradient in the film is further evaluated in section 10.3.

With these two equations (17) and (18), the Young's modulus, residual stress and UTS of the bulge samples can be calculated. For Young's modulus measurements, displacement measurement is required and a bulge testing setup at Helsinki University is used in order to produce displacement-pressure data. The setup is described in section 7.2.5. For UTS measurements, as displacement measurement is not required, a testing device found at Micronova can be used. This device is presented in section 7.2.4.

The difficulty in planning of these tests was that the UTS of AlN thin films has not been studied, and from prior knowledge it could only be estimated to be in the range of 345 MPa (flexural strength of bulk AlN) to around 5 GPa (if the same approximately tenfold increase is observed as for Al_2O_3 in [96]). The devices used here have differing pressure ranges with 0–2.2 bar with Helsinki University and 0–3.75 bar with Micronova device. As all UTS tests are done with the Micronova

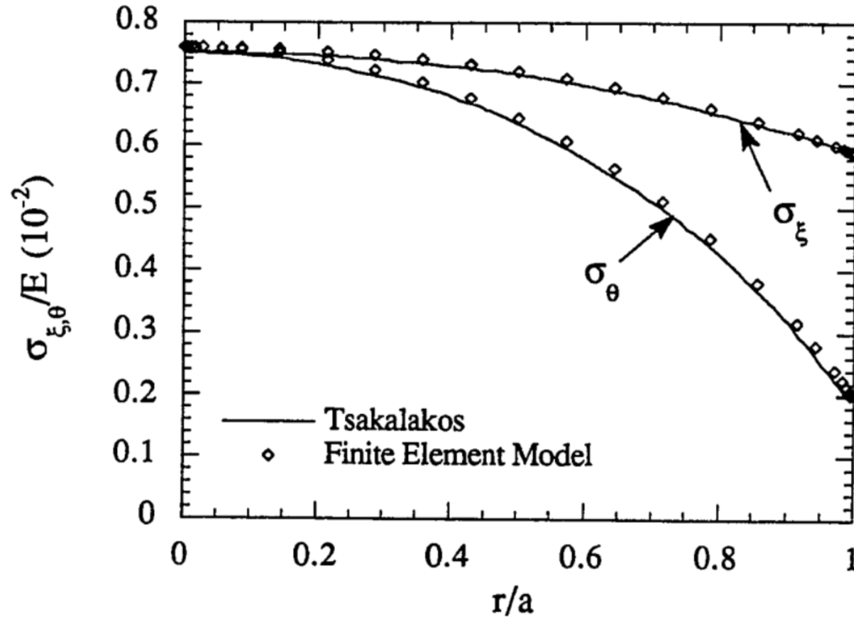

Figure 14: Stress distribution in a bulge film obtained via finite element modelling [104]

device, this fracture of the membranes should be matched to its pressure range, and as stated in section 7.2.4, the most accurate measurement range would be in the range of 1–2 bars. Another difficulty was to match all the tested thicknesses in this range with the same bulge diameter, in order to produce as comparable data as possible. Following the (18), a bulge diameter of 900 μm was chosen, although as can be seen from section 8 and table 9.1.2, the actual diameters were closer to 940 μm due to overetching. All the measurements could be done with samples of this diameter, except for fracture toughness, where a different sample type was used.

The Young's modulus and residual stress measurements are less affected by probabilistic effects and thus a sample set of 3 samples per film type was deemed adequate for reasonably accurate results, as the use of the the Helsinki University equipment was limited. The UTS measurements have a pronounced probabilistic nature as described in sections 2.6 and 2.12.2, and thus a sample set of 25–30 samples per film type is required in order to produce the Weibull plots used in UTS measurements, which are introduced in section 7.4 [55]. A sample set of 30 samples per sample type is thus tested with the Micronova equipment in order to produce reliable results for the UTS of the different film types. These experiments are done with all three different film types studied in this thesis.

Bulge testing can be done by applying pressure on either side of the film and due to delamination and bulge edge stiffness related effects, the results may vary as is shown in [94]. The equipment at Helsinki University can only be used when the cavity side of the film is pressurized and thus all the testing is done with this direction of pressurization. A pressure ramp rate of 10 mbar/s is used for all UTS measurements. Measurements at Helsinki University require manual setting of the

pressure using a hand valve and thus the pressure steps depend on the user, and are commonly in the range of a minimum 50 mbar per step. Thus, fewer measurement points could be achieved with thinner samples that fractured earlier in the pressure range. The curve fitting produced more unreliable results when fewer measurement points are available, but for all measurements at least 4 measurement points were achieved and thus the fits should have reasonable accuracy even in these cases.

In this section, the experimental details on Young's modulus, residual stress and UTS measurements have been given. In the following two sections, the fatigue testing scheme and the fracture toughness measurements are presented.

7.2.2 Fatigue testing

In order to produce fatigue damage, the films are placed under cyclic pressurization. Fatigue cycling tests with bulge testing equipment have been demonstrated in [105] and a similar approach was chosen in this study. As ceramics are generally found to be very resilient to fatigue damage, cycle amounts in the range of hundreds of thousands of cycles are generally used [25, 21]. However, fatigue cycling with the bulge testing equipment used at Micronova takes approximately 50 minutes for 10000 cycles, and thus in the scope of this thesis, the cycle amounts reported in literature are not applicable. The equipment is also incapable of recording the cycle at which bulge fracture occurs, and thus a conventional cycles-to-failure-type of test was unfeasible.

In [25], fatigue changes in a ceramic material are reported when cyclic stress is between 60-80 % of the UTS of the material. In these studies, the cycles are run until failure of the specimen, and thus it may be that fatigue related changes can already be observed with less cycles. Thus, an experiment was chosen where 10000 cycles of 700 mbar pressure are run on 24 samples from one sample film type (W4S200fat), after which 20 of the samples are pressurized until fracture with the Micronova device in order to obtain the UTS of these fatigue-cycled samples, and the Young's moduli and residual stresses of 4 samples are measured with the Helsinki University bulge tester. These values are then compared to those of the non-fatigue cycled samples of the same film type (W4S200) in order to quantify any effects that the fatigue cycling may have induced. Although it is stated in [55] that 25–30 samples are generally required in order to produce reliable results with Weibull analysis, a sample set of 20 samples was thought adequate. This should, however, be noted when interpreting the obtained results.

700 mbar pressure yields a 1.28 GPa stress on the film, which is approximately 82 % of the calculated average UTS of 1.502 GPa (see section 9.4) and thus the stress should be large enough for fatigue effects to occur, while being small enough that none of the fatigue cycled samples fracture during cycling.

The almost instantaneous pressurization option of the Micronova tester is used with a test time of 200 ms, which results in an approximate pressure cycle duration of 0.3 ms.

7.2.3 Bulge test for fracture toughness

Bulge testing has been modified for use in fracture toughness testing in [14] and [106]. A pre-crack of a known length is introduced into a rectangular membrane sample through focused ion beam milling, as is visualized in figure 16. The stress at which this crack extends is then used to calculate the mode I fracture toughness of the thin film specimen through the methods explained in the following text. Rectangular membranes (see figure 15) are used due to the fact that when aspect ratios (length/width) higher than 4 are used, the film is under plane strain conditions with the strain in length direction being zero. This results in a more well defined lateral stress in the width-direction of the membrane, and thus allows for accurate measurement of the induced stress concentration on the tips of a crack situated in the center of the bulge, when the crack is oriented perpendicular to the lateral stress. [14]

The lateral stress at the center of a rectangular bulge with an aspect ratio higher than 4 is given by the following equation:

$$\sigma_{xx} = \frac{p(a^2 + h^2)}{2th}, \tag{19}$$

where p is the applied pressure, h is the membrane deflection, t is the film thickness and a the half-width of the membrane [14].

The aforementioned equation requires measurement of bulge displacement, which can be done using the the Helsinki University equipment. However, the setup lacks the capability of accurate displacement-pressure measurement at point of fracture, which is an issue, as this information would be needed for the calculation of fracture toughness. In section 7.2.1, a way to calculate stresses in the film with only pressure data is given in the equation (18). A similar equation can be derived for rectangular membranes (with an aspect ratio higher than 4) through use of equation (19) instead of the Beams model for a hemispherical cap, and the following equation can be found: [93]

$$\sigma_{UTS}^3 - \sigma_0 \sigma_{UTS}^2 - \frac{1}{6(1+v)} \frac{E P_u^2 a^2}{(1-\nu)h^2} = 0, \tag{20}$$

This equation can be used to calculate the ultimate tensile stress at which the precrack in the tested bulge film extends.

Another way is to extrapolate the films pressure-displacement data to the pressure at which fracture occurs using the equation (17), and then calculate the stress using the extrapolated displacement value and Young's modulus and residual stress values given by the equation. For use in rectangular films, the c_1 and c_2 constants are given in [93] and are 2 and $\frac{8}{6(1+v)}$, respectively. The equation takes the following form when solved for displacement w, for use in extrapolating displacement for a known pressure:

$$\frac{8hE}{6(1-\nu^2)a^4} w^3 + \frac{2h\sigma_0}{a^2} w - P_{frac} = 0, \tag{21}$$

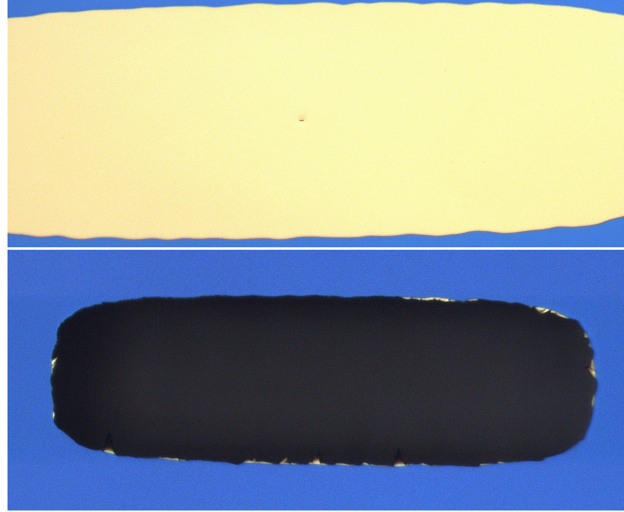

Figure 15: (Above) An image of a sample 280x860 μm rectangular bulge taken with optical microscopy with the 5 μm crack visible in the center of the membrane. (Below) A burst rectangular membrane sample, with slight curvature due to overetching visible.

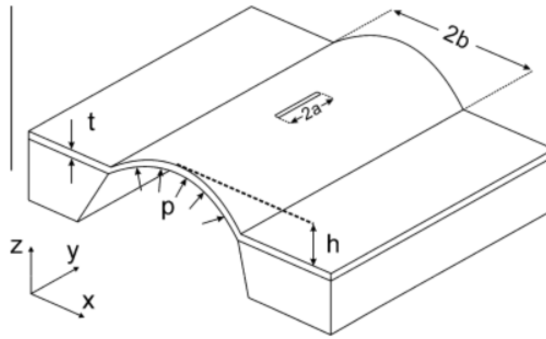

Figure 16: Rectangular membrane type with a FIB milled pre-crack along the center line used in fracture toughness measurements. [14]

Young's modulus and residual stress are acquired through the same method as is done in section 7.2.1, fitting the displacement-pressure data with equation (17). P_{frac} is the pressure at fracture. The displacement extrapolated using this equation is then used in equation (19) to calculate stress at fracture. Both the above mentioned methods will be used in order to verify the stress state at the center of the bulge, and if similar values are obtained, the validity of the equations (17) and (18) for modeling of stresses in the films will as well be verified.

Through the use of the aforementioned methods, the stress at which the pre-crack begins to propagate can be calculated through both use of displacement data and without. This stress and the known length of the FIB milled pre-crack can then be used in the following equation to calculate fracture toughness of the thin film specimen:

$$K_{Ic} = \sigma_c \sqrt{\pi a} Y \left(\frac{a}{W} \right), \tag{22}$$

where σ_c is the stress at fracture propagation and a is the half-width of the pre-crack. (a/W) is a geometrical constant with the value of 1 for our testing geometry [14].

With the relevant equations being known, the rectangles dimensions should be established. As a crack of any preferred length can be introduced, this setup is not as sensitive to the chosen diameter and the pressure at fracture can be chosen with the FIB milled pre-crack length. However, the bulge should have at least an aspect ratio of 4 in order to produce the plane strain conditions in the center of the film, and a smaller membrane is obviously more robust and easier to handle during fabrication. Thus a width of 200 μm and length of 800 μm was chosen, with the FIB milled pre-crack being 5 μm in length.

A more limited sample set of 8 samples from W5S200-wafer was tested in order to produce a reasonably accurate estimate for the fracture toughness of AlN thin films, and prove the experimental concept with the equipment available for this thesis. The accuracy and relevance of our measurement will be discussed in section 10.6.4.

FIB produced pre-cracks are deemed sharp enough to act in a similar manner as actual cracks and thus only damage caused by FIB ion implantation can be considered the drawback of this method, when proper through-thickness FIB milling can be achieved. [79]

7.2.4 Bulge tester at Micronova

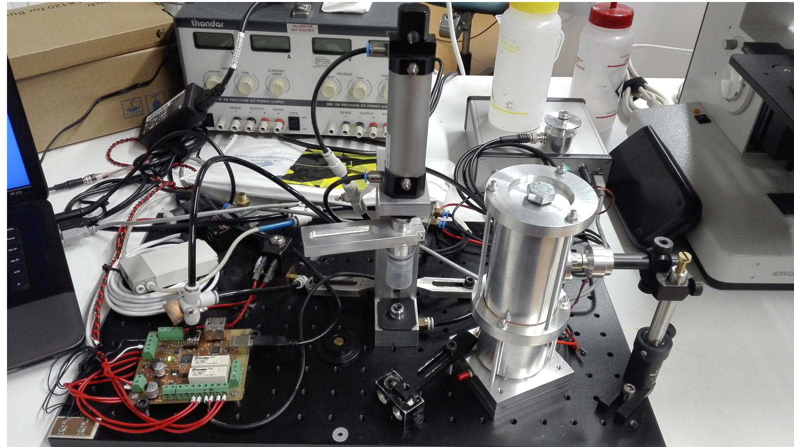

Figure 17: The UTS bulge testing device at Micronova.

The testing device at Micronova is shown in figure 17. It uses pressurized air from a high pressure line and is capable of applying pressures of 0–3.75 bars at constant ramp rates of 10 mbar/s to up to an almost instantaneous pressurization. Pressurization is controlled with an Arduino based feedback system and the device detects rapid changes in the cavity pressure, which is used to determine the point at which the bulge fractures.

The apparent resolution of the device is 1 mbar, although it is very likely that the realistic accuracy of the device is closer to 10 mbar. This resolution should be adequate, as the pressures at bulge fracture are in the range of hundreds of millibars.

The device can also be used for high speed pressure cycling with cycle speeds of up to 10 Hz being possible depending on the desired cycling pressure, with higher pressures requiring a longer cycle time.

An important parameter in the UTS testing is the ramp speed at which pressure is applied on the sample. As discussed in section 2.7, there may be some anelastic properties that affect the UTS measurement results of the films, if high strain rates are applied, and in order to minimize the effect of strain rate, a low ramp rate of 10 mbar/s is used in the UTS experiments. This translates to a strain rate in the range of $3.36 \cdot 10^{-5} s^{-1}$ (calculated with the average UTS and pressure at fracture of W4S200 samples presented in section 9.4).

The samples are tested film side down, as the device pumps the overpressure on the top side of the testing chamber, and when the film side is down, the situation is the same as with the equipment at Helsinki University and more comparable results can be obtained.

This device is used for all UTS measurements, the fatigue cycling of samples, and the fracture toughness measurements (once effective Young's moduli are acquired through use of the Helsinki University testing equipment).

7.2.5 Bulge tester with scanning white light interferometry at Helsinki University

The testing device at Helsinki University is slightly different to the one at Micronova. The sample is attached to a polydimethylsiloxane (PDMS) holder, which is then attached on a removable pressurization rig. The rig has a pressure line attached, that is then attached to an argon gas bottle. The pressure line is controlled with a hand valve from the argon bottle and the pressure in the line is measured with an external pressure gauge.

The rig is placed into a custom built scanning white light interferometer (SWLI), which consists of a halogen lamp (white light source), a Mirau type interference objective, a high speed black and white camera and a piezo scanner which moves the camera in order to scan the deflection range. The camera takes pictures at certain movement intervals, and the computer software uses these images to calculate the deflection of the film.

The major difference between the device at Micronova and the one at Helsinki University measurement-wise is, that the pressure is adjusted with a hand-valve and thus the steps at which pressure can be increased are determined by the user. The device does not register bulge fracture automatically, and thus it is difficult to obtain accurate pressure at fracture. If fracture occurs, only the deflection at the last pressure step can be obtained, and depending on the accuracy of the user, pressure increments of down to 20 mbar can be reached. However, steps of this size will lead to greatly increased testing time and thus larger steps are preferred in most Young's modulus testing as films can withstand pressures in the range of 1.5–2 bar. Due to

the manual nature of the measurement, any fracture results should be assessed with some precaution, while the pressure-deflection data is highly reliable as it is taken at stable pressure settings.

This device is used for all Young's modulus and residual stress measurements.

7.3 Characterization

In this section, the characterization methods used in the experiments are presented.

7.3.1 X-ray diffraction

As described in section 6.1, XRD measurements can be used to evaluate the crystalline quality of a material. Thus, XRD analysis will be conducted so that at least qualitative comparison between the film types can be made.

The Panalytical X'Pert XRD device used in this thesis can be used in both high resolution mode (HRXRD), where intensity distribution at a small change of angle can be accurately determined and the diffraction from a single crystalline orientation can be precisely studied, and in the so called powder diffraction mode (PXRD), which is basically a wider angular resolution option. PXRD was chosen for use in this thesis.

The methods of choice are the comparison of AlN 002-peaks in both ω and ω-2θ-scans. As explained in section 6.1, by comparing the 002-peaks of ω-scans of the films, insight into how widely the c-axes of the crystals in the film vary should be acquired. The widening of the 002-peak in the ω-2θ-scan is then caused by the variation of the inter-lattice-planar distances (variation of the c-lattice constant) in the film crystals, which is then caused by either residual stresses or grain boundaries in the c-axis direction of the film.

As the thicknesses and crystalline quality of the films studied in this thesis vary, the intensities produced by the diffraction vary as well. The intensity distributions that are measured with the XRD are often very noisy as can be seen from the figure 23. Thus a simple first order gaussian fit is done on all the measurements in order to make the measured data more comparable.

It is difficult to make any quantitative analysis based on the XRD characterization made in this study, as very accurate measurements and intricate mathematical modeling are often required. However, as a similar test setup is employed on all sample film types, it is easy to make qualitative comparison between the films based on the shape of the diffraction peaks, most notably their full width at half maximum (FWHM). The results and the comparative analysis are presented in sections 9.1.4 and 10.1, respectively.

7.3.2 Ellipsometry

The Plasmos ellipsometer in used in this study is a very simple measurement device. Initial guess value for the thickness of the film is given to the device and then a comparison to a mathematical model is automatically done by the device. It uses the aforementioned initial guess values to find the correct results, and thus the given guess values should be reasonably close to the measurement result. The possible alternative solution for thickness is, however, given by the software and it tends to be significantly larger than the thicknesses measured in this thesis and thus the actual solutions are very reliable (for example for a 220 nm thin film the next possible results would be ±175 nm apart). The ellipsometer is used to measure the thicknesses of all

the film types studied in this thesis, and the measured thicknesses are found in the table 4.

7.4 Statistical analysis

Weibull analysis is commonly used, when discussing failure of a device or material. As described in the section 2.12.2, the failure of brittle materials is predominantly caused by stress concentrations on defects and discontinuities. The Weibull distribution describes the probability of failure when a certain volume or area of material is under a certain stress loading:

$$P_f = 1 - \exp\left[-\int_V \left(\frac{\sigma}{\sigma_0}\right)^m dV\right], \tag{23}$$

where P_f is the probability of failure, V is the volume (area integral can be used as well, if surface defects are the dominant cause of fracture as explained later), σ is the stress at fracture, σ_0 is the so called critical stress factor (also known as the Weibull scale factor), where the probability of failure is 63 % and m is the Weibull shape parameter, that describes the slope of the Weibull fit. In this thesis, the Weibull scale factor is used as a measure of UTS instead of the average UTS, which would represent the stress at which probability of failure is 50 %. [55, 9]

When a fixed testing geometry is used, the integral yields the following equation: [55]

$$P_f = 1 - \exp\left(\frac{\sigma}{\sigma_\theta}\right)^m, \tag{24}$$

where σ_θ is the characteristic strength that is dependant of the sample volume according to the following equation: [55]

$$\sigma_\theta = \sigma_0 V_{eff}^{-1/m}, \tag{25}$$

where V_{eff} is the effective volume under stress in the sample (effective area could also be used), and σ_0 is the UTS of that volume. The effective volume is defined as: [55]

$$V_{eff} = \int_V \left(\frac{\sigma}{\sigma_{max}}\right)^m dV, \tag{26}$$

where σ_{max} is the maximum stress experienced by the volume. It is thus an integral of the stress states experienced by the volume under loading with stresses normalized to a portion of the maximum stress experienced in the film. The effective volume thus represents the portion of the volume under loading in a test, that is actually at stresses levels in the range of the UTSes of a measured Weibull plot. Effective area could be derived in the same manner, and the effective area should be used in these equations when it is known that the defect distribution of a material is dominated by defects that scale through the area of the material rather than volume, for example in the cases of surface porosity and critically sized defects in the interfacial layers between substrate and thin film.

This volume or area depends on the loading conditions; for bulge testing, it is commonly assumed that uniform biaxial tension is prevalent in the whole film volume, and thus the effective volume is the whole volume of the film, and the effective area is then the whole area of the bulge. In this case, $V_{eff} = V$. This is very well the case in the center of the bulge, but as is noted in [93] and visualized in figure 14, the stress state varies when moving from the center of the bulge towards the edges.

In this case when the stress state is not uniform throughout the film area, the effective volume under stress will not be the actual full volume of the bulge film. In this case, the measured scale factors should scale according to the effective volume and $V_{eff} < V$. Also it should be noted that it could be possible that the stress field varies through the thickness of the film as well (for example with three point bend, only the top half of the sample is in tension whereas the bottom half of the sample is in compression [9]), which could also affect the effective volume. However, FEM simulations done in [103] have shown that the thickness of the film should be in very close to uniform tension and thus the effect of this on effective volume should be minor.

There is very little literature on the effective volume or area under loading in a bulge testing setup. Often an assumption is made that the film is under unibiaxial and homogenous tensile stress throughout its volume and area (as is done in [96]), and hence the effective volume is taken as the whole volume of the bulge film, and the effective area being the area of the bulge. This may lead to discrepancies, when the UTS results are extrapolated to different material volumes.

However, as the stress state is not completely uniform in a bulge testing setup, its effect on the results should be assessed. In a more recent, yet unpublished, study [103], the effective volume under loading in a bulge test setup is determined from FEM modelling, and it is considered dependant on the Weibull shape parameter of the material. This follows from the fact that the Weibull shape parameter describes the uniformity of the defect distribution in a film material. The higher the shape parameter, the more evenly spread the defects are and the more uniform they are in size. As the highest stress in the film is found in the central region, a higher shape parameter indicates that a defect that causes failure is found in a smaller area around the central region. While it may not be an indication of better quality, a material with a higher shape parameter is more predictable in its fracture than one with a small shape parameter. [55] The initial results show that with a shape factor of 3, the effective volume is around 60 % of the volume, and already at a shape factor of 10, the effective volume is close to 40 % of the actual volume [103]. The same ratios should be applicable for effective area as well. However, these results are initial and thus it is not reasonable to assess the effective volumes of the bulge tests in this thesis based on this information. Thus, once the study will be published, more accurate analysis of the results of this thesis can be done using the calculated accurate effective volumes.

As the Weibull plot links volume (or area), stress and failure probability, it can be used to extrapolate results from a film of known volume or area, to films of differing volumes or areas through the equation (13). However, this is naturally only related to the statistical distribution of defects and thus it does not take into account possible

changes in defect distributions, when films of different thicknesses are fabricated. Nevertheless, it gives a reasonable estimate for the UTS of a film of differing size, which can then be adjusted depending on knowledge from the deposition processes. Care must also be taken when comparing the results to other loading geometries than bulge tests, as the effective volume under loading may vary greatly. [55]

As mentioned earlier, the dominant cause of fracture can be stress concentration on surface or volume defects, and this leads to the UTS scaling with either the surface area or the volume subjected to stress. By using the equation (13) with either the ratio of areas or volumes, we can also evaluate whether the UTSes of aluminum nitride thin films scale through area or volume, and thus whether surface or volume defects dominate in fracture nucleation.

By using analysis of the Weibull plots, more information on the fracture properties of the AlN thin films studied in this thesis can be obtained from the UTS measurements, than if only averages from the measurements would be used. The defect distribution of the films can be analyzed using the equation (13), when films of two different thicknesses are tested (W1S50 and W4S200). The mechanical reliability of AlN thin films in applications can be extrapolated from measurements in this thesis, when effective areas or volumes under loading will be taken into account, and thus the mechanical reliability of these thin films can be evaluated.

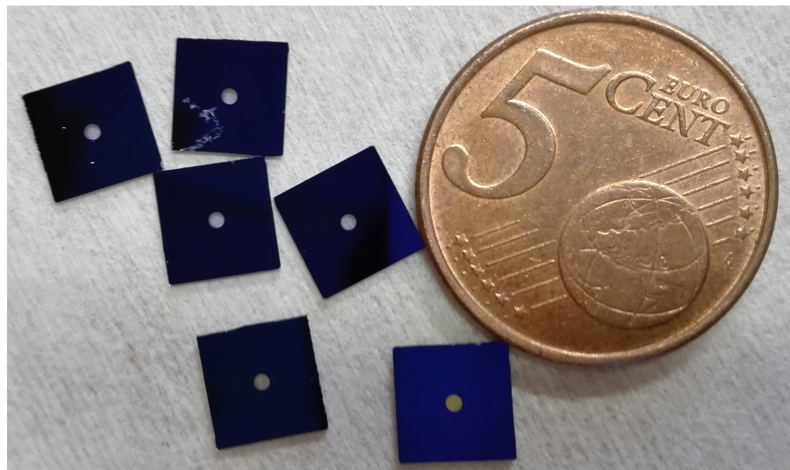

Figure 18: W4S200 samples with intact bulges. The bulge is poorly visible due to the transparency of the thin films and only the bulge on the bottom right sample is well visible.

8 Samples and sample preparation

The bulge test requires free standing membrane structures with a controlled diameter, and due to the device properties, the sample pieces should be of a certain size. In order to produce this kind of samples from films deposited on silicon wafers, a set of fabrication steps is required and those will be explained in this section.

The experiment in this thesis, as explained previously in section 7, consists of multiple experimental paths. The main path of sample fabrication is the same for all samples, while the samples that are tested with the Helsinki University device require an additional step for attaching the sample on a PDMS sample holder (see section 8.6), and the rectangular samples used in fracture toughness measurements (W5S200R) (see section 22) require an additional FIB milling step explained in section 8.7.

The general sample fabrication steps go as follows: The backside of a silicon wafer with a deposited AlN thin film on its front side (the films were deposited using the process parameters reported in sections 8.1.1 and 8.1.2) is coated with Al_2O_3 using an ALD device (see section 8.2). This Al_2O_3 film is then patterned using photolithography and wet etching procedures in order to produce a hard mask for through wafer etching (see section 8.3). A through wafer etch is then done using the Bosch process dry reactive ion etch (DRIE) (see section 8.4), while using a dummy wafer in order to prevent samples from falling into the reaction chamber. The samples are then detached from the dummy wafer and cleaned to remove any residues on the bulge film, which is explained in section 8.5. After these steps a sample bulge as shown in figure 18 is ready and for the samples that require the above mentioned additional steps, steps described in sections 8.6 and 8.7 can be done. All of the aforementioned steps are presented in detail in the following sections.

8.1 Sample material

Three different types of films are tested in this study; two sputtered films produced by Murata, (WxS50 and WxS200), and one MOVPE film (W7M100BX). The films are deposited on silicon wafers, which are then separated into square sample pieces of 7 mm x 7 mm in the sample fabrication process. 96 samples in total are produced from each wafer, although due to sample handling during fabrication process some samples are broken prior to testing. The material that was used in this study is presented in table 2 with some relevant wafer parameters.

Table 2: Sample material

Wafer code	Wafer thickness (μm)	Wafer size (inch)	Intact samples
W1S50	450	4	57
W2S50	450	4	31
W4S200	450	4	68
W5S200R	450	4	87
W7M100BX	950	6	92

The first two letters of a wafer code (for example W1) stand for wafer and a running numbering. After this, the next letter stands for the deposition method with S being sputtering and M being MOVPE. The next two or three numbers stand for the intended (goal thickness in deposition) thickness of the film in nanometers (these are accurately measured for each wafer in table 4). The further letters on W7M100BX were given when the plan was still to produce further MOVPE films, and now that no other MOVPE films were studied, those letters can be disregarded. The R in W5S200R stands for rectangular samples (used for fracture toughness measurements). All the wafers used are (111)-silicon with all other wafers than W7M100BX being double side polished. The code used in the thesis for W4S200fat stands for W4S200-samples that have been fatigue cycled.

An attempt was made to produce samples from 200 nm MOVPE-films as well. However, during the release of the membranes in through wafer etching, the bulge membranes fractured almost instantaneously when the etch reached the membrane. This is very likely due to the tensile residual stress in the film, arising from the high processing temperature used in MOVPE. It can be estimated through knowledge of the UTS (approximately 2.8 GPa) of the thinner MOVPE film, W7M100BX (reported in section 9.4, that the residual stresses in the 200 nm MOVPE films exceed the UTS of the film and thus cause instantaneous fracture, when the support of the silicon substrate is removed.

8.1.1 Sputter deposition

The sputter deposition procedure was done at Murata. Pulsed DC sputtering is used with a 6N aluminum target under a 10 sccm argon and 50 sccm nitrogen atmosphere,

with vacuum pressure of less than 0.1 μtorr and sputtering pressure of 2.5 mtorr. 6 kW sputtering power is used at 100 kHz frequency with 60 % duty cycle. Films of two different thicknesses were deposited and the sputter deposited wafers used in this thesis are coded W1S50, W2S50, W4S200 and W5S200R.

8.1.2 MOVPE

A three step process was used for the deposition of the MOVPE film used in this thesis (W7M100BX). The first step is bake process at 1025 °C temperature and 300 mbar reactor pressure, with the wafer being first 5 minutes in H_2 atmosphere and then 10 minutes in Si_2H_6 atmosphere.

The second step is a low-temperature AlN growth step at 980 °C with two phases. First, initial nitridation is done for 15 seconds at 100 mbar reactor pressure with NH_3 being fed at 15 sccm. The second phase is 3 minutes at 67 mbar reactor pressure with 336 sccm NH_3 and 56 sccm TMAl flow and a V/III ratio of 337.

The third step is the main growth process, where the other process parameters are the same as the second phase of the low-temperature AlN growth step, while the temperature is increased to 1085 °C. The duration of the third step was in the case of the 126 nm W7M100BX samples approximately 15 minutes.

An attempt was made to fabricate samples from a 196 nm MOVPE deposited film, but the sample films fractured during the release of the membranes in through wafer etching. Thus the only sample wafer with a MOVPE deposited film was the 126 nm film W7M100BX.

8.2 ALD aluminum oxide hard mask

ALD is used for Al_2O_3 hard masks used in the fabrication of the samples. The ALD process for Al_2O_3 is well established and the effects of temperature and substrate on the produced film are reasonably well documented.

For Al_2O_3 deposition, it has been observed that higher process temperatures increase the etch resistance of the amorphous thin film produced. This needs to be taken into account when defining the wet etch process for the hard mask and should be thought of when considering dry etch selectivity between this Al_2O_3 hard mask and silicon. The mask should be thick enough to prevent it from being consumed in the DRIE process, and with the selectivity of 66000:1 between Al_2O_3 and silicon [96], a thickness of 50 nm was deemed adequate for through etches of 450 μm thick wafers. A thicker layer of 110 nm was used for the first wafer W7M100BX, which was 950 μm thick. The deposition of Al_2O_3 is done in a Beneq TFS-500 ALD device at 220 °C. The cycle times used are 0.1 s and purge time of 1 second, although 0.2 s cycle with 2 s purge was used for the thicker W7M100BX wafer as its backside was unpolished. For the first wafer, 1050 cycles were run and for all the other wafers, 518 cycles were run. The Al_2O_3 films were measured with the Plasmos ellipsometer, and the W7M100BX had a 124 nm film and the other wafers had film of 53–54 nm, with all wafers being successfully through etched and thus these film thicknesses were adequate.

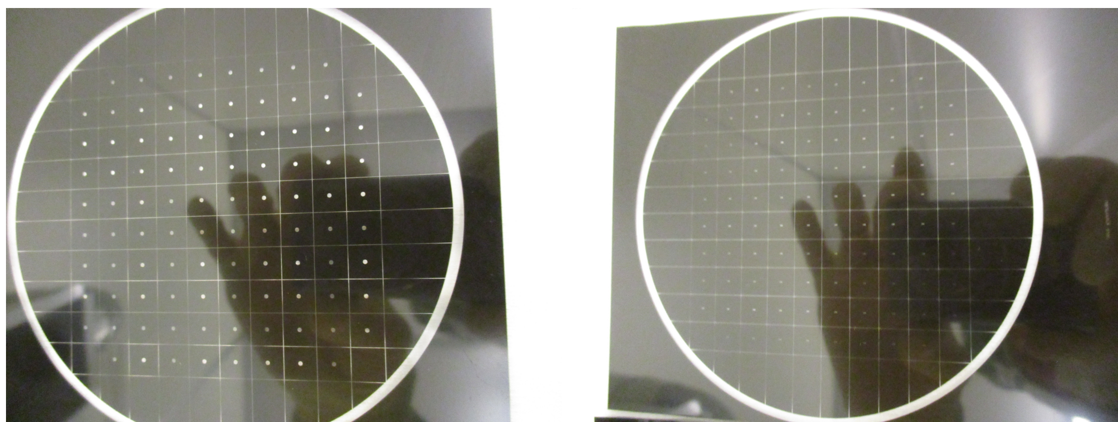

Figure 19: Plastic masks used in photolithography, 0.9 mm diameter circle openings on the left, 0.2x0.8 mm rectangles on right

8.3 Photolithography

Lithography is done on the Al_2O_3-coated backside of the wafer. The steps include photoresist spinning on both sides of the wafer (to protect the AlN film from the developer solution and aluminum etch acid) and soft baking with a hot plate at 110 °C for 50 seconds for both sides of the wafer. Then a plastic mask (shown in figure 19) is used in the Süss MA-6 mask aligner device, which exposes the photoresist through the mask openings. Then, the sample is developed in a AZ 351B developer for 1–3 minutes to remove the resist from the exposed areas. The developer etches AlN as well [107], although in our case the film is protected with a photoresist layer and thus will not be significantly damaged.

The wafer is then hard baked again for 50 seconds at 120 °C, after which the actual Al_2O_3-patterning takes place in aluminum etch with 50 °C solution temperature. The thickness of the hard mask Al_2O_3 is around 53 nm and the etch rate of aluminum etch is reported to be 11 nm/min for Al etch at 50 °C and thus an etching time of a bit under 5 minutes should suffice. However, etching time of 7 minutes is used to ensure thorough etching of the Al_2O_3 hard mask. This can cause some overetching, but that will be accounted for when measuring the bulge diameters, and thus causes no risk to the measurement results.

After the aluminum oxide pattern is thoroughly etched, the resist is removed from both sides of the wafer using a standard photoresist removal process, where the wafer is immersed first in ultrasound agitated acetone for 10 minutes, then in a non agitated acetone bath for 10 minutes and finally in isopropanol for 10 minutes. Rinsing in DI water is done between these three steps, and finally after the IPA bath, a rinse and dry procedure is run in a rinse dryer.

8.4 DRIE process

The device used in this thesis work is the STS Advanced Silicon Etch (ASE) inductively coupled plasma-reactive ion etcher (ICP-RIE) etcher, and it has a very well established

process for through wafer etching of silicon. Different hard mask materials can be used and Al_2O_3 is preferred for its easy deposition process via ALD and its high selectivity (66000:1) to silicon in this process [96]. As interest lies in through wafer etching, with the etch stopping only at the aluminum nitride thin film, it is necessary that the etching process does not etch AlN. A nm/min scale etching rate of AlN in a cryogenic etch process is reported with SF_6-O_2 process chemistry and it is also pointed out that AlN is very resilient to chemical etching under this chemistry, and the etching is primarily caused by the sputtering effects [108]. It can thus be expected that AlN works as an etch stop layer in a SF_6-C_4F_8-O_2 Bosch process etch as well, with etching of the AlN film being of minor significance, although no thickness measurements on the free standing bulges could be conducted due to their transparency. Thus it cannot be verified that no etching of the AlN has taken place.

The STS ASE etching device is thus used, with the 4-inch wafers being attached to Al_2O_3 coated 6-inch dummy wafers to prevent the detached samples from falling into the etching chamber. The wafers are attached AlN side towards dummy wafer with a layer of thick AZ4562 photoresist, and hard baked for 15 minutes at 120 °C on a hot plate.

The STS ASE process is run with flows of 129 sccm SF_6, 85 sccm C_4F_8 and 10 sccm O_2. The plasma generating RF power is 600 W and runs at 13.56 MHz. The platen power is 15 W. The etch rates were measured for each of the wafers with a Dektak profilometer after 20 cycles and the resulting etch speed (on the bulge cavity area) has been used to calculate the approximate amount of cycles required to etch through the wafer. The etch rate may vary depending on the location on the wafer and the temperature of the wafer, and thus the measured etch rate with the profilometer is only used as an approximate. The actual moment when etching has gone through can be seen by looking at the wafer inside the etch chamber through a window in the machine, and then verifying the result by looking at the bulges through a microscope once the wafer is taken out of the etcher. When nearing the value where etch should reach the thin film, shorter sets of 5 or 10 cycles are run until it can be verified that all the bulges are completely through etched. Over etching is thus possible, however as AlN is reasonably inert to this etch process [108], it should not be damaged significantly. Nevertheless, the bulge diameter may grow slightly as silicon continues to be etched, and for this reason the diameters of the bulges are verified with optical microscopy (measured diameters reported in section 9.1.3) and thus the actual diameter change can be accounted for. The measured etch rates and actual cycle amounts run are reported in table 3.

8.5 Sample detachment and cleaning

After the DRIE process, samples are detached from the dummy wafer by immersing them in acetone for around 12-24 hours. Acetone dissolves the photoresist and makes it possible to detach the samples from the dummy wafer without damaging the free standing membranes. The samples from W7M100BX were still very well attached to each other (due to cut lines not being through etched) and thus it was easy to clean the samples well enough with only acetone, but for all the other samples, an

Table 3: Etch rates and amount of cycles run on each of the wafers

Wafer	Measured etch rate (μm/cycle)	Cycles run
W1S50	1.42	315
W2S50	1.45	320
W4S200	1.463	320
W5S200R	1.401	321
W7S100BX	1.433	790

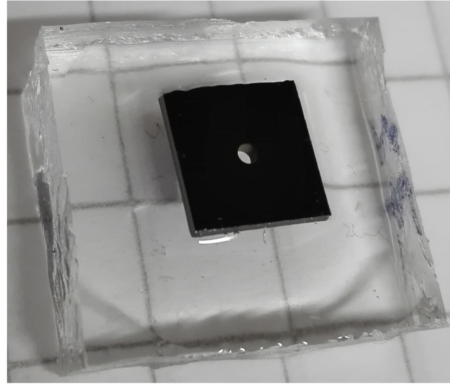

Figure 20: A W7M100BX sample attached to a PDMS holder.

additional cleaning procedure is needed after detachment in order to remove all the resist residues that could affect the bulges mechanical response.

All the other samples except for W7M100BX ones are cleaned in an Oxford Instruments plasma stripper PRS900. The process is run for 15 minutes with the samples being placed on a dummy wafer. The result of the cleaning process is then evaluated with a microscope and simultaneously the bulges are visually inspected for any damage. The broken samples and clearly damaged samples are discarded.

8.6 PDMS sample holder attachment

For testing with the device at Helsinki University, the samples need to be attached to a sample holder (shown in figure 20) as the testing setup requires it. This has been previously done with polydimethylsiloxane (PDMS) [96] and it has been used in this thesis as well. The PDMS that is used is Dow Corning 184 sylgard kit and it includes the actual PDMS and a curing agent, which are mixed at a ratio of 10:1 PDMS to curing agent, and then cured in an oven for 2 hours at 60 °C. Suitable pieces of PDMS are then cut and a hole is punched through the PDMS piece, on top of which the sample is attached with PDMS droplets. The attached sample-PDMS pieces are then cured again in the oven to secure the attachment. A picture of a sample on a sample holder is presented in figure 20.

8.7 FIB milling of fracture toughness sample pre-cracks

Helios focused ion beam device is used to produce pre-cracks in the rectangular bulge films used for fracture toughness measurements. A 5 μm crack is introduced with the beam using a 30 kV acceleration voltage and 28 pA beam current. The FIB device has an inbuilt micromachining program that can be used to produce various geometries on the film, and a rectangle with 5 μm x 50 nm length and width is used to produce the crack, with milling depth (milling program parameter that decides the duration that the milling beam stays in one place) of 1 μm chosen so that the crack will penetrate the whole thickness of the sample film. Some of the resulting cracks were measured with the *in situ* SEM in the device and the crack lengths were a constant 5 μm, whereas the crack width was in the range of 120-160 nm.

The first experiments with pre-cracked samples fabricated with lower beam currents and milling times did not affect the UTS of these samples in any way although the cracks were clearly visible in both SEM and optical microscopy. These cracks of 15-50 μm were most likely not through the whole thickness of the sample, and with proper milling parameters, the samples fractured in the FIB device when approximately 15 μm crack length was exceeded during milling, which is most likely due to residual stresses. This is, however, an interesting finding in the sense that only through thickness cracks were found to lower the UTS significantly.

9 Results

This section presents the measured results obtained through the experimental methods explained in section 7. Only the actual results are reported, and all further analysis of the results is done in section 10.

9.1 Film characterization

This section presents the results obtained with the characterization methods explained in section 7.3. The thicknesses of the tested films are measured through ellipsometry (section 9.1.1), the diameters of the tested bulges are measured with optical microscopy (section 9.1.2), the quality of the bulge fabrication results is assessed with SEM imaging (section 9.1.3) and the quality of the films is assessed through use of XRD scans (section 9.1.4).

9.1.1 Film thicknesses via ellipsometry

The thicknesses of the deposited films were measured using an ellipsometer. The thicknesses are averages from 5 measurement points randomly chosen on the wafer surface, and thus the thicknesses listed here are thicknesses of the deposited film on the wafer before any sample fabrication was done. The results are presented in table 4.

Table 4: Thicknesses of sample AlN films.

Wafer	Thickness (nm)
W1S50	54.8
W2S50	55
W4S200	220
W5S200R	221.1
W7M100BX	126
W8M200*	196*

The W8M200 film was a thicker MOVPE deposited film, which fractured during sample fabrication and thus no measurement results from this film could be obtained other than the thickness listed here.

9.1.2 Diameters using optical microscopy

An optical microscope is used to measure the diameters of each of the UTS-tested samples. The average diameters from each sample set are listed in the table 5, although for sample sets W1S50/W2S50 and W4S200fat, the actual measured diameter for each sample is used when calculating the UTSes, which is reported in section 9.4. For W4S200 and W7M100BX sample sets, the sample testing order was lost between

optical microscopy and UTS testing and thus only the average could be used. The error that is caused by the use of average diameters is discussed further in the section 10.6.3.

For the UTS tests of 50 nm sputtered films, 5 samples from sample set W2S50 and 25 samples from sample set W1S50 were tested due to shortage of successful samples from the W2S50-wafer. However, for these samples, the actual diameters measured are used in the UTS results and thus the average diameters listed on table 5 are only shown for general interest.

Table 5: Diameters of sample AlN bulges.

Wafer	Diameter (μm)	Min	Max	Stddev
W1S50	953.6	904.1	985.5	18.61
W2S50	975.0	969.7	982.2	4.182
W4S200	972.8	963.1	986.3	6.294
W4S200fatigue	976.5	964.7	985.5	5.513
W7M100BX	1013.9	975.9	1077.2	32.87
W5S200R*	272.1*	264.4*	283.4*	6.287*

The values for W5S200R are the widths of the rectangular membranes at the center of the membrane.

9.1.3 Micrographs from scanning electron microscopy

Some intact (figure 22) and fractured bulges were inspected using the field emission scanning electron microscope JEOL JSM-6335F. From the SEM images, it was found that overetching of the bulges was common, with bulge diameters varying by 20–100 μm from the mask diameter. The bulge overetch can be seen from the SEM micrograph in figure 21. The bulges may have different levels of overetching depending on which part of the wafer the sample is from, and this error is likely to be in the range of tens of micrometers and thus the diameters of all the UTS samples were measured, results for which are shown in section 9.1.2.

Tested samples were also imaged in order to investigate whether there are any traces of possible delamination of the bulge from the substrate. No traces of fractures extending on to the substrate side were found. If delamination would have occurred, it would be likely that the film fragments still attached to the substrate would be clearly delaminated from the surface of the substrate.

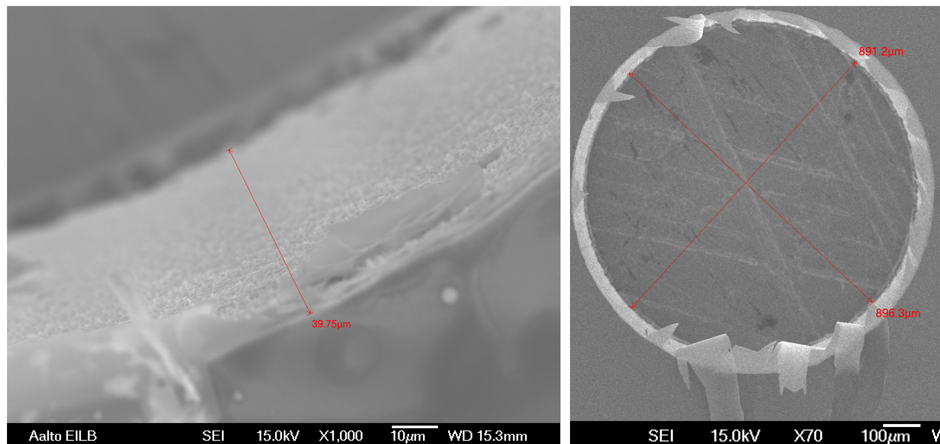

Figure 21: Overetching in W2S50 (left) and W4S200 (right) samples. Overetching visible as the lighter grey area in both images.

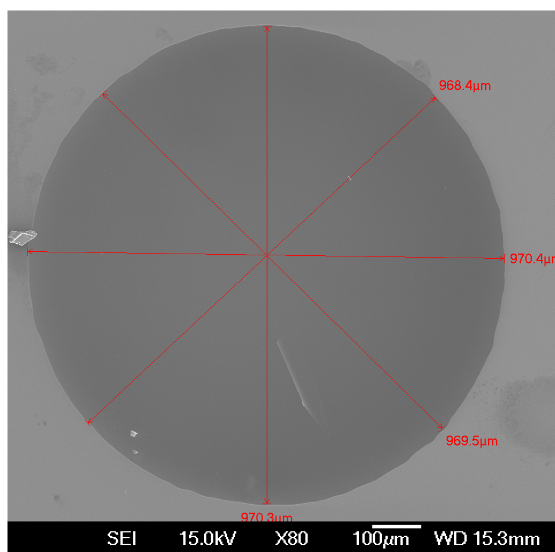

Figure 22: Bulge diameter of an intact W2S50 sample in a SEM image.

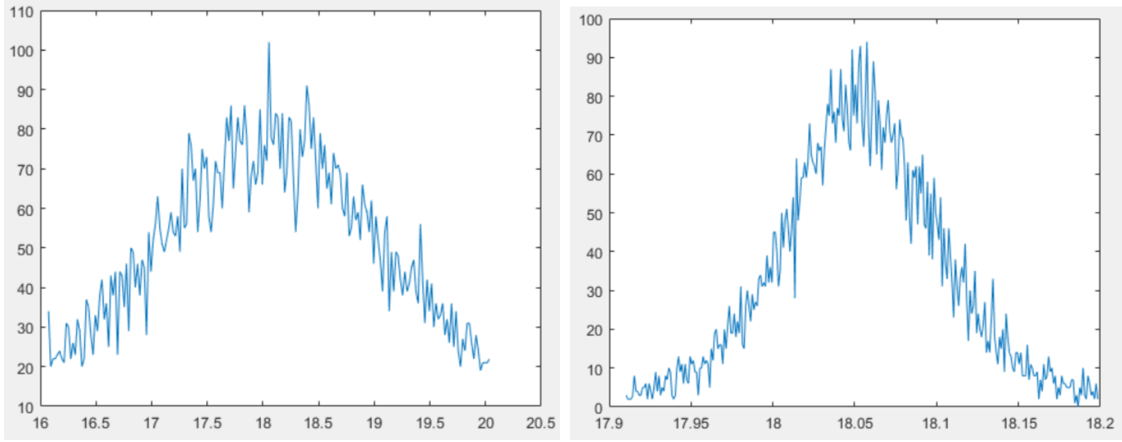

Figure 23: An example of ω- (left) and ω-2θ-type (right) scans for the W4S200 sample type

9.1.4 X-ray diffraction results

A sample from each tested film type was measured with the Panalytical X'Pert XRD (example data in figure 23). Both ω and ω-2θ-type scans were taken around the 002-reflection of AlN. There was a great variance in the reflection intensities from the different film types as can be seen in figure 24 (mainly the 50 nm sputtered film gave a very weak diffraction intensity) and for this reason and in order to produce comparable results, the full widths at half maximum (FWHM) and angles of peak intensity are calculated from Gaussian fits of the actual measurement data, and they are reported in tables 6 and 7. The XRD scans themselves are shown in figures 24-27.

Table 6: FWHMs and peak angles of sample AlN film ω-scans.

Wafer	FWHM (°)	Peak angle (°)
W1S50	7.7544	17.87
W4S200	3.93961	18.06
W7M100BX	1.15857	18.06

Table 7: FWHMs and peak angles of sample AlN film ω-2θ-scans.

Wafer	FWHM (°)	Peak angle (°)
W1S50	0.284933	18.05
W4S200	0.158526	18.05
W7M100BX	0.134789	18.06

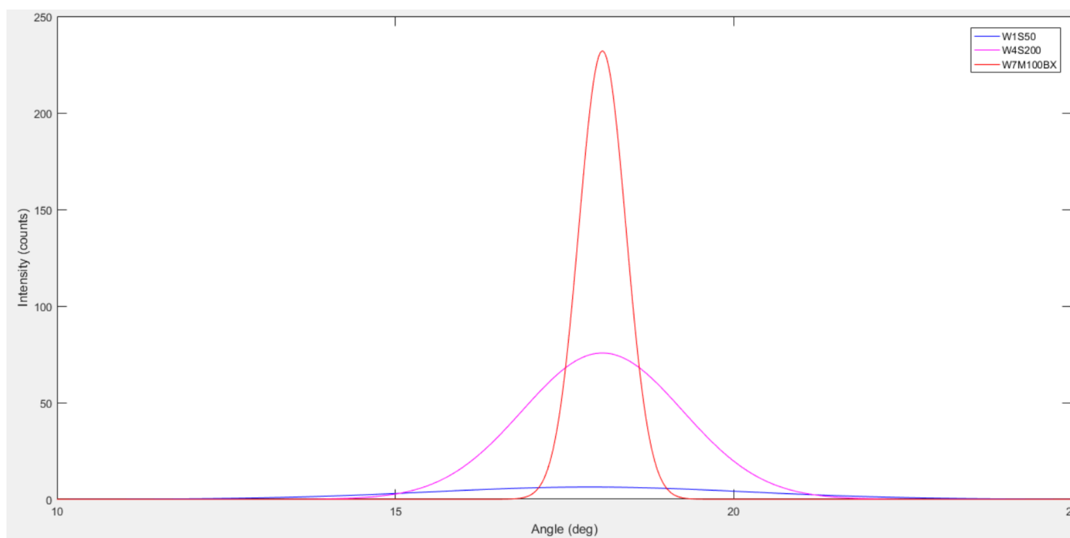

Figure 24: Gaussian fits on sample XRD ω-scans with difference of peak reflection intensities well visible.

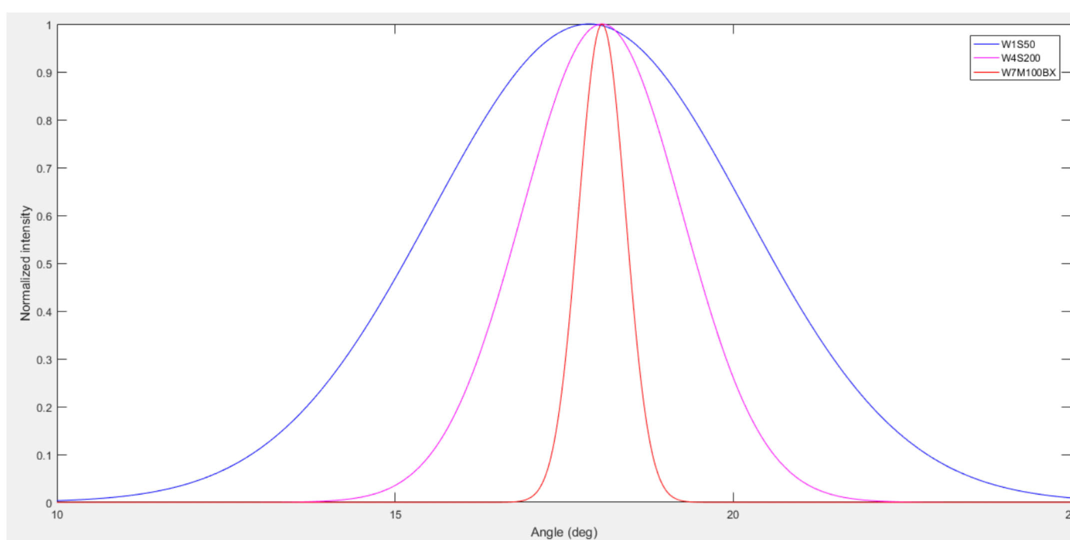

Figure 25: Normalized gaussian fits on sample XRD ω-scans with differences in peak angle and FWHM well visible.

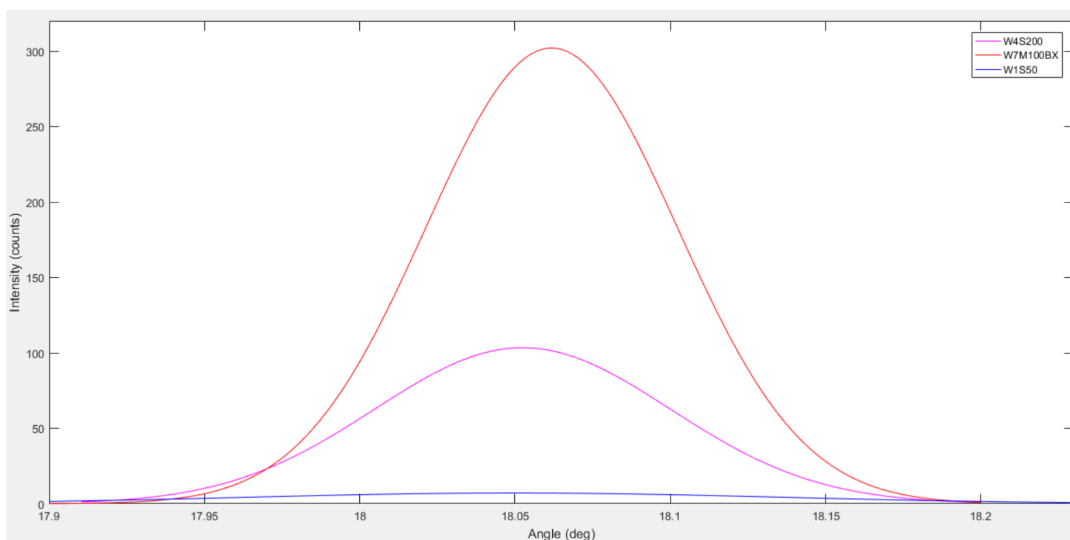

Figure 26: Gaussian fits on sample XRD ω-2θ-scans with difference of peak reflection intensities well visible.

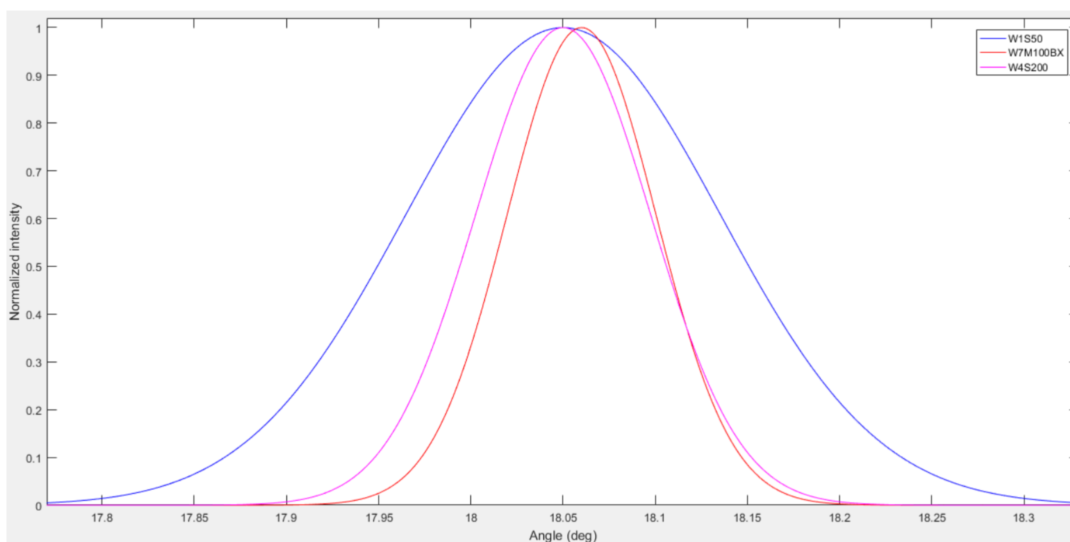

Figure 27: Normalized gaussian fits on sample XRD ω-2θ-scans with differences in peak angle and FWHM well visible.

9.2 Young's modulus

Young's moduli were calculated using displacement-pressure data obtained with the measurement equipment at Helsinki University (see section 7.2.5). The data is fitted with the equation (17), where Young's modulus and residual stress remain the only unknown variables, which are solved using the fit. An example fitted curve is shown in figure 29 and the results for all sample film types are presented in table 8. The results for residual stresses are obtained through the same curve fits and they are reported in section 9.3. A visualization of the data obtained with the Helsinki University equipment can be seen in figure 28 and an example of bulge displacement profiles at different pressure loads are presented in figure 30.

Table 8: Measured Young's moduli of sample films. (in GPa)

Wafer	Sample 1	Sample 2	Sample 3	Sample 4	Average
W1S50	332.5	338.9	336		335.8
W2S50	334.6				334.6
W4S200	339.7	343.2	337.8		340.2
W7M100BX	390.4	291.8	329.2	330.6	335.5
W4S200fatigue	338.8	351.8	329.2	329.2	337.3

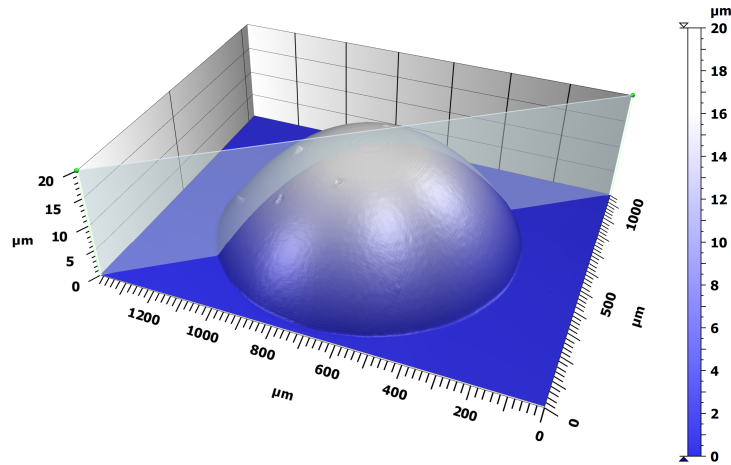

Figure 28: A 3D reconstruction from a W7M100BX bulge measurement at Helsinki University, with the line along which displacement profile is measured visible. Note that the height and width have differing scales.

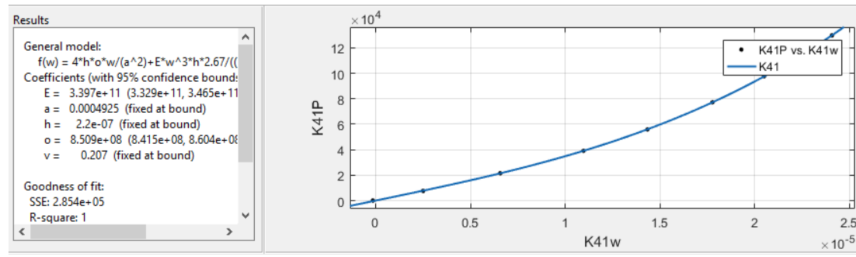

Figure 29: A curve fit on displacement vs. pressure data for sample 1 of W4S200 sample type, with calculated Young's modulus (E) and residual stress (o) visible.

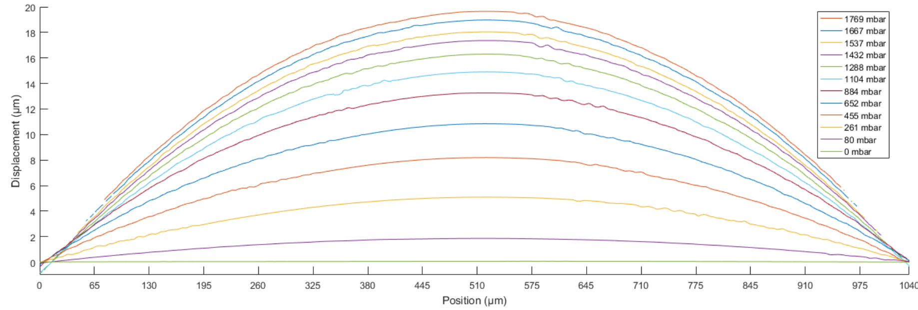

Figure 30: The displacement of a W7M100BX bulge at different pressure loads. Note that the pressure intervals are not uniform and the y- and x-axes have different scales.

9.3 Residual stresses

Residual stresses were measured through pressure-displacement data fits with equation (17) along with Young's modulus, and the measurement results are presented in table 9. The residual stresses in the films deposited at Murata were also measured through wafer curvature method with the average residual stress in W1S50 film being 212 MPa, in W2S50 274 MPa and in W4S200 738 MPa. These results show good agreement with our results, with variation being possibly explained by differences in the measured areas of the film between the whole wafer area in measurements done at Murata, and a sub-millimeter diameter circle in the bulge tests.

Table 9: Measured residual stresses of sample AlN bulges. (in MPa)

Wafer	Sample 1	Sample 2	Sample 3	Sample 4	Average
W1S50	262.1	163	312		245.7
W2S50	261.9				261.9
W4S200	850.9	823.2	963		879
W7M100BX	1636	1398	1479	1500	1503.3
W4S200fatigue	900.1	886.5	976.7	1040	950.8

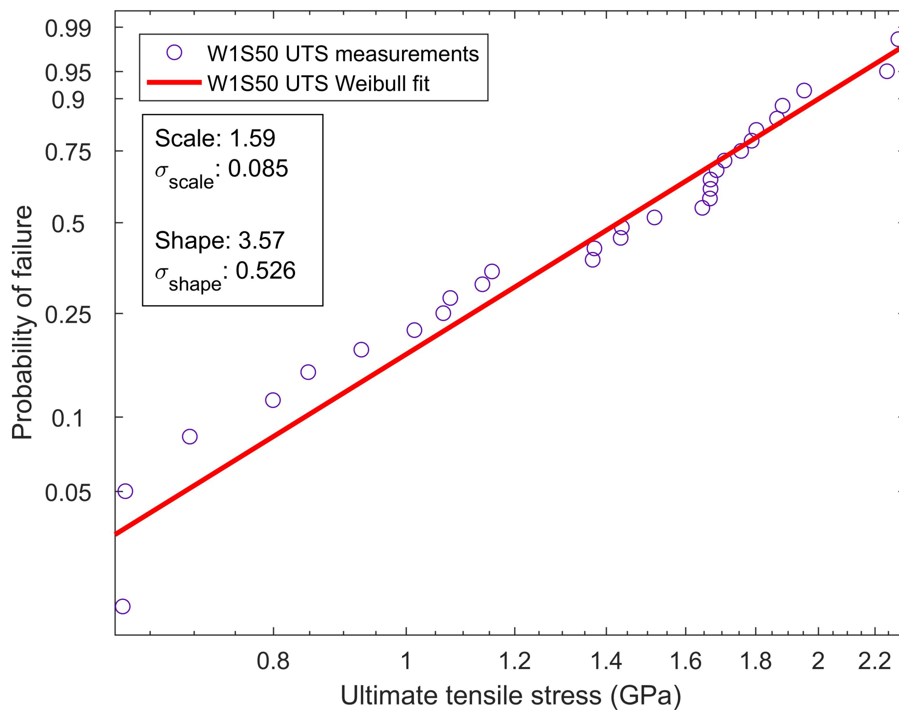

Figure 31: Weibull plot of the W1S50/W2S50-sample set, with scale and shape parameters given with their standard deviations (σ).

9.4 UTS results

Ultimate tensile strengths were measured using bulge testing for a sample set of 30 samples per each sample film type, with the exception of a set of 20 samples for the fatigue cycled specimens, using methods explained in section 7.2.1. The average Young's moduli presented in table 8 and average residual stresses from table 9 are used when calculating the UTSes through equation (18), with a Poisson's ratio value of 0.207 (see section 3.1.1). Diameters used are explained in section 9.1.2 and the thicknesses that are used are listed in table 4. For W1S50/W2S50-set, the aforementioned values of W1S50 sample set are used. As explained in section 7.4, the measured UTS values are of little use by themselves for brittle materials, and a Weibull plot and fit is thus produced from each sample set. The Weibull fits with their scale and shape parameters are shown in the figures 31-34.

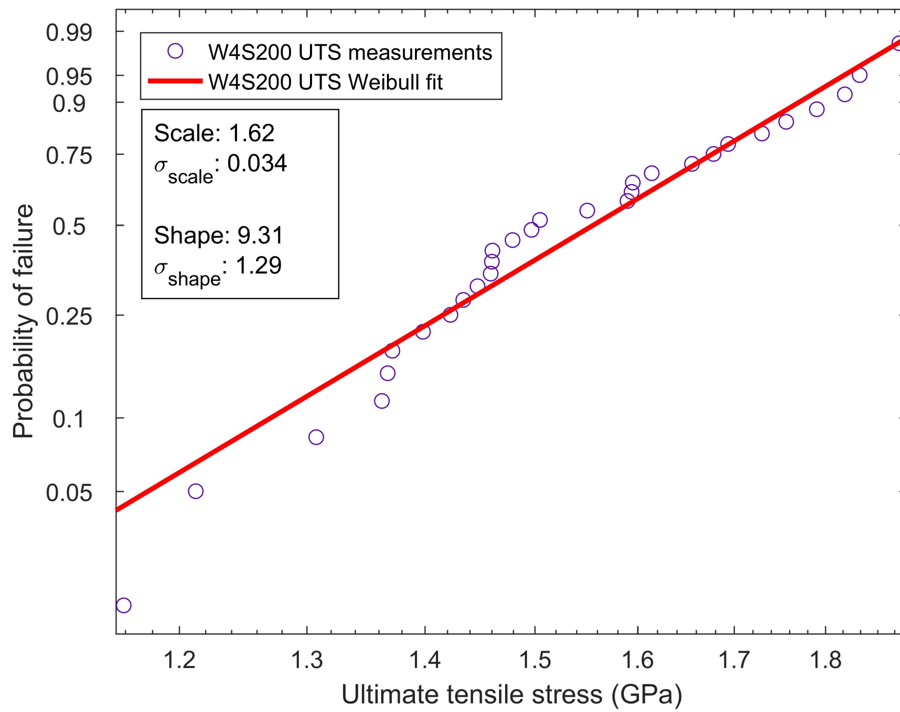

Figure 32: Weibull plot of W4S200 samples.

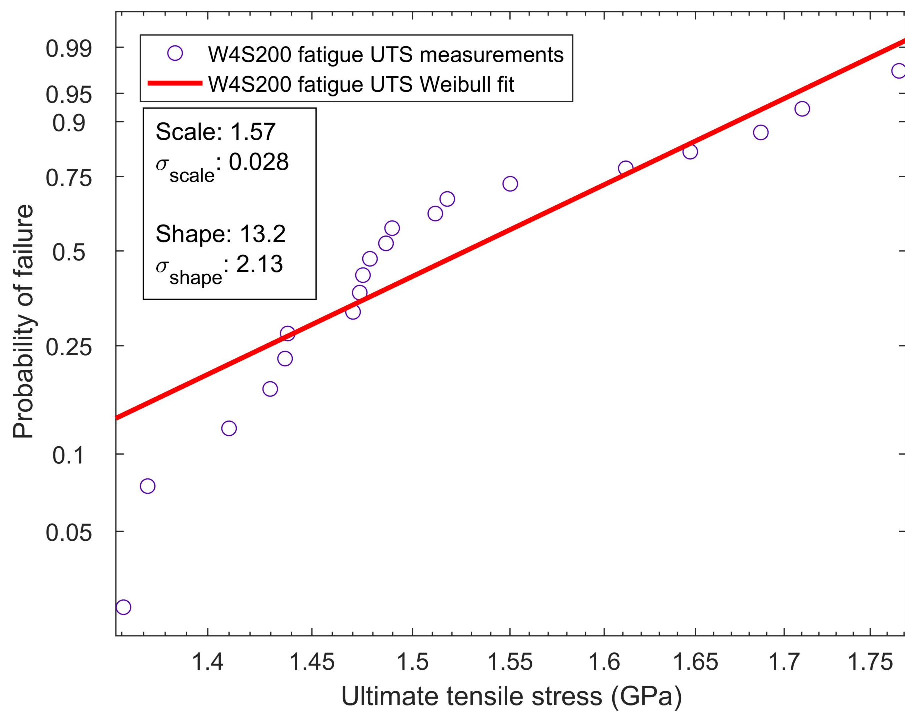

Figure 33: Weibull plot of fatigue cycled W4S200-samples.

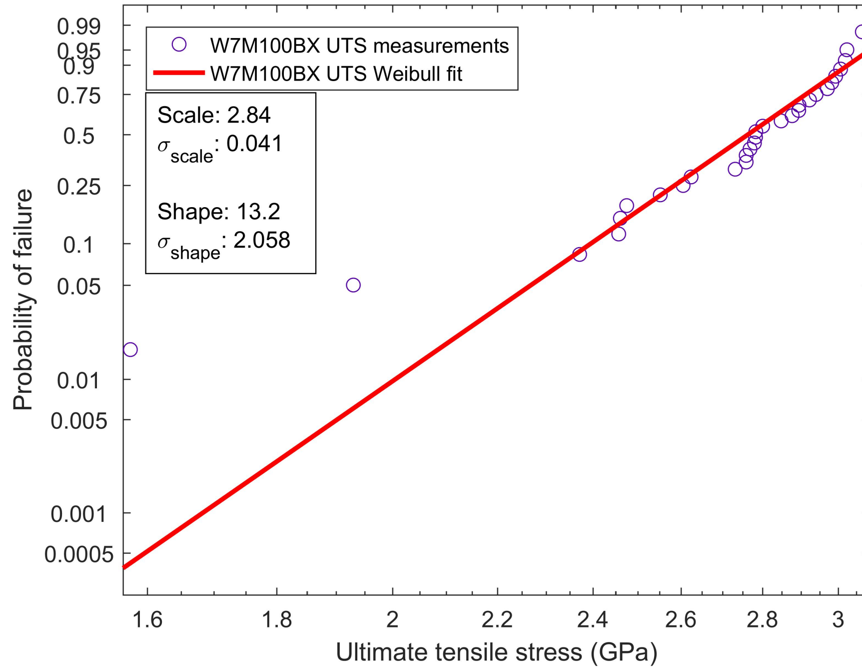

Figure 34: Weibull plot of W7M100BX-samples.

9.5 Fatigue

A set of 24 samples (W4S200fat) from the W4S200 wafer was cycled to 700 mbar pressure 10000 times in order to see if any measurable fatigue related changes occur in AlN films. 700 mbar of pressure yields approximately 1.23 GPa of tensile stress in these films, taking into account the residual stresses in the film, which translates to approximately 81 % of the measured average UTS of 1.52 GPa of the W4S200 samples. After cycling, 4 samples were measured with the Helsinki University equipment in order to calculate the Young's moduli and residual stresses in these films, and 20 samples were burst with the Micronova equipment in order to measure the UTS in these fatigue cycled films. The results are compared with those of non-cycled W4S200-samples in tables 10 and 11 in order to quantify any changes that fatigue cycling could have induced in the films.

Table 10: Comparison of the Young's moduli between fatigue cycled and non-cycled samples (in GPa).

Wafer	Sample 1	Sample 2	Sample 3	Sample 4	Average
W4S200	339.7	343.2	337.8		340.2
W4S200fat	338.8	351.8	329.2	329.2	337.3

A slight decrease of 2.9 GPa can be seen in the Young's modulus of fatigue cycled

Table 11: Comparison of residual stresses between fatigue cycled and non-cycled samples (in MPa).

Wafer	Sample 1	Sample 2	Sample 3	Sample 4	Average
W4S200	850.9	823.2	963		879
W4S200fat	900.1	886.5	976.7	1040	950.8

samples, although variance in the measurement results shows measured Young's moduli both higher and lower than those of non-cycled samples. The fatigue cycled samples measured a considerable increase of 71.8 MPa in residual stress to that of non-cycled samples.

The Weibull plots of both the cycled and non-cycled samples can be seen in section 9.4. The non cycled samples gave a scale factor of 1.62 GPa and shape factor of 9.31 (see figure 32), whereas the scale factor of fatigue cycled samples was 1.57 GPa and shape factor was 13.2 (see figure 33). The fatigue cycled samples thus show a slight decrease of 0.05 GPa in scale factor, with a considerable increase of 3.89 in the shape factor.

The relevance and possible implications of the results are discussed in section 10.5.

9.6 Fracture toughness

Fracture toughness was measured using rectangular membranes produced from W5S200 test wafer with a sputtered 221.1 nm AlN film. A 5 μm long pre-crack was introduced on the center of the membranes along its long axis, using the FIB device presented in section 8.7. A set of 8 samples was then pressurized until fracture using the Micronova testing device, and the pressure at fracture was recorded. Two distinct calculation methods are used to correlate the pressure data with stress, one that uses equation (20) to directly calculate the stress at fracture from the pressure at fracture (results presented in table 13), and a second method, where the displacement-pressure data acquired at Helsinki University with these rectangular membranes, is used to extrapolate displacement at fracture, and then equation (19) is used to calculate stress at fracture (results presented in table 14.

Equation (22) is then used to calculate fracture toughness (K_{Ic}), when crack half length of 2.5 μm is used. The film diameter (in this case the width of the film) is measured individually for each tested sample and used in the according calculations. The measurement scheme had some imperfections due to time restrictions, and these, and the produced uncertainty in the measurements, is discussed in section 10.6.4.

The Young's moduli and residual stresses from three measured rectangular sample films are presented in table 12, with average values calculated.

Table 12: Measured Young's moduli and residual stresses of W5S200R rectangular membrane samples.

Parameter	Sample 1	Sample 2	Sample 3	Average
Young's modulus (GPa)	341.7	228	471.8	347.2
Residual stress (MPa)	1067	954.4	1485	1168.8

As can be seen from the results above, the Young's moduli and residual stresses of these samples showed a great variance. The samples that were measured with the Helsinki University equipment were FIB pre-cracked with a 15 μm crack, as the initial idea was to measure displacement at fracture. However, the samples did not fracture at the pressure range available there, and after further experimenting with the Micronova equipment and the FIB process, it became reasonably clear that these earlier samples had only partially through-milled pre-cracks as in further experiments, fracture occurred at less than 1 bar pressure for a 10-μm pre-crack specimen. Thus, the large variance can possibly be accounted to the effect of this partially-through-thickness pre-crack and also partially to the variance in the shapes of the produced membranes following from varying over-etching in the membrane shapes. Nevertheless, the results from sample 1 show good acceptance with results from the circular membrane measurements for the sample set W4S200, which are of a similar film type (220 nm sputtered film), and thus the Young's modulus and residual stress of sample 1 will be used in the calculation of fracture toughness using the methods explained previously.

Table 13: K_{Ic} calculated using the pressure method and the equation (20), with the calculated stresses and fracture pressures presented as well.

Measurement	Pressure (mbar)	Stress at fracture (GPa)	K_{Ic} (MPa/m$^{1/2}$)
Sample 1	2558	1.626	4.556
Sample 2	3103	1.750	4.905
Sample 3	3055	1.764	4.944
Sample 4	3760	1.901	5.328
Sample 5	3149	1.771	4.964
Sample 6	1127	1.262	3.536
Sample 7	2903	1.728	4.844
Sample 8	3793	1.908	5.346
Average	2716.4	1.714	4.803

Table 14: K_{Ic} calculated using the displacement method, with the extrapolated displacements and according pressures and stresses presented as well.

	Pressure (mbar)	Displacement (μm)	Stress (GPa)	K_{Ic} (MPa/m$^{1/2}$)
S1	2558	6.90	1.63	4.57
S2	3103	7.70	1.76	4.92
S3	3055	7.63	1.77	4.96
S4	3760	8.54	1.91	5.35
S5	3149	7.76	1.78	4.98
S6	1127	3.97	1.26	3.54
S7	2903	7.42	1.73	4.86
S8	3793	8.58	1.91	5.37
Avg	2716.4	6.957	1.72	4.82

10 Discussion

The purpose of this section is to analyze the results reported in section 9. The results are of little importance by themselves when the mechanical reliability of these thin films is in question, and thus the implications of these results should be discussed. This is done is in this section, while also delivering error analysis on the measured values in section 10.6.

10.1 Implications of the XRD results

The results for both ω and ω-2θ-type XRD scans of 002-peaks are presented in section 9.1.4. The useful parameters from each scan are the FWHM and the angle at which the peak is located (Bragg angle). The results from ω-2θ scans compare well with literature values for slightly thicker sputtered films. [109] As clear peaks at 002-reflection angle were found for all sample types, it can be verified that the films are at least of polycrystalline nature with the crystal c-axes oriented perpendicular to the film surface. The scan types are different in geometrical nature, and thus the results from the different scan types should be assessed separately.

ω-type scan measures the variance in the c-axis directions of the crystal grains in the material. The variance is mainly caused by dislocations that cause grain misalignment, and part of the widening can be explained due to wafer curvature as well. However, with these small 7x7 mm samples, this effect does not seem very significant, as it can be seen that samples (W4S200/W7M100BX), that have larger residual stresses, have smaller FWHM than the thinner W1S50 samples. Thus, in this case, the wider FWHM can be thought of as a measure of defect density and grain misalignment, with W1S50 showing the poorest film structure and W7M100BX the best. [39] Any quantitative analysis is very difficult as all the affecting parameters should be well known, and thus these results remain a qualitative comparison tool between the films. The shift of the 002-peak angle in these scans is difficult to explain, although it could be related to a higher concentration of tilted grains in comparison to a better oriented material. AlN 002-peak should be close to 18 degrees, and any shift from that in ω-scans is caused by tilting of the refractive 002-plane in the film with respect to the surface of the substrate. [110]

In the case of ω-2θ-scans, the FWHM widening is caused by variation in the interplanar distance in the c-axis direction between diffracting 002-planes. This can be accounted to either the crystalline lattice being under a varying tensile stress, or to the effect of grain structure. Peak angle shift should be visible in a crystalline material under uniform tensile stress, but none is observed in the sample measurements. The FWHM's thus represent the variation of grain structure in the c-axis direction, with a greater FWHM being caused by more variation, which can as well be taken as an indication of smaller crystallite size and thus poorer crystalline quality. [39]

As a conclusion, it can be stated that the MOVPE deposited film W7M100BX shows the best crystalline structure in XRD measurements, with the 200 nm sputtered film being reasonably close in quality, and the 50 nm sputtered film showing the poorest quality.

10.2 Analysis of the Young's moduli and residual stresses

The results show very good consistency, with average Young's moduli in the range of 334.6–340.2 GPa. There is, however, significant experimental variance in the sample sets, and this variance is discussed further in section 10.6.

The average values show good agreement with the measured Young's modulus of bulk aluminum nitride (345 GPa [27]), while measurements from thin film samples show consistently lower values, as can be seen from the listing of literature values in table 1. When analyzing results from literature, it seems that an increasing film quality (better c-axis orientation, larger crystallites and less defects) may be behind a higher Young's modulus, as in the studies, where higher Young's moduli are measured, [48] and [49], a very well ordered crystalline structure is reported. In the bulge test experiment [50], a thicker film has a higher Young's modulus, and as is discussed in section 3.2, an increasing film thickness may result in a better crystalline structure. It should, however, be remembered that Young's moduli measured in different crystalline orientations may differ by as much as 100 % [94]. The Young's moduli obtained through use of nanoindentation are in the c-axis direction of the films, as opposed to the Young's modulus measured in this thesis, which is the one effective in the plane perpendicular to the c-axis of the crystals, which is likely to explain much of the discrepancy. Thus, it could be concluded, that the Young's moduli measured in this thesis are in agreement with literature, and are consistent with values from those measurements, where equally high quality films are studied.

The residual stresses presented in section 9.3 are well in line with previous findings with MOVPE films, and with the wafer curvature measurements of sputtered films. Formed residual stresses are greatly affected by fabrication process parameters and the substrate material used, which likely explains the discrepancy between the results presented in this thesis and those found in [50]. An interesting correlation can be observed in the W7M100BX sample set, which exhibited the highest UTS of the measured film types even though it had the highest residual stresses as well. These films withstood the highest pressures of all the tested film types, even if the thicker W4S200 sputtered films had smaller residual stresses and greater thickness. However, it is unlikely that the higher strength is related to any effect caused by residual stresses themselves, but rather the films were simply of higher quality, as is discussed in section 10.3.

Residual stresses increase when thicker films are deposited, which is observed between W1S50 and W4S200 sample sets. In [50], an observation is made that the increase in residual stresses continues to a certain thickness, after which the stresses begin decreasing. It is likely that such a phenomena would take place in the films such as the ones studied in this thesis as well, if thicker films were deposited. The thickness relation of the formed residual stresses was as well observed, when sample fabrication from thicker MOVPE films was attempted; the films burst during film release in through wafer etching, which is likely to be due to residual tensile stresses that surpass the UTS of these films.

Residual stresses above or close to the UTS make use of these films unreliable, as little additional tension will cause fracture in the film, especially if free standing

structures are fabricated. Even with films with smaller residual stresses, the residual stresses should be assessed in order to verify the range of stresses experienced by the film in the application, in order to verify that the stresses stay under the UTS of the film.

10.3 Analysis of the UTS results

The fracture properties of brittle ceramics are dominated by stress concentration on defects in the material. Through use of Weibull fitting, the probability of failure for a volume of material under a certain stress level can be calculated. The Weibull scale parameter denotes the tensile stress at which the probability of failure of the sample is 63 %, and the Weibull shape parameter m describes the spread of the probabilities of failure.

The scale parameter of the Weibull fit is a measure of the actual UTS of the film, which is primarily affected by the size of the critically sized defects in the material, directly through the equation (2.4). Smaller defects in the material lead to a larger scale parameter, and thus the material is able to withstand greater loads. Due to the loading condition in bulge tests, with only the central region being under the modelled stress level, it is likely that the smallest UTS values in the experiments are due to the fact that a critically sized defect happens to be in the very central region of the film. For the samples where fracture occurs at higher levels of stress (above the minimum UTS), the fracture can propagate from a defect of the same size as in the previously mentioned case, that is situated further from the center of the film, where the stress level is close to the value of minimum UTS of the film, or the fracture can propagate from a smaller defect in the central region of the film. However, if multiple defect populations with defects of different sizes are present in the film, it should be visible in the Weibull plot as non-linear increase of probability of failure with increased stress levels [55]. Indications of such behaviour can be seen in plots in figures 32 and 33, where probability of failure increases more rapidly, when going from 1.4–1.5 GPa, and then increases more slowly with further increase of stress. This would thus indicate that two defect populations are present in these films.

The scale parameters of sputtered films W1S50 and W4S200 are very close to equal. This would imply that both materials have the same critical defect size, which is an interesting finding considering the statistical volume effect usually in play in ceramic thin films. This finding is further discussed in section 10.4, with critical defect sizes calculated in section 10.7.1. The MOVPE-deposited W7M100BX sample set shows a much greater scale parameter of 2.84 GPa. This implies a much smaller critical defect size in the MOVPE films as compared to ones deposited via sputtering.

The m parameter is often taken as a measure of the distribution of the critically sized defect population. [55] As discussed in section 7.4, a higher shape parameter is found when the critically sized defects are evenly distributed in the material and are likely to be close to the same size. Although it is not directly a measure of good quality, it does make estimation of the materials reliability under stress states more robust.

The shape parameters of brittle materials are often in the range of 5–18 [55]. The

W1S50-sample set shows a great variance in the measured UTSes, and thus its shape parameter is a very modest 3.57. The value is very small, and due to this it is difficult to reliably predict the failure of these films at stress levels close to the stress level of its scale parameter, 1.59 GPa. The W4S200 sample set shows a reasonable shape parameter of 9.31, while W7M100BX samples show the greatest shape parameter of 13.2. The likelihoods of failure for these two films can be more accurately assessed at stress levels, where failure occurred in the measurements, and it is reasonably safe to assume that a single defect population of a reasonably dense distribution dominates the fracture of these films.

The implications of the results are further discussed in section 10.7.2.

10.4 Area or volume defects

As is explained in section 7.4, the statistical nature of brittle fracture should cause higher measured UTS values in specimens of smaller dimensions, with the measured UTS scaling either through volume or area difference between the specimens. The magnitude of the scaling depends on the Weibull shape factor of the specimens.

The equation (13) can be used to extrapolate the UTS for a different volume of material, when the Weibull scale and shape parameters are known. As we have measurement results from two different thicknesses of sputtered films (W1S50 and W4S200), we can use these two measurements to assess whether UTS of these films scales through area or volume, and thus whether area or volume defects are dominant in fracture nucleation.

Either the measurement results from W1S50 samples can be used to extrapolate upwards to a thickness of 220 nm, or the results from W4S200 can be used to extrapolate downwards to W1S50's film thickness of 54.8 nm.

When calculating downwards using the scale and shape parameter of W4S200 measurements presented in section 9.4 in equation (13), we find that the scale parameter of W1S50 should be 1.89 GPa instead of 1.59 GPa that was measured, if volume scaling was prevalent. When extrapolating upwards with the scale and shape parameter of W1S50, a film of 220 nm thickness (as in W4S200 samples) should have a scale parameter of 1.06 GPa. Both results show no agreement with the measurements, which was reasonably clear as the measured UTS (scale parameter) of W4S200 was higher than its 54.8 nm counterpart (W1S50), which cannot hold true if volume scaling of UTS is present.

The bulge diameters of these two sample types were the same, with slightly smaller average diameter in W1S50 samples due to differing through-etch results. The above method can be used with areas instead of volumes. The result when extrapolating upwards from W1S50 gives a scale parameter of 1.57 GPa for a film of the same diameter as W4S200, and vice versa, when extrapolating downwards from W4S200 diameter, the scale parameter of 1.63 GPa can be calculated for a film with the same diameter as the W1S50 samples.

The calculations discussed above indicate that the scaling of UTS in the sample sputtered films in this thesis is dominated by the area of the samples. This is an interesting finding as usually brittle fracture is dominated by defects in the volume of

the material rather than surface defects, and thus scaling should follow volume when the critically sized defects are uniformly distributed in the whole volume. The area scaling could be explained by defect formation during settling of the material to the preferred crystalline structure. As is visualized in figure 7 and discussed in section 3.2, the interface of the silicon substrate and the AlN thin film is highly defect populated due to the lattice mismatch between (111)-silicon and AlN, with possible additional effect from CTE-mismatch related residual stress relief through defect and dislocation forming. This would suggest that the defects found in the transition layer are larger than those that form during further growth of the layer at these thicknesses, and thus the transition layer defects dominate the fracture properties of these sputtered thin films. However, it should be considered, that further growth of the film from 200 nm upwards may produce a new critically sized defect population, which would then become the dominant cause of fracture nucleation in films of greater thicknesses.

It should as well be noted that there is a large difference in the shape parameters of these two sample sets. As the shape parameter is related to the defect distribution of the sample film, with a lower shape parameter meaning more randomly sized defects in the material, the difference in shape parameters would then mean that these two sample sets have a different defect distribution. The results of both the UTS measurements and the XRD scans (see section 10.1) point in this direction, and thus it is a valid assumption that the films have different critically sized defect populations. However, due to the nature of the extrapolation through equation (13), the extrapolated results are for a sample film that would have the same defect population as the tested material. Thus, if extrapolation of the UTS results for a thicker sample material is attempted, it is likely that using the shape and scale factors of the W4S200-sample set gives more realistic results, as the defect population of thicker films is likely to be closer to the one of the thicker W4S200 films.

As is discussed in section 7.4, the stress state in a bulge test is not uniform throughout the film, but rather decreases from the maximum in the center of the film to the minimum on the edges. Thus the effective volume of the bulge test is not the whole volume of the bulge film, but rather a proportion of it. The effective volume of the bulge test should be considered when extrapolating the results of these tests for use in applications. However, as little study is conducted on the effective volume of the bulge test, it is impossible to discuss further here. However, in the yet unpublished work [103], the effective volume is considered dependant of the shape factor of the sample film, and effective volumes for different shape factors are calculated. Thus, the results found in this thesis can be further analyzed using that knowledge, when the study is published and if the findings in the study are verified.

It can be concluded that it is likely that a critically sized defect population that scales through the area of the films dominates the fracture properties of these films. This population is likely formed in the transition layer of the films during deposition. The way this information can be used in the design for reliability of applications where these films are used is discussed in section 10.7.2.

10.5 Effect of fatigue

The fatigue cycling experiment is described in section 7.2.2. From the results presented in sections 9.4, 9.2 and 9.3, the effect of this kind of a fatigue cycling scheme on the mechanical properties of these thin films can be evaluated.

In the UTS results, the scale parameter of fatigue cycled samples shows a slight decrease of 50 MPa. This is, however, very close to the standard deviation of the measured results, and thus it is difficult to verify, if this effect is truly due to fatigue related changes in the material, or is the change only caused by experimental variance or error. It is, however, in the direction that would be caused by fatigue effects in the material, such as sub-critical crack growth or microcrack elongation, that are discussed in section 2.11. Either of the two effects could be in play, with defects extending slightly due to fatigue cycling and thus causing a slightly lower measured UTS.

However, the shape parameter of the Weibull fit shows a reasonably significant increase of 3.89 in the fatigue cycled samples. The shape parameter describes the uniformity of the defect distribution in the material. A change in the shape parameter would thus indicate, that the defect population in the material would have undergone a change. The direction of the change is in this case to the direction, that the defects have grown closer to the critical defect size, and thus a critical defect is more likely to be found in the central region of the film, and thus the fracture occurs at a smaller range of stress increase. The size of the increase is already so significant, that it is difficult to explain it with experimental deviation, although the smaller amount of tested samples may have a considerable effect. Nevertheless, the increase would suggest that some changes occur in the material, and thus a further study could be in place in order to verify the change, either with a larger sample set run for the same amount of cycles (in order to reduce the effect of experimental variation) or with a larger amount of cycles (to induce more significant fatigue effects).

The Young's modulus of the fatigue cycled specimens decreased by 2.9 GPa. This change is well in the range of experimental error, as can be seen from the range of results presented in table 8, and thus the results would suggest that fatigue cycling has no considerable effect on the Young's modulus of these films. However, as stated in section 3.2, a decrease in Young's modulus should be observed with increasing defect density. Thus, the direction of this change is in line with the slight changes observed in the UTS testing.

The residual stresses show a considerable increase of 71.8 MPa. This is hard to explain as fatigue cycling should rather relax residual stresses through defect and dislocation formation, or even through plastic deformation. However, as can be seen from the other residual stress results, it seems quite obvious that there may be very large local variation in the residual stresses in the films. This increase is thus most likely accountable to such an effect, although a much larger set of samples would be required to verify this hypothesis. Nevertheless it is verified that residual stresses do not relax during fatigue cycling, which verifies that no plastic deformation occurs, and is thus an important observation by itself.

In total, the decrease in the scale parameter, increase in shape parameter and

decrease in Young's modulus would point in the direction that fatigue would cause an increase in the defect sizes of the thin films. This could be explained by microcrack propagation or SCG, although it is difficult to accurately assess the cause of these changes without further experiments. Both polycrystalline and single crystal aluminum nitride are reportedly very inert, even at high temperatures, to water and oxidization and thus SCG in AlN should be negligible in normal ambient conditions [111], and it is possible that microcrack propagation would thus be behind the fatigue effects in AlN.

The changes are very small and close to the scale of experimental variation and thus it cannot be definitely concluded that any effect is actually in play, nor it is possible to conclude that absolutely no changes occur through fatigue. However, in a study with resonant AlN beams, fatigue failure was observed between 60000–335000 cycles, with clear fatigue related changes observed with dependence on the film quality. Thus it could be concluded that the results of this thesis are in line with those reported in literature. [21]

It can be said, however, that if any fatigue effects are in play, they cause no significant change to the mechanical reliability of these thin films at these stress and cycle levels. The results would suggest a further study with a higher amount of cycles and/or a larger sample set in order to verify the slight effect found in these measurements, as similar fatigue studies commonly use cycle amounts in the range of >100000 cycles [25], which was not possible in the scope of this thesis.

10.6 Error analysis

In this section, the most significant identified error sources in the experiments conducted in this thesis are assessed, and estimates on their possible effect on the measurement results are given.

10.6.1 Sample fabrication related error

Effects of geometry variance have also been discussed in [94]. There is a clear variance in the diameters of the bulges tested in this thesis and some roughness on bulge sides has also been observed. The rectangular bulges for fracture toughness testing showed clear rounding of both the bulge corners and the sides of the bulge. The rounded shapes differ from the assumptions made in the mathematical models, that are used to relate pressure-deflection data with actual stresses in the films. Imperfections in the bulge sides may cause stress concentration, that can cause fracture from points other than the center of the film, which is the point where the mathematical models are valid.

The imperfect shape of the bulges causes error in both the measurement Young's moduli and residual stresses, and the UTS measurements. Onset of fracture from edge imperfections causes error in UTS measurements. However, it could be expected that failure caused by these stress concentrations would cause a significantly lower measured UTS at fracture, than fractures originating from the center of the film, and thus cause outliers in the UTS data. This kind of outlying results (although the

defects that cause fracture at such low stresses cannot be accurately analyzed) can be seen, for example, from W7M100BX results in section 9.4, and the effect of only a few outliers to the Weibull fit and the resulting scale and shape parameters is very small.

10.6.2 Sensitivity of the measurements to Poisson's ratio variance

Due to the anisotropic nature of the hexagonal aluminum nitride lattice, Poisson's ratio depends on the orientation of the crystallite, and thus the direction of the applied stress. Thus, depending on the quality and orientation of the film, the Poisson's ratio can vary from 0.176 to 0.257. [39] A value of 0.207 is used in this thesis, as is explained in section 3.1.1. Nevertheless, it should be assessed how significantly the variance of Poisson's ratio can affect the measurements in this thesis.

A simple sensitivity analysis is conducted on calculation of the Young's modulus of the W4S200 sample 1 in order to see how significantly the change of Poisson's ratio from 0.176 to 0.257 changes the calculated Young's modulus. Residual stress results are not affected, as ν is not a factor in the residual stress component of the equation (17). Through fitting of the sample displacement-pressure data with the equation (17) with 0.176 as the Poisson's ratio, a Young's modulus of 350.6 GPa is calculated. Through use of a Poisson's ratio value of 0.257, the resulting Young's modulus is 321.7 GPa. The original value with 0.207 as Poisson's ratio was 339.7 GPa. Thus it can be concluded that a variance in the range of 28.9 GPa can be explained through variation of Poisson's ratio. This may, however, act differently in the different measurements, and a more mathematically rigorous sensitivity analysis should be conducted if more accurate assessment should be of interest.

In the case of UTS measurements, the effect should be less significant, as can be seen from equation (18). A similar quick sensitivity analysis is conducted on the W4S200 sample set, with the change in average UTS being analyzed. With ν=0.207, the average UTS is 1.537 GPa. With ν=0.176, average UTS is 1.525 and with ν=0.257, the average UTS is 1.561 GPa. Thus, only a change of 36 MPa is observed, which is insignificant considering the experimental error.

Thus, it can be concluded that the variation of Poisson's ratio has a significant effect on measured Young's modulus, and thus the values presented in this thesis are primarily comparable with results obtained with the same Poisson's ratio of 0.207. The UTS measurements are not significantly altered by variation in Poisson's ratio.

10.6.3 Effect of diameter error

The diameters of bulge samples used in this thesis varied due to a variable etching result. The through wafer etching had consistent variation on the wafers, with samples close to one edge of the wafer being etched faster than the other. In order to produce properly released bulge membranes, some samples had to go through overetching in the range of 5–10 cycles, so that the bulges on the other side of the wafer were completely etched through as well. This resulted in variance in the measured diameters of the membranes, which was not completely understood prior to the first measurements, and for this reason only the average diameter is used

for calculation with W4S200 and W7M100BX. In the case of Young's modulus measurements, the actual diameters were always measured by the SWLI-equipment, and there is no reason to doubt the accuracy of these measurements and thus a sensitivity analysis on Young's moduli results is unnecessary.

A simple sensitivity analysis on the average UTSes is conducted on W4S200 sample set, with minimum and maximum diameter from table 5 used. In addition to this, the average diameter is used on the W1S50 sample set to see if use of actual diameters versus average diameters has a considerable effect on the average UTS.

The average UTS of W4S200 with the average diameter in use is 1.537 GPa. When using 963.1 μm as the diameter, the average UTS of the W4S200 sample set is 1.5309 GPa, and with a diameter of 986.3 μm, UTS of 1.548 GPa is calculated. Thus a difference of 11 MPa is observed.

When using the average diameter of 953.6 μm instead of the actual measured diameters for each of the samples of W1S50 sample set, the average UTS changes from 1.4238 to 1.4231 GPa. A difference of 0.7 MPa is observed.

Considering the experimental variance and standard deviation of the measurements, the effect of diameter variation can be considered insignificant, and the use of average diameter values is justified.

10.6.4 Validity of the fracture toughness measurements

The initial plan was to follow the testing scheme presented in [14], which uses displacement versus pressure measurement in order to calculate the stress in the film at fracture, when a pre-crack of a known length is introduced on the center line of the long axis of the bulge membrane through use of FIB milling. However, during the course of the thesis, it became apparent that this kind of a measurement is only required when Young's modulus and residual stress of the film are poorly known beforehand. Equation (17) models the behaviour of a membrane under pressurization very well and thus an accurate value for Young's modulus and residual stress in a certain film type can be obtained. When these are known for a certain film type, the pressure-deflection behaviour and the resulting stress at the center of the membrane is well modeled by equation (18). It was proven through measurements that the same holds reasonably well for rectangular membranes, when correct values of the c-parameters are used, and thus the equation (20) can be used to model stress on the pre-crack during fracture toughness testing and no displacement data is required, when both Young's modulus and residual stress of the tested film are well known.

However, the displacement-pressure data obtained from the rectangular samples showed significant variance. Due to the initial idea of measuring displacement at fracture, the samples that were measured at Helsinki University had a 15 μm pre-crack introduced. However, it was only after these measurements that it was found that these pre-cracks were very likely not through-thickness, as no fracture until 3.75 bar was observed in tests with the Micronova device. The variation of the pressure-deflection data is likely to be due to these varying-depth pre-cracks, which then places the usability of the pressure-deflection data under doubt. The average Young's modulus and residual stress were very close to the results obtained from

W4S200-samples, and thus the range should be close to correct, and thus it is as well reasonable to assume that the results presented in section 9.6 are close to the truth. Nevertheless, it should be examined how much the variation from 228–471.8 GPa Young's modulus and 954.4–1485 MPa residual stress would cause in the results. Thus, the results for these cases are calculated for each tested fracture toughness sample in the same manner as in table 13, and the averages are given in the following table 15.

Table 15: Average fracture toughnesses calculated with Young's moduli and residual stresses from sample 2 and 3 in table 12, with the average result from sample 1 given as a reference.

	Young's modulus (GPa)	Residual stress (MPa)	K_{Ic} (MPa/m$^{1/2}$)
Sample 2	228	954.4	4.23
Sample 3	471.8	1485	5.81
Sample 1	341.7	1067	4.80

It can be seen that K_{Ic} would still remain in the range of 4.23–5.81 MPa/m$^{1/2}$.

As the film that is being pressurized in fracture toughness measurements has a crack through it, air flow through the crack may cause deviation of displacement-pressure behaviour from that of a non-cracked specimen. Thus, in order to obtain an accurate measure for stress on the pre-crack, a pressure-displacement curve should be obtained from a pre-cracked specimen, so that correct "effective" Young's modulus and residual stress can be calculated for use in the equations, that correlate displacement with stress at the center of the film. The stresses calculated through these formulas should be valid at given pressures, when the Young's modulus and residual stress used are valid for the specimen type, even though they would vary from the actual intrinsic Young's modulus of the film (hence the word "effective"). However, it could be estimated that the variation caused by the pre-crack is reasonably minor. Nevertheless, further measurements would be in place to rigorously verify how the pre-crack alters the pressure-deflection behaviour of the membranes.

The stress state at the center of the membrane is modeled through geometrical relations, which assume a certain shape of the deformed membrane. The etching result in the experiments in this study was not ideal, and thus the sides of the membranes have some curvature. This may cause variation to the stress field at the center of the membrane, the scale of which is hard to be quantified. In addition to this, the air flow through the crack during pressurization may as well cause variation in the stress concentration at the crack tips, which is equally difficult to account for. Measurements using water to pressurize the membrane have been demonstrated in [106], although it could be that this is primarily used in order to have static pressurization steps, where displacement can be accurately measured, which would not be possible when leakage is present. The effect of gas flow is assessed in [14] as well, where it is considered insignificant. The effect of imperfect geometry should nevertheless be minimized with measurements with a more well-defined etching result.

In any case, the results obtained in this thesis, even when considering the variation in the displacement measurements, are in the range of 4.2-5.8 $MPa/m^{1/2}$. This is still considerably above 2.6 $MPa/m^{1/2}$, that is measured for bulk AlN thin plates in [52]. This discrepancy is difficult to explain, as the effect of transition from plane strain to plane stress in thin films should be very minor with brittle materials as explained in [14], with effect in the range of few percents at maximum. This discrepancy could well be explained with material properties, which would suggest that this kind of polycrystalline thin films can withstand defects better than the amorphous bulk material. However, further study should be conducted to verify the result.

10.7 Evaluation of the mechanical reliability of AlN thin films

The purpose of this section is to discuss the ramifications of the measurement results presented in this thesis: how can the results be used to evaluate the reliability of AlN thin films in applications? The first section discusses the critical defect distribution that dominates the fracture properties of these films, with the second section focusing on how the measured parameters can be used in design for reliability.

10.7.1 Critical defect size in the sample material

With fracture toughness being measured, a critical defect size in these thin films can be calculated. Through use of equation (22), the defect width ($2a$) can be calculated, when both UTS and fracture toughness are known. This defect half width is the size of an ideal crack in the material that would cause critical stress concentration, and thus fracture, when aligned perpendicular to the direction of applied stress. In the case of bulge tests, the film is under symmetric unibiaxial stress and thus a defect in any orientation in the plane of the film is under the same stress.

Due to the loading condition of the bulge test, where maximum stress is close to the central region of the bulge, with stress decreasing when moving to the edges, it is likely that the minimum stress at which the bulges fracture in the UTS tests is the stress at which a defect of the critically sized defect population is at the central region of the film, and thus the UTS of that measurement is the stress at which this defect causes fracture (the effect of loading conditions on UTS results is further discussed in section 10.3). The maximum stress, at which the films fracture, then gives a lower limit to the defect size in the film, although due to the loading situation it cannot be verified if the defect that causes fracture in these cases is situated in the central, highly stressed, region of the film, or if the cause of fracture is a larger defect situated further from the center of the film. Thus, this lower limit is more theoretical and less reliable, and only defines a lower limit for the critical defect size that causes fracture in these films.

Using the measured fracture toughness presented in section 9.6 and minimum measured UTS values for the films (for W7M100BX, the first two measurements are ignored as outliers caused by possible damage during sample production and the

third smallest measured value is used), the critical defect sizes (CS) with their lower limits (LL) presented in the table 16 can be calculated for the different film types.

Table 16: Critical defect sizes (CS) and their lower limits (LL) of the different film types

Sample type	Min. UTS (GPa)	Max. UTS (GPa)	CS (μm)	LL (μm)
W1S50	0.62	2.29	38.2	2.8
W4S200	1.16	1.89	10.9	4.13
W4S200fat	1.36	1.77	7.92	4.7
W7M100BX	2.31	3.07	2.61	1.56

It should be considered that the stress concentrations caused by defects in a real material are probably smaller than that of an ideal crack (three dimensional bulk defects are not likely geometrically equivalent to an ideal crack), and thus the actual defects in the material are likely to be larger than those listed in table 16.

10.7.2 Design for reliability

The Young's moduli, residual stresses, UTSes, fracture toughness and fatigue response of these aluminum nitride thin films have been measured and assessed. Now, it is important to consider how can this knowledge be used when designing applications where this kind of films are used. The different parameters can be used in different fields of design, and some possible ramifications of these parameters to design with aluminum nitride thin films are discussed in the following text.

The Young's moduli affect the way these films respond to applied forces. The Young's moduli that are measured in this thesis are consistently larger than those reported in literature. What this implies is that less elastic strain, than what would have been expected when Young's moduli values from different contemporary studies are used, can be expected when a certain load is applied on the films. The inverse of this is naturally that an applied strain on the film will result in a higher stress loading. The higher stress required in order to induce a certain strain will naturally have implications when, for example, piezoelectric actuation is considered. It should, however, be remembered that the Young's moduli reported in this thesis are only valid for the (002)-plane deformation of AlN.

The residual stresses of fabricated AlN thin films should be quantified in order to accurately calculate the stresses that the film experiences under use. Accurate knowledge of the stress states is required in order to set ensure the UTS of the film is not exceeded. As the residual stresses vary greatly depending on the deposition process used, it is difficult to directly extrapolate the measured values from this study, and measurements for that exact film type should be conducted.

It can be expected that these AlN films can be safely operated at stresses that are under the levels where the first fractures occurred in testing. Thus, if absolute reliability is required, the minimum UTS values from section 9.4 should be used as

safety limits. If higher loads are nevertheless induced in operation, the probability of failure for that certain film can be assessed. If failure does not occur on the first time the film is loaded to a stress level, it is very unlikely that the film will fail on further loading cycles to the same load either, unless cycle amounts surpassing 10000 cycles are run.

The UTS results can be extrapolated to sample films of different thicknesses using the equation (13). It should, however, be used with caution, as the equation expects that the film of different thickness has the same defect population as the film that is used as the basis of the extrapolation. As discussed in section 10.4, it has been observed that the UTSes of sputtered films seem to scale through area rather than volume, and thus the relevant parameter in applications would be the area of the transition layer that is under loading in the application, rather than the volume of the film. Thus, films of different thicknesses are expected to fracture at the same stress loads.

The fracture toughness measured in this thesis can be used as well to extrapolate the fracture properties of the films studied in this thesis to those that are used in applications. If any hint on the size of the defects in the films can be found, fracture toughness can be used in order to calculate the films UTS. Likewise, fracture toughness can be used to evaluate how sensitive the films are to any defects that are, for example, induced in operation or fabrication of the films. Fracture toughness, being an intrinsic property of a material, should not change significantly between samples of the same substance, and thus the measured value should be well usable on AlN films with varying thicknesses and structures. However, further study with, for example, amorphous films should be conducted in order to verify no relation between the crystalline structure and the fracture toughness of the material exists.

The properties that have been measured in this thesis provide a great set of tools for evaluation of the mechanical reliability of aluminum nitride thin films. However, careful assessment of the stress and strain states experienced in the applications should always be conducted. Any possible variation in the crystalline quality of the films will also cause changes in the mechanical properties these films, the scale of which can be surprisingly large. Thus, when using any of the measured properties presented in this thesis, careful consideration of the relevant structural properties should always be done.

11 Conclusions

The purpose of this thesis was to first find a technique with which the mechanical reliability of AlN thin films can be assessed, and then conduct the experiments in order to measure the relevant mechanical properties of the thin films. This was successfully done in this thesis using the bulge experiment.

The mechanical properties of sputtered and MOVPE-deposited AlN thin films have been assessed. Reliable measures of Young's moduli, residual stresses, UTSes and fracture toughness of these types of AlN thin films have been produced. As there has been no research on the UTS and fracture toughness of aluminum nitride thin films, the experiments in this thesis produced unpreceded knowledge in that area. In addition to the aforementioned, fatigue effects in AlN thin films were as well studied. Through use of the methods explained in section 10, these material properties can be used in order to ensure the mechanical reliability of AlN thin films in any application of interest, where similar polycrystalline thin films are used.

From the results of the experiments conducted in this thesis, the following conclusions can be drawn: the measurements indicated that the MOVPE-deposited film was of highest crystalline quality. It also showed greater UTS, thus indicating a higher mechanical reliability than the sputtered films. The sputtered films showed that an increase in thickness from 50 to 200 nm enhances the crystalline quality of the film, and thus as well its mechanical properties as a whole. Another thickness related effect that was seen was that residual stresses increased with thickness in both MOVPE and sputtered films.

The UTS measurements with the sputtered films indicate as well that the defect population that dominates fracture nucleation in those films scales with area rather than volume. This is a very interesting finding, as volume scaling was anticipated.

A very minor indication in the direction that fatigue may have a degrading effect on the mechanical reliability of AlN thin films was seen. However, the changes caused by fatigue cycling scheme done in this thesis were so minor, that it cannot be reliably assessed that there actually is any effect.

As is explained in section 10, the properties of these thin films vary greatly depending on the deposition process parameters and thickness of the film, and thus careful consideration should be done when using the results of this thesis on AlN thin films, that are, for example, deposited on different substrate materials.

11.1 Future research

There is naturally still room for further research. The primary interest would lie in experiments with ALD films in order to verify the effects of crystallinity to the mechanical properties of these films. A fatigue cycling experiment with larger cycle amounts should as well be conducted in order to verify how susceptible these thin films are to cyclic fatigue damage. A more rigorous set of fracture toughness experiments should be done using differing pre-crack lengths and a larger sample set. As the bulge experiment was successfully used for all the measurement types in this thesis, further research can now be easily conducted as the relevant test scaling is done.

References

[1] O. Ambacher. Growth and applications of group iii-nitrides. *Journal of Physics D: Applied Physics*, 31(20):2653, 1998.

[2] G. Piazza, V. Felmetsger, P. Muralt, R. H. Olsson III, and R. Ruby. Piezoelectric aluminum nitride thin films for microelectromechanical systems. *MRS Bulletin*, 37(11):1051–1061, 2012.

[3] S. Barth, H. Bartzsch, D. Glöß, P. Frach, T. Modes, O. Zywitzki, G. Suchaneck, and G. Gerlach. Magnetron sputtering of piezoelectric aln and alscn thin films and their use in energy harvesting applications. *Microsystem Technologies*, 22(7):1613–1617, 2016.

[4] B. A. Griffin, S.D. Habermehl, and P.J. Clews. Development of an aluminum nitride-silicon carbide material set for high-temperature sensor applications. In *SPIE Sensing Technology+ Applications*, pages 91130A–91130A. International Society for Optics and Photonics, 2014.

[5] B. Griffin. Piezoelectric MEMS based on aluminum nitride. https://www.osti.gov/scitech/servlets/purl/1244916. Online; Accessed: 2017-04-19.

[6] Vesper MEMS. AlN MEMS microphone product. http://vespermems.com/products/vm1000/. Online; Accessed: 2017-04-19.

[7] D. Broek. *Elementary engineering fracture mechanics*. Springer Science & Business Media, 2012.

[8] User: philipfigari. Steps to analyzing a material's properties from its stress/strain curve. http://www.instructables.com/id/Steps-to-Analyzing-a-Materials-Properties-from-its/. Online; Accessed: 2017-04-19.

[9] M. Barsoum and M.W. Barsoum. *Fundamentals of ceramics*. CRC press, 2002.

[10] User: Twisp. Fracture mechanics - wikipedia article. https://en.wikipedia.org/wiki/File:Fracture_modes_v2.svg, 2008. [Online; accessed 27.3.2017].

[11] D.Y.W. Yu. *Microtensile testing of free-standing and supported metallic thin films*. PhD thesis, Harvard University, 2003.

[12] S. Zhang, D. Sun, Y. Fu, and H. Du. Toughness measurement of thin films: a critical review. *Surface and Coatings Technology*, 198(1):74–84, 2005.

[13] P. F. Becher. Microstructural design of toughened ceramics. *Journal of the American Ceramic Society*, 74(2):255–269, 1991.

[14] B. Merle and M. Göken. Fracture toughness of silicon nitride thin films of different thicknesses as measured by bulge tests. *Acta Materialia*, 59(4):1772–1779, 2011.

[15] X.-K. Zhu and J.A. Joyce. Review of fracture toughness (g, k, j, ctod, ctoa) testing and standardization. *Engineering Fracture Mechanics*, 85:1 – 46, 2012.

[16] M. Kamble. Quora - solid mechanics: What are the differences between plane stress and plane strain conditions?, 2015. [Online; accessed 11.5.2017].

[17] ASTM Standard. E399. *Standard Method of Test for Plane Strain Fracture Toughness of Metallic Materials*, 1971.

[18] D. Broek. *The practical use of fracture mechanics.* Springer Science & Business Media, 2012.

[19] D. Green. *An introduction to the mechanical properties of ceramics.* Cambridge University Press, 1998.

[20] D. L Anderson. *Theory of the Earth.* Blackwell scientific publications, 1989.

[21] M. Schneider, A. Bittner, P. Schmid, and U. Schmid. Impact of c-axis orientation of aluminium nitride thin films on the long-term stability and mechanical properties of resonantly excited mems cantilevers. *Procedia Engineering*, 87:1493 – 1496, 2014.

[22] A. Bourret, A. Barski, J. L. Rouvière, G. Renaud, and A. Barbier. Growth of aluminum nitride on (111) silicon: Microstructure and interface structure. *Journal of Applied Physics*, 83(4):2003–2009, 1998.

[23] B. M. Moshtaghioun, D. G.z García, A. D. Rodríguez, and N. P. Padture. High-temperature creep deformation of coarse-grained boron carbide ceramics. *Journal of the European Ceramic Society*, 35(5):1423 – 1429, 2015.

[24] R. O. Ritchie and R. H. Dauskardt. Cyclic fatigue of ceramics. *Journal of the Ceramic Society of Japan*, 99(1154):1047–1062, 1991.

[25] M. N. Aboushelib, H. Wang, C. J. Kleverlaan, and A. J. Feilzer. Fatigue behavior of zirconia under different loading conditions. *Dental Materials*, 32(7):915 – 920, 2016.

[26] T. Kitamura, H. Hirakata, T. Sumigawa, and T. Shimada. *Fracture nanomechanics.* CRC Press, 2016.

[27] J.F. Shackelford, Y.H. Han, S. Kim, and S.H. Kwon. *CRC Materials Science and Engineering Handbook, Fourth Edition.* CRC Press, 2016.

[28] S. Ogata and H. Kitagawa. Ab initio tensile testing simulation of aluminum and aluminum nitride ceramics based on density functional theory. *Computational Materials Science*, 15(4):435 – 440, 1999.

[29] E. Arzt. Size effects in materials due to microstructural and dimensional constraints: a comparative review. *Acta Materialia*, 46(16):5611 – 5626, 1998.

[30] I Gorczyca, NE Christensen, P Perlin, I Grzegory, J Jun, and M Bockowski. High pressure phase transition in aluminium nitride. *Solid state communications*, 79(12):1033–1034, 1991.

[31] C. P Laksana, M. Chen, Y. Liang, A. Tzou, H. Kao, E. S Jeng, J. S. Chen, H. Chen, and S.R. Jian. Deep-uvsensors based on saw oscillators using low-temperature-grown aln films on sapphires. *IEEE transactions on ultrasonics, ferroelectrics, and frequency control*, 58(8):1688–1693, 2011.

[32] R. B. Karabalin, M. H. Matheny, X. L. Feng, E. Defaÿ, G. Le Rhun, C. Marcoux, S. Hentz, P. Andreucci, and M. L. Roukes. Piezoelectric nanoelectromechanical resonators based on aluminum nitride thin films. *Applied Physics Letters*, 95(10), 2009.

[33] J. C Doll, B. C Petzold, B. Ninan, R. Mullapudi, and B. L Pruitt. Aluminum nitride on titanium for cmos compatible piezoelectric transducers. *Journal of Micromechanics and Microengineering*, 20(2):025008, 2009.

[34] L. Zheng, S. Ramalingam, T. Shi, and R. L. Peterson. Aluminum nitride thin film sensor for force, acceleration, and acoustic emission sensing. *Journal of Vacuum Science & Technology A: Vacuum, Surfaces, and Films*, 11(5):2437–2446, 1993.

[35] K Miwa and A Fukumoto. First-principles calculation of the structural, electronic, and vibrational properties of gallium nitride and aluminum nitride. *Physical Review B*, 48(11):7897, 1993.

[36] E. Österlund. Vertical piezoelectric structures for in-plane actuation in mems sensors. Master's thesis, Aalto University School of Electrical Engineering, 2015.

[37] M. Fernandez-Serra. The structure and entropy of ice. http://mini.physics.sunysb.edu/~marivi/TEACHING-OLD/PHY313/lib/exe/detail.php?id=lectures3A4&media=lectures:wurtzite_polyhedra.png. Online; Accessed: 2016-12-19.

[38] A.F. Wright. Elastic properties of zinc-blende and wurtzite aln, gan, and inn. *Journal of Applied Physics*, 82(6):2833–2839, 1997.

[39] MA Moram and ME Vickers. X-ray diffraction of iii-nitrides. *Reports on progress in physics*, 72(3):036502, 2009.

[40] I. Yonenaga, T. Shima, and M.H.F. Sluiter. Nano-indentation hardness and elastic moduli of bulk single-crystal aln. *Japanese journal of applied physics*, 41(7R):4620, 2002.

[41] B. Ilic, S. Krylov, and H. G. Craighead. Young's modulus and density measurements of thin atomic layer deposited films using resonant nanomechanics. *Journal of Applied Physics*, 108(4):044317, 2010.

[42] L. Yate, J.C. Caicedo, A. Hurtado Macias, F.J. Espinoza-Beltrán, G. Zambrano, J. Muñoz-Saldaña, and P. Prieto. Composition and mechanical properties of alc, aln and alcn thin films obtained by r.f. magnetron sputtering. *Surface and Coatings Technology*, 203(13):1904 – 1907, 2009.

[43] P.W Shum, K.Y Li, Z.F Zhou, and Y.G Shen. Structural and mechanical properties of titanium–aluminium–nitride films deposited by reactive close-field unbalanced magnetron sputtering. *Surface and Coatings Technology*, 185(2–3):245 – 253, 2004.

[44] S.-R. Jian and J.-Y. Juang. Indentation-induced mechanical deformation behaviors of aln thin films deposited on c-plane sapphire. *J. Nanomaterials*, 2012:36:36–36:36, January 2012.

[45] S.-R. Jian, G.-J. Chen, H.-G. Chen, J. S.-C. Jang, Y.-Y. Liao, P.-F. Yang, Y.-S. Lai, M.-R. Chen, H.-L. Kao, and J.-Y. Juang. Cross-sectional transmission electron microscopy studies for deformation behaviors of aln thin films under berkovich nanoindentation. *Journal of Alloys and Compounds*, 504, Supplement 1:S395 – S398, 2010. 16th International Symposium on Metastable, Amorphous and Nanostructured Materials.

[46] H.C. Barshilia, B. Deepthi, and K.S. Rajam. Growth and characterization of aluminum nitride coatings prepared by pulsed-direct current reactive unbalanced magnetron sputtering. *Thin Solid Films*, 516(12):4168 – 4174, 2008.

[47] N. Jackson, O. Z. Olszewski, L. Keeney, A. Blake, and A. Mathewson. A capacitive based piezoelectric aln film quality test structure. In *Proceedings of the 2015 International Conference on Microelectronic Test Structures*, pages 193–197, March 2015.

[48] S.-R. Jian, Guo-Ju Chen, and Ting-Chun Lin. Berkovich nanoindentation on aln thin films. *Nanoscale Research Letters*, 5(6):935, 2010.

[49] T.A. Rawdanowicz, V. Godbole, J. Narayan, J. Sankar, and A. Sharma. The hardnesses and elastic moduli of pulsed laser deposited multilayer aln/tin thin films. *Composites Part B: Engineering*, 30(7):657 – 665, 1999.

[50] M. Schneider, A. Bittner, and U. Schmid. Thickness dependence of youngs modulus and residual stress of sputtered aluminum nitride thin films. *Applied Physics Letters*, 105(20), 2014.

[51] S. Raghavan and J.M. Redwing. In situ stress measurements during the {MOCVD} growth of aln buffer layers on (1 1 1) si substrates. *Journal of*

Crystal Growth, 261(2–3):294 – 300, 2004. Proceedings of the 11th Biennial (US) Workshop on Organometallic Vapor Phase Epitaxy (OMVPE).

[52] H. Miyazaki, Y. Yoshizawa, K. Hirao, and T. Ohji. Evaluation of fracture toughness of ceramic thin plates through modified single edge-precracked plate method. *Scripta Materialia*, 103:34 – 36, 2015.

[53] User: Ben Mills. Silicon - wikipedia article. https://en.wikipedia.org/wiki/File:Silicon-unit-cell-3D-balls.png, 2007. [Online; accessed 7.1.2017].

[54] JX Zhang, H Cheng, YZ Chen, A Uddin, Shu Yuan, SJ Geng, and S Zhang. Growth of aln films on si (100) and si (111) substrates by reactive magnetron sputtering. *Surface and Coatings Technology*, 198(1):68–73, 2005.

[55] O. Borrero-Lopez and M. Hoffman. Measurement of fracture strength in brittle thin films. *Surface and Coatings Technology*, 254:1–10, 2014.

[56] S. Wei, F. Qun-Bo, W. Fu-Chi, and M. Zhuang. The influence of defects on the effective young's modulus of a defective solid. *Chinese Physics B*, 22(4):044601, 2013.

[57] H. S. Kim and M. B. Bush. The effects of grain size and porosity on the elastic modulus of nanocrystalline materials. *Nanostructured Materials*, 11(3):361 – 367, 1999.

[58] L. B. Freund and S. Suresh. *Thin film materials: stress, defect formation and surface evolution*. Cambridge University Press, 2004.

[59] S Akiba, A Matsuda, H Isa, M Kasahara, S Sato, T Watanabe, W Hara, and M Yoshimoto. Formation of a nanogroove-striped nio surface using atomic steps. *Nanotechnology*, 17(16):4053, 2006.

[60] V. Miikkulainen, M. Leskelä, M. Ritala, and R. L. Puurunen. Crystallinity of inorganic films grown by atomic layer deposition: Overview and general trends. *Journal of Applied Physics*, 113(2):021301, 2013.

[61] S. Goerke, M. Ziegler, A. Ihring, J. Dellith, A. Undisz, M. Diegel, S. Anders, U. Huebner, M. Rettenmayr, and H.-G. Meyer. Atomic layer deposition of aln for thin membranes using trimethylaluminum and h2/n2 plasma. *Applied Surface Science*, 338:35 – 41, 2015.

[62] M. Broas, P. Sippola, T. Sajavaara, V. Vuorinen, A. Pyymaki-Perros, H. Lipsanen, and M. Paulasto-Kröckel. Structural and chemical analysis of annealed plasma-enhanced atomic layer deposition aluminum nitride films. *Journal of Vacuum Science & Technology A: Vacuum, Surfaces, and Films*, 34(4):041506, 2016.

[63] C. Ozgit, I. Donmez, M. Alevli, and N. Biyikli. Self-limiting low-temperature growth of crystalline aln thin films by plasma-enhanced atomic layer deposition. *Thin Solid Films*, 520(7):2750 – 2755, 2012.

[64] M. A. Herman, W. Richter, and H. Sitter. *Epitaxy: physical principles and technical implementation*, volume 62. Springer Science & Business Media, 2013.

[65] I. M. Watson. Metal organic vapour phase epitaxy of aln, gan, inn and their alloys: A key chemical technology for advanced device applications. *Coordination Chemistry Reviews*, 257(13–14):2120 – 2141, 2013. Chemistry and Applications of Metal Nitrides.

[66] WJ Meng, J Heremans, and YT Cheng. Epitaxial growth of aluminum nitride on si (111) by reactive sputtering. *Applied physics letters*, 59(17):2097–2099, 1991.

[67] K. Wasa and S. Hayakawa. *Handbook of sputter deposition technology.* Noyes Publications, 1992.

[68] J Bhardwaj, H Ashraf, and A McQuarrie. Dry silicon etching for mems. In *Symposium on Microstructures and Microfabricated Systems*, pages 4–9, 1997.

[69] L. Sainiemi. *Cryogenic deep reactive ion etching of silicon micro and nanostructures.* G5 artikkeliväitöskirja, Teknillinen korkeakoulu, 2009.

[70] S. Reyntjens and R. Puers. A review of focused ion beam applications in microsystem technology. *Journal of Micromechanics and Microengineering*, 11(4):287, 2001.

[71] G. G. Stoney. The tension of metallic films deposited by electrolysis. *Proceedings of the Royal Society of London. Series A, Containing Papers of a Mathematical and Physical Character*, 82(553):172–175, 1909.

[72] U. Wiklund, M. Bromark, M. Larsson, P. Hedenqvist, and S. Hogmark. Cracking resistance of thin hard coatings estimated by four-point bending. *Surface and Coatings Technology*, 91(1):57 – 63, 1997.

[73] I. Hofinger, M. Oechsner, H.-A. Bahr, and M. V. Swain. Modified four-point bending specimen for determining the interface fracture energy for thin, brittle layers. *International Journal of Fracture*, 92(3):213–220, 1998.

[74] T.L. Becker, J.M. McNaney, R.M. Cannon, and R.O. Ritchie. Limitations on the use of the mixed-mode delaminating beam test specimen: Effects of the size of the region of k-dominance. *Mechanics of Materials*, 25(4):291–308, 1997.

[75] D. T. Read and A. A. Volinsky. Measurements for mechanical reliability of thin films. In *Security and Reliability of Damaged Structures and Defective Materials*, pages 337–358. Springer, 2009.

[76] Q. Kan, W. Yan, G. Kang, and Q. Sun. Oliver–pharr indentation method in determining elastic moduli of shape memory alloys—a phase transformable material. *Journal of the Mechanics and Physics of Solids*, 61(10):2015–2033, 2013.

[77] G. D. Quinn and R. C. Bradt. On the vickers indentation fracture toughness test. *Journal of the American Ceramic Society*, 90(3):673–680, 2007.

[78] M. Sebastiani, K.E. Johanns, E.G. Herbert, and G.M. Pharr. Measurement of fracture toughness by nanoindentation methods: Recent advances and future challenges. *Current Opinion in Solid State and Materials Science*, 19(6):324 – 333, 2015. Recent Advances in Nanoindentation.

[79] B. N. Jaya, C. Kirchlechner, and G. Dehm. Can microscale fracture tests provide reliable fracture toughness values? a case study in silicon. *Journal of Materials Research*, 30(5):686–698, Mar 2015.

[80] D. Kupka, N. Huber, and E.T. Lilleodden. A combined experimental-numerical approach for elasto-plastic fracture of individual grain boundaries. *Journal of the Mechanics and Physics of Solids*, 64:455 – 467, 2014.

[81] D. Son, J.-h. Jeong, and D. Kwon. Film-thickness considerations in microcantilever-beam test in measuring mechanical properties of metal thin film. *Thin Solid Films*, 437(1):182–187, 2003.

[82] V.T. Srikar and S.M. Spearing. A critical review of microscale mechanical testing methods used in the design of microelectromechanical systems. *Experimental mechanics*, 43(3):238–247, 2003.

[83] W. N. Sharpe, B. Yuan, R. Vaidyanathan, and R. L. Edwards. Measurements of young's modulus, poisson's ratio, and tensile strength of polysilicon. In *Micro Electro Mechanical Systems, 1997. MEMS'97, Proceedings, IEEE., Tenth Annual International Workshop on*, pages 424–429. IEEE, 1997.

[84] I. Chasiotis and W. G. Knauss. A new microtensile tester for the study of mems materials with the aid of atomic force microscopy. *Experimental Mechanics*, 42(1):51–57, 2002.

[85] D. T. Read, Y.-W. Cheng, R. R. Keller, and J. D. McColskey. Tensile properties of free-standing aluminum thin films. *Scripta Materialia*, 45(5):583–589, 2001.

[86] R. Liu, H. Wang, X. Li, G. Ding, and C. Yang. A micro-tensile method for measuring mechanical properties of mems materials. *Journal of Micromechanics and Microengineering*, 18(6):065002, 2008.

[87] M.A. Haque and M.T.A. Saif. Microscale materials testing using mems actuators. *Journal of Microelectromechanical Systems*, 10(1):146–152, 2001.

[88] D.S. Gianola and C. Eberl. Micro-and nanoscale tensile testing of materials. *JOM Journal of the Minerals, Metals and Materials Society*, 61(3):24–35, 2009.

[89] M.A. Haque and M.T.A. Saif. In-situ tensile testing of nano-scale specimens in sem and tem. *Experimental mechanics*, 42(1):123–128, 2002.

[90] Y.-S. Kang and P. S. Ho. Thickness dependent mechanical behavior of submicron aluminum films. *Journal of Electronic Materials*, 26(7):805–813, 1997.

[91] M.A. Haque and M.T.A. Saif. Mechanical behavior of 30–50 nm thick aluminum films under uniaxial tension. *Scripta Materialia*, 47(12):863–867, 2002.

[92] Y. Zhu and H.D. Espinosa. An electromechanical material testing system for in situ electron microscopy and applications. *Proceedings of the National Academy of Sciences of the United States of America*, 102(41):14503–14508, 2005.

[93] JJ Vlassak and WD Nix. A new bulge test technique for the determination of young's modulus and poisson's ratio of thin films. *Journal of Materials Research*, 7(12):3242–3249, 1992.

[94] J. S Mitchell, C. A Zorman, T. Kicher, S. Roy, and M. Mehregany. Examination of bulge test for determining residual stress, young's modulus, and poisson's ratio of 3c-sic thin films. *Journal of Aerospace Engineering*, 16(2):46–54, 2003.

[95] Y. Xiang, J. McKinnell, W.-M. Ang, and J. J. Vlassak. Measuring the fracture toughness of ultra-thin films with application to alta coatings. *International Journal of Fracture*, 144(3):173–179, 2007.

[96] M. Berdova, T. Ylitalo, I. Kassamakov, J. Heino, P. T. Törmä, L. Kilpi, H. Ronkainen, J. Koskinen, E. Häggström, and S. Franssila. Mechanical assessment of suspended {ALD} thin films by bulge and shaft-loading techniques. *Acta Materialia*, 66:370 – 377, 2014.

[97] C. Suryanarayana and M. G.t Norton. *X-ray diffraction: a practical approach*. Springer Science & Business Media, 2013.

[98] R. Yogamalar, R. Srinivasan, A. Vinu, K. Ariga, and A. C. Bose. X-ray peak broadening analysis in zno nanoparticles. *Solid State Communications*, 149(43–44):1919 – 1923, 2009.

[99] Hiroyuki Fujiwara. *Spectroscopic ellipsometry: principles and applications*. John Wiley & Sons, 2007.

[100] N. Yao and Z. L. Wang. *Handbook of microscopy for nanotechnology*. Springer, 2005.

[101] J.Y. Pan, P. Lin, F. Maseeh, and S.D. Senturia. Verification of fem analysis of load-deflection methods for measuring mechanical properties of thin films. In *Solid-State Sensor and Actuator Workshop, 1990. 4th Technical Digest., IEEE*, pages 70–73. IEEE, 1990.

[102] V. Y. Pickhardt and D. L. Smith. Fabrication of high-strength unsupported metal membranes. *Journal of Vacuum Science and Technology*, 14(3):823–825, 1977.

[103] V. Rontu. Mechanical properties of ald al2o3 thin films. Unsubmitted as of 22.5.2017.

[104] M. K. Small and W.D. Nix. *Use of the bulge test in measuring the mechanical properties of thin films*. PhD thesis, to the Department of Materials Science and Engineering.Stanford University, 1992.

[105] B. Merle and M. Göken. Bulge fatigue testing of freestanding and supported gold films. *Journal of Materials Research*, 29(2):267–276, Jan 28 2014. Copyright - Copyright © Materials Research Society 2013; Last updated - 2014-04-02; CODEN - JMREEE.

[106] Y. Xiang, J. McKinnell, W.-M. Ang, and J.J. Vlassak. Measuring the fracture toughness of ultra-thin films with application to alta coatings. *International Journal of Fracture*, 144(3):173–179, 2007.

[107] S Sirvio, L Sainiemi, S Franssila, and K Grigoras. Atomic layer deposition of al2o3, tio2 and zno films into high aspect ratio pores. In *Solid-State Sensors, Actuators and Microsystems Conference, 2007. TRANSDUCERS 2007. International*, pages 521–524. IEEE, 2007.

[108] A. Perros, M.s Bosund, T. Sajavaara, M. Laitinen, L. Sainiemi, T. Huhtio, and H. Lipsanen. Plasma etch characteristics of aluminum nitride mask layers grown by low-temperature plasma enhanced atomic layer deposition in sf6 based plasmas. *Journal of Vacuum Science & Technology A*, 30(1), 2012.

[109] J. Zhou, M. DeMiguel-Ramos, L. Garcia-Gancedo, E. Iborra, J. Olivares, H. Jin, J.K. Luo, A.S. Elhady, S.R. Dong, D.M. Wang, and Y.Q. Fu. Characterisation of aluminium nitride films and surface acoustic wave devices for microfluidic applications. *Sensors and Actuators B: Chemical*, 202:984 – 992, 2014.

[110] K. A. Aissa, A. Achour, J. Camus, L. Le Brizoual, P.-Y. Jouan, and M.-A. Djouadi. Comparison of the structural properties and residual stress of aln films deposited by dc magnetron sputtering and high power impulse magnetron sputtering at different working pressures. *Thin Solid Films*, 550:264–267, 2014.

[111] K. M. Taylor and C. Lenie. Some properties of aluminum nitride. *Journal of The Electrochemical Society*, 107(4):308–314, 1960.